Inclusive charged and strange particle production at the CERN SppS collider

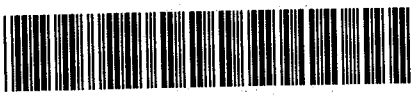

Lucas Taylor

Thesis submitted for the degree of Doctor of Philosophy
of the University of London
and for the Diploma of Membership of Imperial College

July 1990

Imperial College, London

Abstract

The analysis presented herein is based on data collected during the autumn of 1987 by the UA1 experiment at the CERN $Sp\bar{p}S$ collider, operating at a centre-of-mass energy of $630\,GeV$. Approximately three million $p\bar{p}$ interactions were recorded with minimal requirements on the physics content. Since the statistical errors of the data sample are small, emphasis has been placed on the understanding and the minimisation of the systematic errors. The inclusive production of charged hadrons has been studied. In addition, neutral K_S^0 mesons were reconstructed via their weak decay to two charged pions. A sample of 91 000 K_S^0 candidates, with a purity of 86%, has been obtained enabling the inclusive K_S^0 production cross-section to be measured up to a transverse momentum of $6GeV/c$. A comparison with the charged pion cross-section, *i.e.* the K/π ratio, is made. Using a statistically-motivated additive quark model for soft hadron-production, the *strange* quark suppression factor has been evaluated.

Contents

List of Figures

List of Tables

Preface

The work described in this thesis was carried out at the Imperial College for Science, Technology and Medicine, London, England and at the European Centre for Nuclear Research (CERN) in Geneva, Switzerland. The data analysed were collected by the UA1 experiment [1] and comprise a vast amount of information on the decay products of high energy collisions in the Super Proton-Antiproton Synchrotron (Sp$\bar{p}$S) collider at CERN operating at a centre-of-mass energy of $630 GeV$.

Chapter 1 introduces the Standard Model of high-energy nuclear interactions and outlines the theoretical ideas particular to this analysis. The Sp$\bar{p}$S collider, the UA1 detector and the central tracking chamber (CD) are described in chapters 2 and 3. The calibration of the CD is discussed in chapter 4. The inclusive production properties of charged hadrons is presented in chapter 5. Attention is then focussed on the finding of neutral kaon decays (chapter 6), the calculation of their reconstruction efficiency (chapter 7). Finally, in chapter 8, the K^0 results are presented and compared to the inclusive charged hadron production properties and theoretical predictions.

The analysis described in chapters 4 to 8 and the appendices is the author's own work apart from the following: §4.1 describes a standard calibration method, and §6.1 the UA1 V^0-finding algorithm. The K^0_S reconstruction efficiency method described in chapter 7 was developed in a previous UA1 analysis, although much technical work on the software was needed. Appendix A is a description of the standard method for evaluating the acceptance of the central drift chamber.

I am indebted to all those members of the UA1 collaboration who helped me in this work, in particular to Aleandro Nisati for introducing me to this subject, to Veikko Karimäki for his excellent V^0-finding package, and to Igor Zacharov

[1] UA1 is a collaboration of institutions from Aachen, Amsterdam (NIKHEF), Annecy (LAPP), Birmingham, CERN, Harvard, Helsinki, Kiel, London (Imperial College, and Queen Mary College), Madrid (CIEMAT), MIT, Padua, Paris (College de France), Riverside, Rome, Rutherford Appleton Laboratory, Saclay (CEN), Victoria, Vienna and Wisconsin.

for much help with software and the K^0 reconstruction efficiencies. Our many discussions on these and other topics were invaluable to this work. The computing resources required for this work were extensive. I am grateful to Alan Norton for providing me with the necessary CPU time and cassettes, and to the members of the Data Division at CERN and the computing staff at the Rutherford Appleton Laboratory, for maintaining such excellent services. I have benefited greatly from the software expertise of Tony Cass, Michel Della Negra and Jonathan Gregory. I would like to thank my supervisor, Jim Virdee, for all his help and guidance on all aspects of this thesis and Chris Seez who was a constant source of sound advice. I am grateful to David Binnie without whose support completion may have been much delayed and to Linda Jones for managing the Imperial College bureaucracy.

My deepest thanks go to Nick and Simon Lawson, Staphan Sarkissian, Andrew Belk, David Robinson, Mike MacDermott, Sybille Christen and especially to my family for their love, support and hospitality.

This work was supported in part by the Science and Engineering Research Council of Great Britain.

1. Introduction

All known matter is now thought to be built from a small number of elementary point-like particles whose interactions may be explained in terms of just four forces, namely the Gravitational, Weak, Electromagnetic and Strong interactions. Elementary matter particles (known as fermions since they obey Fermi-Dirac statistics) may be classified as quarks which interact via all four interactions and leptons which do not experience the Strong force. These may be further divided into three families, or generations, each with two members, as shown in table 1.1. [1] Each fundamental particle has an anti-particle with the same mass. Free quarks have not been seen in nature — instead they form $q\bar{q}$ (meson) and qqq (baryon) [2] bound states of the Strong interaction, known collectively as hadrons. Quantum Field

	Generation			Electric
	I	II	III	charge, Q
Quarks	up (u)	charm (c)	top (t)	$+\frac{2}{3}$
	down (d)	strange (s)	bottom (b)	$-\frac{1}{3}$
Leptons	e^-	μ^-	τ^-	-1
	ν_e	ν_μ	ν_τ	0

Table 1.1: Fundamental Particles

theories (see, for example, ref. [1]) have been developed to describe the Weak, Electromagnetic and Strong interactions in which the forces between fermions are explained in terms of the exchange of mediating particles (table 1.2). Axiomatic to these theories is the principle of *gauge-invariance* ("gauge" is an historical mis-

[1] The top quark and the tau-neutrino have yet to be experimentally observed.
[2] Here q and $\bar{q}$ denote a quark and an antiquark respectively.

Interaction	Coupling strength	Range (m)	Mediating boson	Quantum number
Strong	$\alpha_S \sim 1$	$\sim 10^{-15}m$	Gluon, g	Colour
Electromagnetic	$\alpha = \frac{e^2}{4\pi\hbar c} = 1/137$	∞	Photon, γ	Charge
Weak	$G_F m_p^2 \simeq 10^{-5}$	$\sim 10^{-18}m$	W^+,W^-,Z^0	Weak isospin
Gravitational	$\mathcal{G} m_p^2 \simeq 6 \times 10^{-39}$	∞	Graviton, G	Mass

Table 1.2: Properties of the four fundamental forces

nomer for "phase"). The global phase of the fermion fields may be arbitrarily chosen without changing any observable quantity. Associated with this internal symmetry is a conserved quantity. [3] The interactions between the matter fields arise naturally by demanding that the theory be not just globally but also *locally* gauge-invariant. Additional so-called gauge fields must then be introduced to compensate for the, otherwise observable, phase differences of different space-time points. The quanta of these gauge fields are the exchange particles mediating the force.

The Electromagnetic and Weak interactions are well described by a unified Electroweak theory (§1.1); Quantum-Chromodynamics (§1.2) is the theory of the Strong interaction. There is no satisfactory quantised theory of Gravity which is described by the classical theory of General Relativity. It is believed that all four forces may be different aspects of a single universal interaction but there is, as yet, no successful unification theory incorporating the Strong interaction and Gravity.

1.1 Electroweak theory

The theory of electromagnetism is invariant under global changes in the phase of the fermion fields. This invariance is equivalent to the conservation of the

[3] In a similar way, the laws of conservation of energy, momentum and angular momentum arise from the invariance of physical processes under displacements in time, and spatial translations and rotations.

electromagnetic current. If the phase is allowed to vary independently at each space-time point, then a new vector field which couples to the fermion must be introduced for the theory to remain locally gauge-invariant. This massless field is the photon field and the interacting theory is known as Quantum Electrodynamics (QED).

To construct a gauge-invariant field theory for the Weak interaction the electromagnetic interaction must be included. The symmetry group for this unified Electroweak theory [2] is $SU(2)_L \times U(1)$, where the subscript, L, indicates that only the left-handed spin components of the field interact weakly. The conserved quantities are Weak isospin t and Weak hypercharge y. The $SU(2)_L$ gauge fields are a weak iso-triplet W_i $(i = 1, 2, 3)$; the $U(1)$ field B is a weak hypercharge singlet. Both W_i and B are massless.

The experimentally observed mediators of the Weak interaction, the charged W^+ and W^- and the neutral Z^0, are however massive. To give the $SU(2)$ gauge fields mass in a gauge invariant way the existence of addition scalar particles, known as Higgs' bosons (see *e.g.* ref. [1]), is postulated which, in the minimal model, form a weak isospin doublet, $\binom{\phi^+}{\phi^0}$. These interact with the massless gauge fields W_i and B, spontaneously breaking the gauge symmetry, to give three massive bosons, *i.e.* $W^\pm$ and Z^0, and a massless photon field A. The $W^\pm$ are given by

$$W^\pm = \frac{1}{\sqrt{2}}(W_1 \pm iW_2) \tag{1.1}$$

The Z^0 and photon are linear combinations of W_3 and B:

$$Z^0 = W_3 \cos\theta_W - B \sin\theta_W \tag{1.2}$$

$$A = W_3 \sin\theta_W + B \cos\theta_W \tag{1.3}$$

The Weak mixing angle θ_W must be determined by experiment.

The left-handed parts of the lepton fields are *Weak isospin* doublets $\binom{e^-}{\nu_e}_L$, $\binom{\mu^-}{\nu_\mu}_L$, and $\binom{\tau^-}{\nu_\tau}_L$. The right-handed components of massive lepton fields, e_R^-, μ_R^- and τ_R^-, are weak isospin singlet states; right-handed neutrinos do not exist.

Decays between quark families (*e.g.* $\Lambda^0 \to p\pi^-$ in which an s quark decays to a u quark and a W boson) show that $\binom{u}{d}$, $\binom{c}{s}$ and $\binom{t}{b}$, cannot be exact weak isospin doublets. The Strong eigenstates of the quarks are not the same as the Weak eigenstates. Choosing to fix u, c and t, the weak isospin doublets are $\binom{u}{d'}$, $\binom{c}{s'}$ and $\binom{t}{b'}$, where d', s' and b' are superpositions of the Strong eigenstates d, s and b:

$$\begin{pmatrix} d' \\ s' \\ b' \end{pmatrix} = \begin{pmatrix} U_{ud} & U_{us} & U_{ub} \\ U_{cd} & U_{cs} & U_{cb} \\ U_{td} & U_{ts} & U_{tb} \end{pmatrix} \begin{pmatrix} d \\ s \\ b \end{pmatrix} \tag{1.4}$$

U_{ij} is the unitary Cabibbo-Kobayashi-Maskawa matrix [3]. Thus, for example, the coupling for $d \to u + W^-$ carries a factor U_{ud}, $s \to u + W^-$ a factor U_{us}, and so on. Since any superposition of neutrinos is a massless state, there is no mixing matrix for the leptons — *by definition*, ν_e is the neutrino paired with the electron in Weak interactions, just as d' is the quark paired with u.

1.2 The Strong Interaction

Analogous to the electric charge in QED, strongly interacting particles have a strong charge known as colour. Quarks come in three colours, [4] say red(r), green(g) and blue(b) while antiquarks carry anti-colour ($\bar{r}, \bar{g}$ and $\bar{b}$). The quarks are combined to form colour singlet baryons (three quarks) and mesons (a quark and an antiquark), *e.g.* $q_r q_g q_b$ and $q_r \bar{q}_{\bar{r}}$ respectively, which are known collectively as hadrons. The strong interactions of quarks are invariant under colour interchange *i.e.* each quark is a colour triplet state of the symmetry group $SU(3)_C$.

A theory of the Strong interaction is obtained using the principle of local gauge

[4] The total number of colours N_C is measured, for example, by the ratio of the inclusive cross-sections:

$$R = \frac{\sigma(e^+e^- \to \text{hadrons})}{\sigma(e^+e^- \to \mu^+\mu^-)} = N_C \sum_{\text{flavours}} q_i^2$$

where q_i is the quark charge.

invariance, based on the $SU(3)_C$ group of phase transformations of the quark colour fields. For the theory to be locally gauge invariant, eight massless gauge fields are needed. The quanta of these fields form an $SU(3)_C$ octet of coloured vector *gluons* (carrying one colour and one anti-colour) which mediate the Strong interaction. Thus, for example, a red and a green quark may interact via the exchange of a $r\bar{g}$ gluon.

Since gluons carry colour they are themselves subject to the colour field. As a result, the field surrounding a colour charge becomes polarised such that the the strength of the strong force increases with distance. [5] The strong coupling constant, $\alpha_S(q^2)$, is given by [4]:

$$\alpha_S(q^2) = \frac{12\pi}{(33 - 2n_f)\ln(q^2/\Lambda^2)} + (\text{higher order terms}) \qquad (1.5)$$

where n_f is the number of quark flavours with mass less than the energy scale q of the interaction, and Λ ($\sim 200MeV$) is obtained from experiment. For large q^2 the coupling constant is small. Such interactions are well described by the gauge-invariant perturbative field theory known as Quantum Chromodynamics (QCD). At low q^2, however, α_s is large and higher order terms cannot be ignored. In this regime a more phenomenological approach is needed.

1.3 Inclusive hadron production

Soft hadronic collisions are responsible for most of the total $p\bar{p}$ cross-section but, since the coupling constant is large, they cannot be treated by perturbative QCD. A low momentum transfer interaction is shown schematically in fig. 1.1. The interacting hadrons may be considered as *bags* or *clusters* of many quarks and gluons. A soft interaction takes place involving many of these partons, represented by the dashed lines in fig. 1.1, resulting in an excited state of low x_L partons which

[5] This is to be contrasted with electromagnetism in which the virtual e^+e^- pairs produced in the *neutral* photon field surrounding an electrically charged particle, polarise to shield the 'bare' charge.

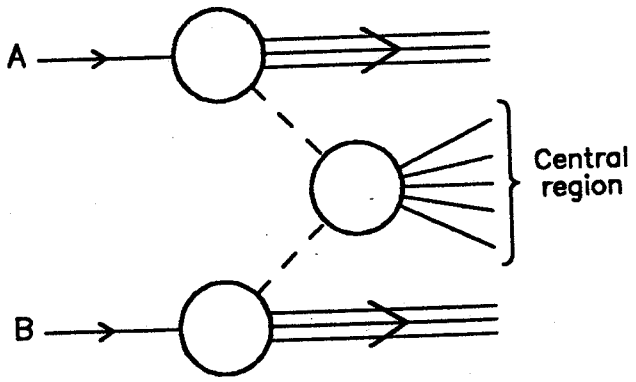

Figure 1.1: Schematic diagram of low q^2 hadron scattering.

then combine to form hadrons in the so-called central region. For low $\sqrt{s}$ (*e.g.* at the CERN ISR) the hadronic cross-section is completely dominated by soft multi-parton interactions. In this regime, the event multiplicity and the mean transverse momentum of the final-state particles increase approximately as $\log(s)$. The charged hadron p_t spectrum [6] for soft interactions involving many partons is predicted to follow a Boltzmann distribution, $e^{-\beta E}$, with E is the transverse mass: $m_t \equiv \sqrt{p_t^2 + m_\pi^2}$ [5]. This form has been verified for inclusive pion production at the ISR [6,7] and is expected to hold for soft interactions at the Sp$\bar{\text{p}}$S where the energy density (and hence the number of degrees of freedom of the system) is even greater.

An additive quark model has been developed to describe multi-particle production in the central region [8,9], in which the non-perturbative dynamics of the strong interaction are not considered. Based on statistical arguments it predicts the *relative* yields of different hadrons. The basic model has been extended to include the decay particles of short lived resonances [10]. The *uds* $SU(6)$ flavour-spin symmetry is assumed to be broken only by a relative suppression of strange particle production, due to the higher mass of the strange quark. This is quantified

[6] The transverse momentum, p_t, of a particle is the component of momentum perpendicular to the incoming hadrons.

by the parameter, λ, defined as:

$$\lambda = \frac{2\langle n_{s\bar{s}}\rangle}{\langle n_{u\bar{u}}\rangle + \langle n_{d\bar{d}}\rangle} \tag{1.6}$$

where $\langle n_{s\bar{s}}\rangle$, $\langle n_{u\bar{u}}\rangle$ and $\langle n_{d\bar{d}}\rangle$ are the mean numbers of strange, up and down quarks and anti-quarks in the final state. The interaction is assumed to be of sufficiently high-energy to produce enough partons for the quantum numbers of the initial state hadrons, A and B, to have no effect on the final state. With this assumption, $\lambda = 1$ in the absence of symmetry breaking. Each quark or antiquark is assumed to bind with another quark or antiquark with equal probability until a meson or baryon is formed. The spins of the partons are assumed to be uncorrelated and a factor of $(2J + 1)$ is applied to the yield of a hadron with spin J. The relative fraction, C_i, of a particle type i in the final state has been evaluated in terms of λ. The coefficients C_i, calculated in ref. [10], are presented in table 1.3. By studying the relative production of hadrons which differ only by the replacement of a d quark by a s quark, λ may be measured. In chapter 8, the relative yields of neutral kaons to charged hadrons and pions are obtained. In the framework of this model the strange quark suppression factor, λ, has been evaluated.

At the Sp$\bar{\text{p}}$S collider events with high p_t jets originating from the hard scattering of just two partons are observed. Such events are characterised by a relatively high charged particle multiplicity, $\langle n_{\text{ch}}\rangle$, and mean transverse momentum, $\langle p_t\rangle$, compared to the large background of soft events which have similar properties to those at lower $\sqrt{s}$. The high momentum transfer inclusive process, $p\bar{p} \rightarrow C + X$ (where X represents all the final-state particles produced excluding C), is illustrated schematically in fig. 1.2. The coupling constant, α_s, is small so the underlying interaction can be approximately described as a hard scatter of just two constituent partons, a and b from the colliding hadrons A and B. The remaining partons in the hadrons A and B form jets of hadrons with large $x_L = p_L/p$, where p_L and p are the longitudinal and total hadron momenta. The nature of the hadrons produced in this so-called beam-fragmentation region depends on the

Particle type	Relative yield for direct production	Relative yield, C_i, including resonance decays
π^+, π^-	3	$31 + 12\lambda + 3\lambda^2 + \gamma(\frac{16}{3} + 4\lambda + \frac{8}{3}\lambda^2)$
π^0	3	$34 + 12\lambda + 4\lambda^2 + \gamma(\frac{16}{3} + 4\lambda + \frac{8}{3}\lambda^2)$
K^+, K^-	3λ	$12\lambda + 4\lambda^2$
$K^0, \bar{K}^0$	3λ	$12\lambda + 3\lambda^2$
η	$1 + 2\lambda^2$	—
χ	$2 + \lambda^2$	—
$\rho^+, \rho^0, \rho^-, \omega$	9	—
ϕ	$9\lambda^2$	—
$K^{*+}, K^{*0}, \bar{K}^{*0}, K^{*-}$	9λ	—
$p, n, \bar{p}, \bar{n}$	γ	5γ
$\Lambda, \bar{\Lambda}$	$\gamma\lambda$	$8\gamma\lambda$
$\Sigma^+, \Sigma^-, \bar{\Sigma}^+, \bar{\Sigma}^+$	$\gamma\lambda$	$\gamma\lambda$
$\Sigma^0, \bar{\Sigma}^0$	$\gamma\lambda$	—
$\Xi^0, \Xi^-, \bar{\Xi}^0, \bar{\Xi}^+$	$\gamma\lambda^2$	$3\gamma\lambda^2$
$\Omega^-, \bar{\Omega}^+$	$3\gamma\lambda^3$	$3\gamma\lambda^3$

Table 1.3: Relative particle yields, C_i, in the central region including resonance decay products; $\gamma = (4 + 4\lambda + 4\lambda^2)/(5 + 5\lambda + 3\lambda^2 + \lambda^3)$

quantum numbers of the colliding particles and any intermediate resonances produced. The scattered partons, a and b, may be valence quarks, sea quarks or gluons. The available energy of the collision depends on the momenta of the partons a and b. The structure function, $f_A^a(x_a, q^2)$, gives the probability that the parton a has a fraction x_a ($0 \leq x_a \leq 1$) of the momentum of hadron A. Fig. 1.3 shows schematically the proton structure functions for u, d and s quarks [11]. The u and d curves include both valence quarks (which determine the quantum numbers of the hadron) and sea quarks (which are virtual), whereas the s quarks can come only from the sea. The average fraction of the proton momentum carried by the quarks is 54%. The remaining 46% is distributed amongst the gluons.

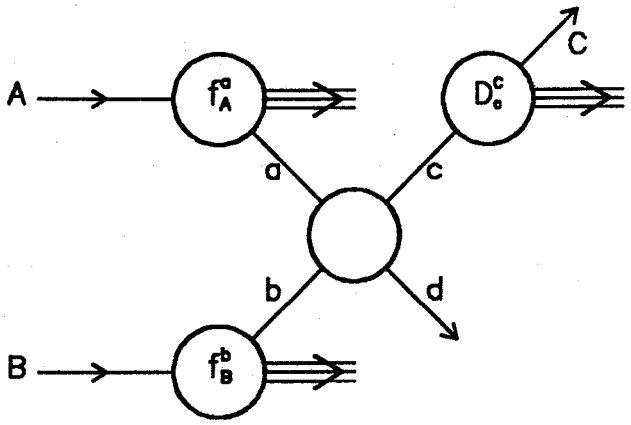

Figure 1.2: Schematic diagram of high q^2 hadron scattering.

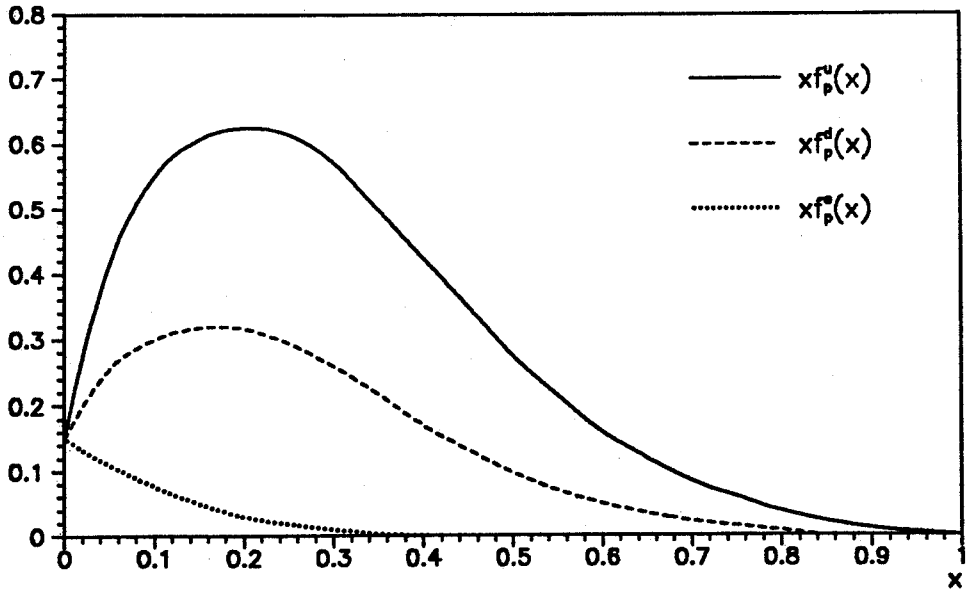

Figure 1.3: Schematic shape of the proton structure functions for u, d and s quarks

The partons c and d produced by the hard scatter can have a large transverse momentum component, p_t, relative to the incoming hadrons. As c and d fly apart, the strong colour field between them increases until a quark-antiquark pair is produced from the vacuum. These combine, or *hadronise* to form jets of hadrons in the central region. The fragmentation functions, $D_c^C(z_C, q^2)$ give the probability that the hadron, C, will be produced with momentum $z_C p_c$ from a parton c with momentum p_c. The observation of high p_t tracks in an event is indicative of an underlying high q^2 interaction.

For high q^2 interactions, perturbative QCD has been used to calculate analytically the parton cross-sections for the processes $q\bar{q} \rightarrow q\bar{q}$, $gq \rightarrow gq$, $gg \rightarrow q\bar{q}$, *etc.*, where higher order effects such as gluon emission are neglected [12]. In the asymptotic limit ($\sqrt{s}, q^2 \rightarrow \infty$), the quantity $p_t^4 f(p_t)$ (where $f(p_t)$ is the differential cross-section) is predicted to have a universal functional form independent of $\sqrt{s}$. This prediction, known as Feynmann scaling, is only predicted in the leading logarithm approximation of QCD, *i.e.* when q^2 is large and hence α_s is small. Higher order diagrams, involving multiple gluon exchange or the spectator partons (see *e.g.* fig. 1.4), introduce corrections terms which evolve as p_t^{-n}, where $n > 4$. Such corrections increase with decreasing q^2 (since α_s increases) until many

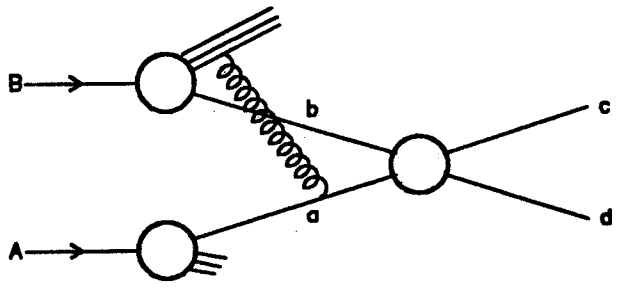

Figure 1.4: Higher twist diagram involving a spectator parton.

partons are involved. The soft regime discussed above is the extreme case where no hard scatter can be distinguished. There are a number of other effects which produce violations of Feynmann scaling and lead to increases in the power, n:

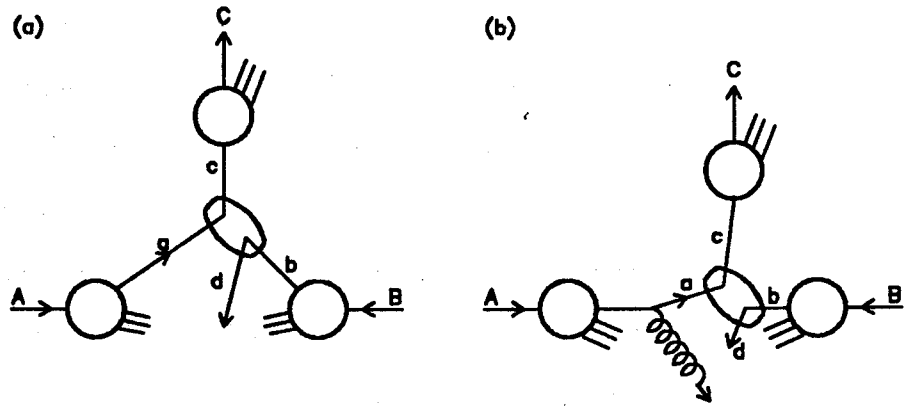

Figure 1.5: Intrinsic parton p_t from (a) Fermi motion and (b) gluon bremsstrahlung.

- **Intrinsic parton momentum.**

The partons have an intrinsic transverse momentum, k_t, within the hadron from two sources. Firstly, the parton is confined within the hadron and so, according to Heisenberg's uncertainty principle, it will have a transverse Fermi momentum, shown schematically in fig. 1.5(a), of $\Delta p_t \sim \hbar/r \sim \hbar/(0.5fm) \simeq 0.4GeV/c$. The second contribution to k_t is from the emission of gluons by the partons, a process known as initial state gluon bremsstrahlung (fig. 1.5(b)). The intrinsic transverse momentum can be measured experimentally using the Drell-Yan process $AB \rightarrow \mu^+\mu^- X$, where A and B are hadrons, and X represents the spectator system in the fragmentation domain. From the difference in the measured muon momenta it is found that the mean intrinsic momentum is $\langle k_t \rangle \simeq 0.85GeV/c$, almost independent of $\sqrt{s}$ and q^2 [11].

- **Running coupling constant.**

As discussed in §1.2 the strong coupling constant decreases with increasing q^2. This favours low p_t interactions and therefore increases the power n. It has been estimated that this may increase n by ~1 [13].

- **Evolution of the Structure functions.**

As the momentum transfer increases the structure functions become softer as more

partons are "seen" to share the momentum of the hadron. Fig. 1.6 shows the evolution of the structure functions, expressed here as $F_2(x, q^2) = x(f_q + f_{\bar{q}})$, with q^2 [14]. This results in a further suppression in the cross-section with increasing

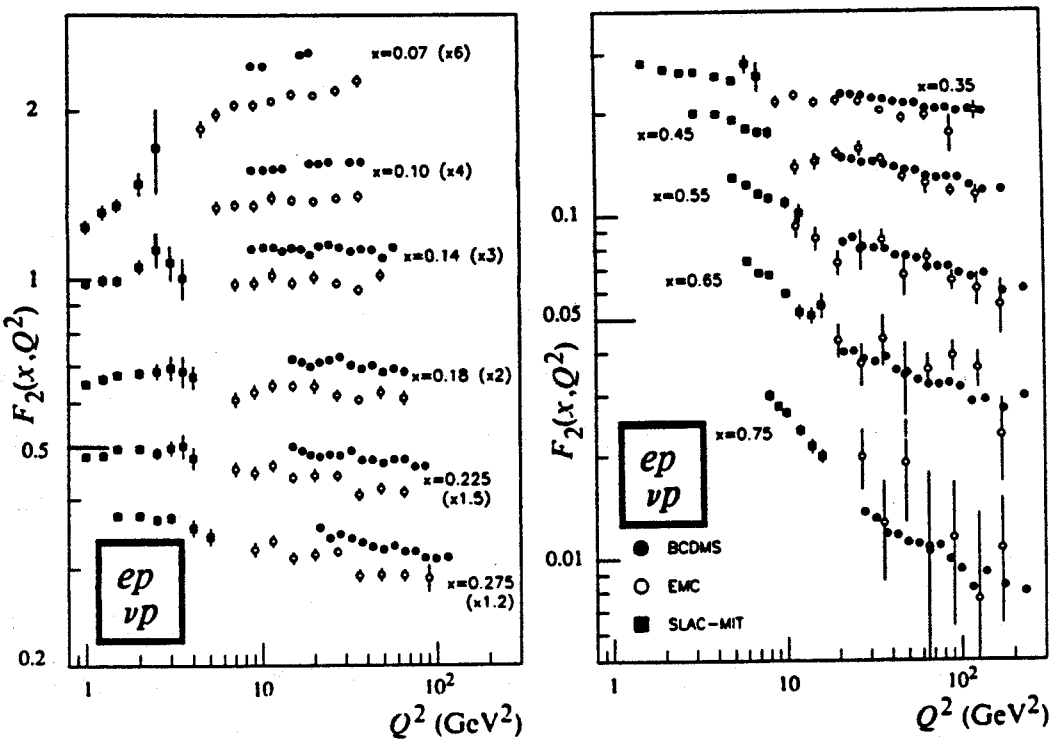

Figure 1.6: Evolution of the proton structure functions with q^2

p_t.

- **Fragmentation functions.**

The scale invariant fragmentation function $D_c^C(z, q^2)$ gives the probability that a parton, c, from the collision will fragment to produce a hadron, C, having a fraction z of the momentum of c, where $(0 \leq z \leq 1)$. Scaling violations result from the emission of gluons by c, which if they are of sufficient momentum can themselves fragment to form $q\bar{q}$ pairs. Together, the scaling violations from the structure and fragmentation functions add of the order of unity to the power, n.

At the collider, $n \sim 8 - 9$ $(p_t < 10GeV/c)$ and shows a slow decrease with increasing $\sqrt{s}$, as discussed in chapter 5.

2. The Experiment

2.1 The CERN Spp̄S Collider

The operation of the Spp̄S during autumn 1987 is described. Since then many of the numbers quoted have been improved upon. Protons produced by electrical discharges in hydrogen gas are accelerated to 50MeV by a linear accelerator and are then transferred to the Proton-Synchrotron Booster ring (PSB). This injects the protons into the Proton-Synchrotron (PS) with 800MeV energy where they are further accelerated to $26 GeV$ (Figure 2.1). These protons are mostly used in the production of anti-protons. They are directed onto a high density, water-cooled, iridium target where antiprotons are produced with a yield of about 4×10^{-6} $\bar{p}$ per incident proton [16,17]. The divergent $\bar{p}$ beam produced is incident on the end of a 20mm diameter lithium rod carrying a current of 420kA which magnetically focusses the beam. The anti-protons then pass into the Anti-proton Collector (AC) via an RF de-bunching cavity. In the AC the spatial and momentum spreads of the beam are reduced by a factor of ~500, by Stochastic Cooling [18]. Beam pick-ups detect antiprotons with momenta different from the mean and send a signal to diametrically opposite compensation magnets which apply a correcting force. After re-bunching to facilitate efficient transfer, they pass to the Anti-proton Accumulator (AA) where the phase-space is further compressed giving a total reduction factor of 10^8. Accumulation proceeds at a rate of up to 1.5×10^{10} $\bar{p}$/hour, a factor of four below the design limit. By thus separating the collection and cooling of the antiprotons, a peak luminosity of $\mathcal{L} \approx 5 \times 10^{29} cm^{-2} s^{-1}$ was

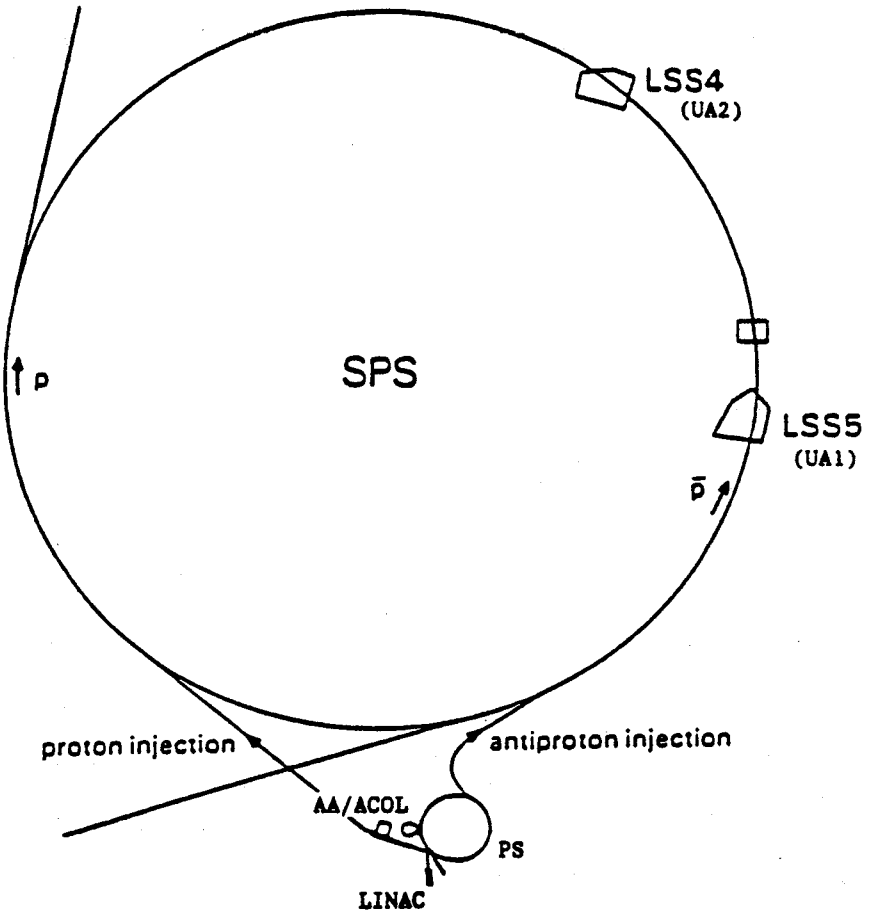

Figure 2.1: Layout of the CERN Spp̄S accelerator complex

achieved in 1987 during the first run of the Spp̄S with ACOL. [1] The maximum stack of $\bar{p}$'s in the AA is limited by intra-beam Coulomb scattering, so when $\sim 2\times10^{11}\bar{p}$'s have been accumulated they are injected at $3{\cdot}5\,GeV$ into the PS where they are accelerated to $26\,GeV$. According to the mode of operation, either three or six $\bar{p}$ bunches are then transferred to the Spp̄S which already contains the same number of proton bunches. Acceleration of p's and $\bar{p}$'s takes place simultaneously to the final energy of $315\,GeV$, corresponding to $630\,GeV$ in the centre of mass frame, such that the bunch crossing time is $7{\cdot}6\mu s$ (3 bunches) or $3{\cdot}8\mu s$ (6 bunches).

[1] This figure reached $2{\cdot}5\times10^{30}cm^{-2}s^{-1}$ in 1989 as the machine performance was improved.

The expected rate for a physical process with a cross-section, σ is given by

$$\frac{dN}{dt} = \sigma\mathcal{L} \tag{2.1}$$

where the luminosity, $\mathcal{L}$, is a property of the operating conditions of the collider, defined as

$$\mathcal{L} = \frac{N_p N_{\bar{p}} f}{A} \tag{2.2}$$

N_p and $N_{\bar{p}}$ are the numbers of protons in each bunch, f is the bunch-crossing frequency, and A is the effective cross-sectional area of the beams. The luminosity decreases such that the Sp$\bar{\text{p}}$S needs to be refilled approximately daily.

2.2 The UA1 Detector

Prior to a discussion of the UA1 experiment itself the coordinate system used should be clarified. The beam-pipe lies along the x-axis with antiprotons travelling in the positive x direction. Positive y is vertically upwards, and positive z is outwards from the centre of the ring. In addition, four angles are used (fig. 2.2): the dip-angle ($-\pi/2 < \lambda < \pi/2$), azimuthal angle ($-\pi < \phi < \pi$), x-axis polar angle ($0 < \theta < \pi$) and the angle in the xy or projected plane ($-\pi < \Phi < \pi$).

In order to measure accurately transverse momentum and missing energy the detector (fig. 2.3) was designed to be as hermetic as possible. The total energy and momentum are more difficult to measure since many of the particles produced in $p\bar{p}$ interactions remain inside the beam-pipe. Charged particle tracking and momentum measurement is performed by a large cylindrical multiwire drift chamber, known as the Central Detector or CD. This is discussed in detail in subsequent chapters. A lead-scintillator electromagnetic calorimeter surrounding the CD was removed following the 1985 Sp$\bar{\text{p}}$S run to make way for a fine-granularity Uranium-TMP calorimeter, currently under construction as part of the UA1 upgrade. Around the electromagnetic calorimeter a water-cooled aluminium coil produces a uniform dipole field of up to 0·7T in the z direction.

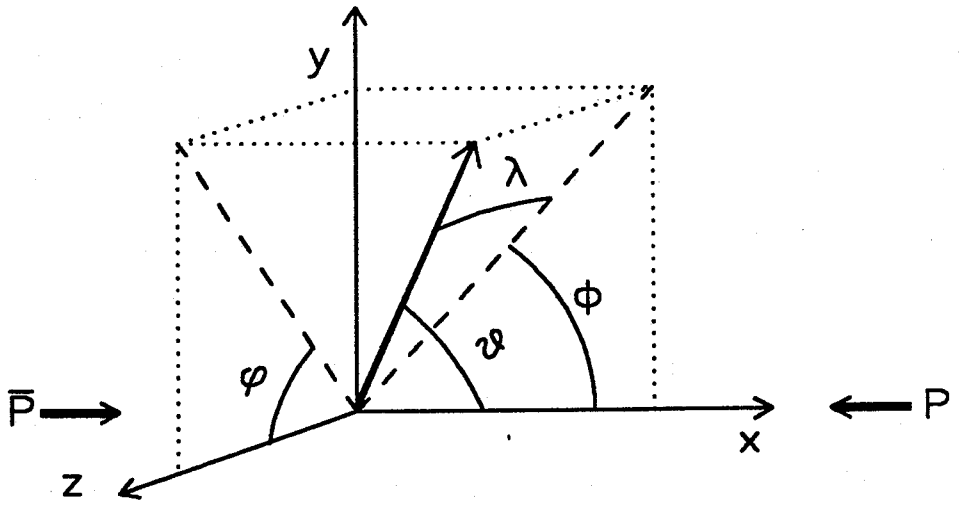

Figure 2.2: UA1 coordinate system

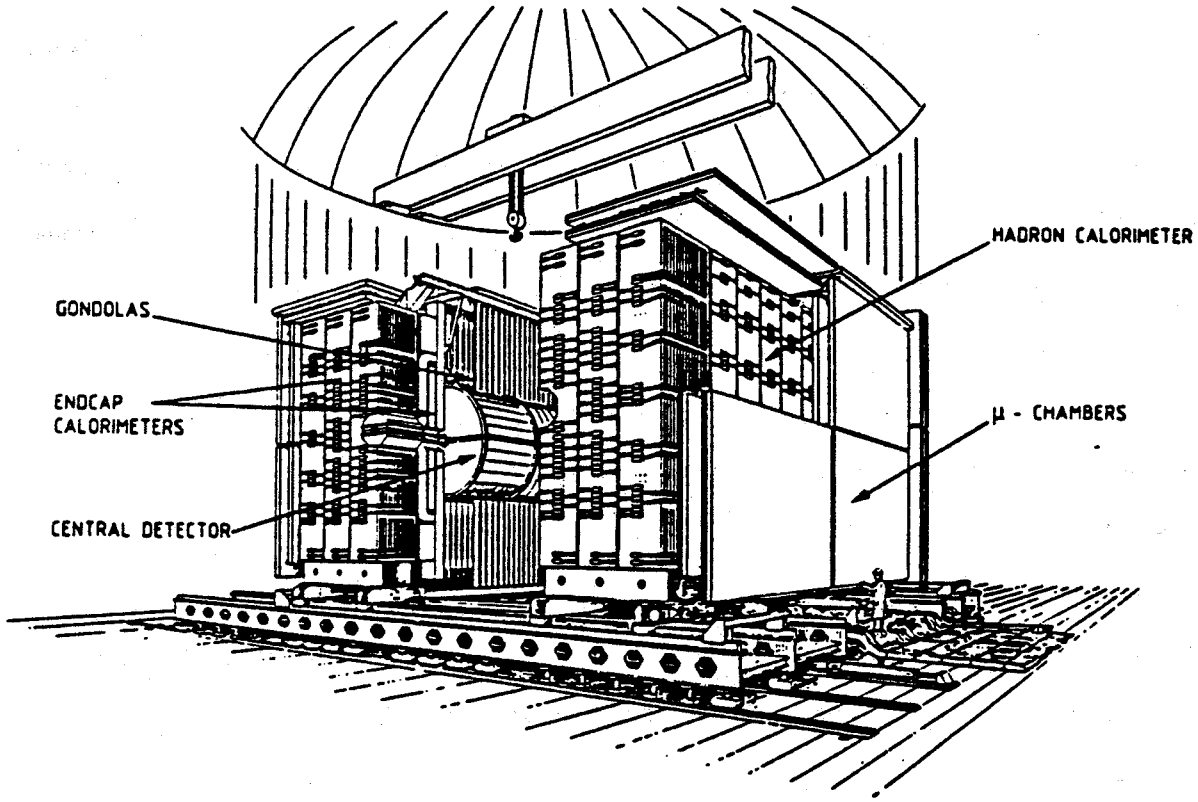

Figure 2.3: UA1 detector

To measure hadronic energy, UA1 has an iron-scintillator sampling calorimeter covering almost 4π in solid angle [19], which also acts as the return yoke of the magnet. Surrounding the coil, twenty C-shaped modules cover the range 25°–155° in polar angle. Each module is subdivided into twelve cells in azimuth. These have two samplings in depth corresponding to a total thickness of iron of $0{\cdot}75m$ ($5{\cdot}0/\sin\theta$ absorption lengths). End caps in the form of 8×8 arrays of thicker cells ($1{\cdot}1m$ or $7.1/\cos\theta$ absorption lengths) extend the polar angle coverage to within 5° of the beam. The acryllic scintillator sheets of each sampling are readout by photomultiplier pairs via BBQ wavelength shifter bars and plexiglas light guides. The shower position may be determined by the method of light-division. The hadronic energy resolution is $\Delta E/E = 80\%/\sqrt{E(GeV)}$.

Iron shielding, partially instrumented with limited-streamer or Iarocci tubes [20], lies between the Hadron Calorimeter and the muon chambers [21,22]) which surround the detector. The latter are gaseous drift chambers, of total area $700m^2$, designed to detect the penetrating muons from vector boson and heavy flavour decays. Each muon drift cell is a self-supporting extruded aluminium tube $150mm \times 45mm$ in section and 4–$6m$ long, containing a 40% argon, 60% ethane gas mixture. A single $50\mu m$ stainless steel anode wire runs along the central axis of each tube while three copper strips form the cathode and also shape the field. The tubes are joined to form planes with four layers of chambers in mutually orthogonal pairs. These are staggered to help resolve left-right ambiguities and to minimise the dead space between cells. There are two planes separated by $60cm$. The spatial resolution of an individual chamber is between $0{\cdot}2mm$ and $1{\cdot}0mm$. For high p_t muons, the angular resolution at the event vertex is $\sim 4mrad$, which is limited by multiple scattering in the iron.

Large sheets of scintillator partially cover the muon chambers. These are used for triggering on cosmic-ray muons which are used to calibrate the hadron calorimeter and study systematic effects in the Central Detector.

2.3 The Trigger

The UA1 trigger selects $p\bar{p}$ interactions according to their physics content and rejects such backgrounds as beam-halo or beam-gas interactions. It comprises a pre-trigger and three further levels of increasing selectivity. The first, second and third level triggers were not used in this analysis. The Pre-Trigger [23] provides a reference time for all UA1 systems. Passive pick-up coils, known as SPS directional couplers, are placed close to the beam about $20m$ from the beam intersection point to detect the incoming beams. These signals are sent to the counting room via air-dielectric coaxial cables, where they are used to define the zero time (machine crossing) signal for the experiment. The pre-trigger also signals inelastic $p\bar{p}$ interactions using precise timing information from the SPS and Very Forward (VF) hodoscopes. The former consist of two 10-element arrays of scintillator at x=$\pm 6m$ covering a rapidity [2] range of approximately $\pm(3{\cdot}5\text{–}5{\cdot}3)$; the latter, at $\pm 12m$, have four elements covering $\pm(4{\cdot}3\text{–}6{\cdot}6)$ in rapidity (fig. 2.4). Events are vetoed in which hits are recorded early in the hodoscopes (with respect to the minimum possible time for particles coming from the interaction point). Thus, beam-gas interactions upstream or beam halo particles which trigger the hodoscopes on the way in are rejected. Hits in the hodoscopes consistent, within $\pm 20ns$, with particles coming from the interaction point are said to be in-time.

The SPS and VF counters provide a minimum-bias (also called non-single diffractive) trigger by requiring an in-time hit in either the SPS or the VF hodoscopes on *both* the p and the $\bar{p}$ sides. The minimum-bias cross-section may be written:

$$\sigma_{\rm MB} = \sigma_{p\bar{p}}^{tot} - \varepsilon_{SD}\sigma_{SD} - \varepsilon_{DD}\sigma_{DD} - \sigma_{EL} \tag{2.3}$$

[2] The rapidity, y, of a particle is defined as

$$y = \frac{1}{2}\ln\frac{E + p_L}{E - p_L}$$

where E and p_L are the energy and longitudinal momentum respectively.

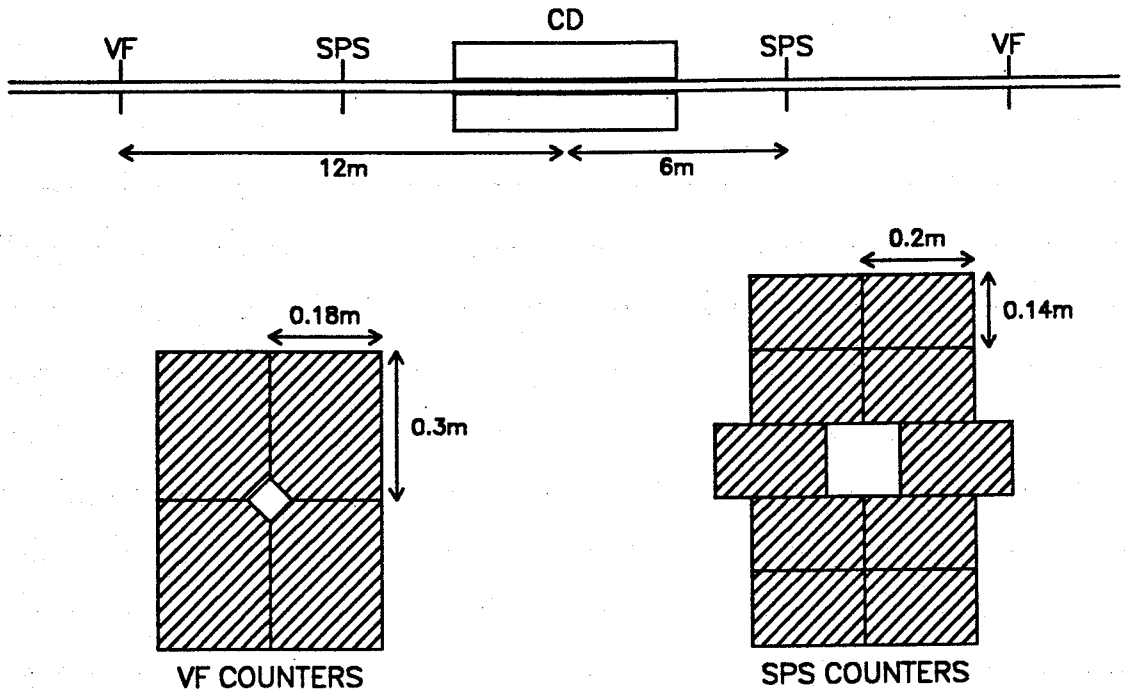

Figure 2.4: Pre-trigger hodoscopes

where σ_{SD}, σ_{DD} and σ_{EL} are the single-diffractive, double-diffractive and elastic cross-sections and ε_i are the trigger inefficiencies for each process. Very few single-diffractive interactions satisfy this trigger ($\varepsilon_{SD} > 99\%$) and only a small proportion of double-diffractive events are completely contained within the beam-pipe ($\varepsilon_{DD} \sim 8\%$). Using the measured cross-sections of UA4 and UA5 [24,25], and allowing for the hodoscope efficiencies [26], the minimum-bias cross-section is found to be

$$\sigma_{\rm MB} = (37.1 \pm 2.6)mb \tag{2.4}$$

The mean number of interactions per bunch crossing, given by eq. 2.1 with $\Delta t = 3.8\mu s$, is $\sim$0·05 for the luminosities in 1987 (typically, $\mathcal{L} \sim 5 \times 10^{29} cm^{-2} s^{-1}$), from which the fraction of events containing a double interaction [27] is less than 0·3%.

2.4 Data quality

Beam-scrapers are used to remove those particles travelling on slightly different orbits from the main bunches. At the start of 1987, the aperture of the SpS beam-scrapers at the injection point was increased to improve the transfer efficiency from the PS. This resulted in poor beam conditions with large amounts of out-of-time beam-halo accompanying the proton bunches, producing hits in the trigger hodoscopes and unassociated tracks in the CD. The problem was exacerbated by interactions in a narrow section of beam-pipe which was installed in preparation for the Uranium-TMP Very-Forward calorimeter.

Timing information from the SPS hodoscopes reveals contamination from false triggers. The recorded time of the hits in the p-side SPS hodoscope with respect to the hit in the $\bar{p}$-side hodoscope is shown in fig.2.5 for (a) noisy, and (b) clean beam conditions. The peak at zero corresponds to in-time hits on both sides due to

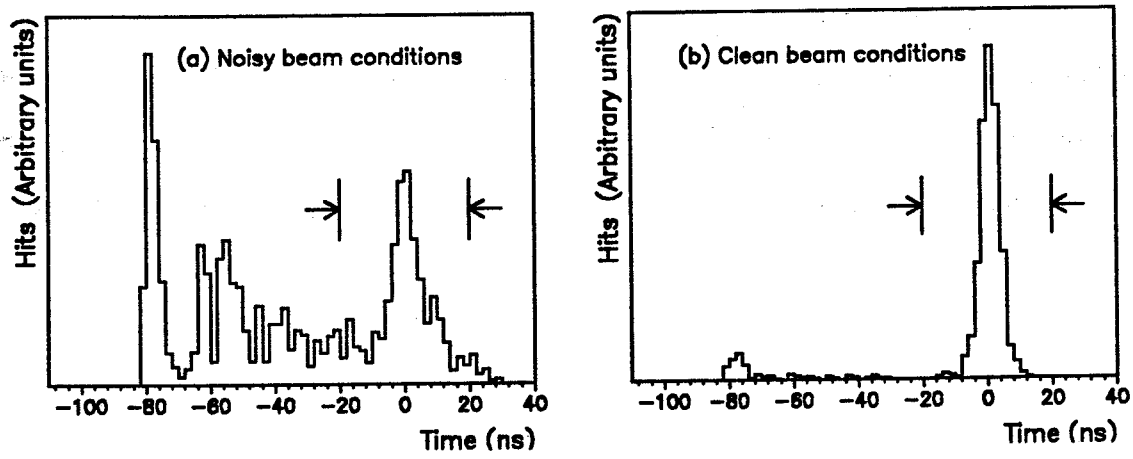

Figure 2.5: Timing of SPS hodoscope hits on the incoming p-side.

particles coming from the interaction point (the arrows show the timing acceptance window). The second peak at $-80ns$ is due to proton beam-gas interactions, which give an early hit in the p side hodoscope. The background before and under the in-time peak in fig.2.5(a) is due to either late hits on the $\bar{p}$ side or early hits on the p side, which are both caused by stray particles following the main proton

bunches. In many cases these triggers were rejected offline by the CD primary vertex requirement. A residual contamination, however, is possible when a single-diffractive event produces a hit on one side simultaneous with a false in-time hit on the other.

In addition to these false triggers, a background of unassociated tracks and electrical pick-up from the beam [28] makes the track-finding in the CD more difficult. Noise in the CD also results in systematic shifts of the tracks in z. At worst, the mean charged track multiplicity is reduced by almost 20%, with 25% more tracks found in $-z$ than in $+z$, compared to clean beam conditions. [3] A systematic study of the reconstructed tracks and the SPS hodoscope timing plots covering the whole data sample, showed that the problems were concentrated at the beginning of the 1987 run after which time the beam conditions improved considerably. Therefore, no data taken prior to 26.11.1987 (run number 20305), consisting of $2{\cdot}8\times10^5$ events, were used in this analysis. The systematic z asymmetry was, however, present throughout the run though it was considerably smaller when the beam was clean. A fiducial cut was therefore applied to all charged tracks, removing the most affected region close to the beam. For the remaining tracks, a phenomenological correction was possible. This is described in more detail in chap. 4.

[3] With good beam conditions, the charged track multiplicity, transverse momentum, ϕ and η distributions were consistent with the pre-ACOL data of 1985.

3. The Central Detector

3.1 Construction of the Central detector

The Central Detector, or CD, is a cylindrical multiwire drift chamber $5{\cdot}8m$ long and $2{\cdot}2m$ in diameter with a polar-angle coverage of 5° to 175°[29,30]. The gas mixture is 40% argon and 60% ethane, which was doped at times with $1ppb$ of Tetra-Methyl-Phenylene-Diamine (TMPD) to increase the electron yield from the light of the calibration lasers. The CD is divided into six self-supporting half-cylindrical chambers 1·93m in length. The outer shell consists of a honeycomb structure sandwiched between two layers of Vetronite and strengthened with Stesalit bars. The rectangular central plane and semi-circular end planes are made from Plexiglass foam. This design maximises the rigidity while minimising the number of radiation lengths of the chamber walls. The wires, between $0{\cdot}8m$ and $2{\cdot}2m$ long, run parallel with the magnetic field direction. They are arranged in planes 18cm apart held at alternately high and low electrical potential. The region between two planes is known as a drift volume. In each central chamber there are five vertical drift volumes and a single horizontal volume, known as a "green" chamber, adjacent to the beam-pipe. The four forward chambers have six horizontal drift volumes. For a typical $p\bar{p}$ event this configuration gives, throughout the detector, a roughly constant density of points along each track. The cathode plane is common to adjacent drift volumes, and comprises $150\mu m$ gold-plated Cu-Be wires at $5mm$ intervals, held at typically $-28kV$. Three wire planes, $6mm$ apart, constitute the anode. The outer layers are alternately $100\mu m$ gold-plated Cu-Be field-shaping wires at $-2kV$, and $35\mu m$ Ni-Cr sense wires at zero potential,

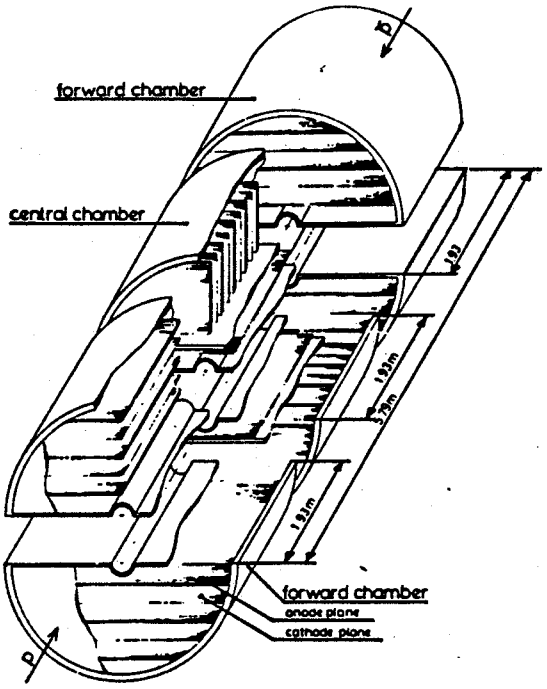

Figure 3.1: The UA1 Central Detector

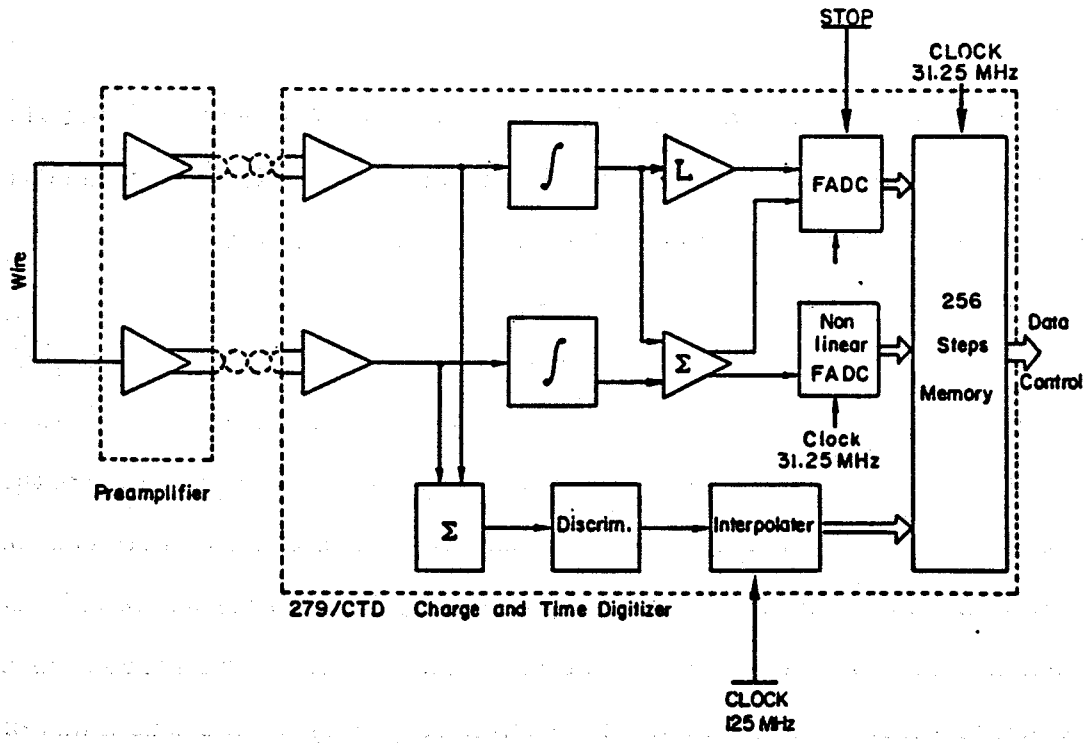

Figure 3.2: CD Readout System

spaced $5mm$ apart. The position of an individual sense wire in a plane is known to within $50\mu m$. The intermediate field plane is made from $150\mu m$ gold-plated Cu-Be wires at -2·5kV. These control the gas gain and compensate for the electrostic deflection of the field and sense wires in the drift field. Electric field edge effects are minimised by arrays of conductive strips on the chamber walls, set at a uniformly graded potential by means of resistive voltage dividers. The magnetic field is constant throughout the detector to better than 1%.

The readout electronics chain is shown in figure 3.2. The sense wires are instrumented at both ends. The signals pass through pre-amplifiers mounted on the chamber before travelling along approximately $50m$ of cable to the counting room. An integrating unit, clocked at $31{\cdot}25MHz$, records the incoming charge in $32nsec$ time intervals. The sum, $(Q_L+Q_R)_i$, of the charges from the left and right ends of the wire, and from the left side alone $(Q_L)_i$ are formed (where i denotes the sampling period), and fed as input to a linear-response Fast Analogue to Digital Converter (FADC) designed to produce as output:

$$z_i = \frac{(Q_L)_i}{(Q_L+Q_R)_i} \tag{3.1}$$

which is the z-coordinate expressed as a fraction of the wire length. Since the error in the z_i measurement is larger in the tails of the pulse, the final value of z is taken as the energy-weighted average of the individual samplings:

$$z = \frac{\sum z_i E_i}{\sum E_i} \tag{3.2}$$

Five time periods, corresponding to a total of $160nsec$, are used to measure z with a resolution of $\geq$1·6% of the wire length, which is limited by the 6-bit precision of the FADC. A single non-linear FADC measures the summed charge from both ends of the wire to give the total charge (ultimately the energy loss dE/dx) accurately over a wide range. In parallel with the integrators, the left and right signals are summed and discriminated. A Time to Digital Converter (TDC) on the discriminator output is strobed at $125MHz$, measuring the time of arrival of the pulse to an

accuracy of $4nsec$. The vast amount of data ($\sim$ 160MBytes/event) from the CD is reduced to a manageable amount by dedicated Readout-Processors (ROP's). Each reads the data from sixty wires and passes the hit information to the data-acquisition system.

3.2 Operation of the Central Detector

Particles traversing the detector release electrons by primary ionisation of the gas, which drift at a uniform velocity v_d in the electric field towards the anode plane. The magnetic field deflects the electrons by an angle α, which increases the drift time slightly. The drift gap of $18cm$ allows the total charge to be collected in $3{\cdot}6\mu s$ (for B=0·7T) — less than the beam-crossing time of $3{\cdot}8\mu s$ for six bunch operation. In the high field close to the sense wire the electrons accelerate creating an avalanche of electrons by secondary ionisation, with a gas gain of 10^5, producing a signal or "hit" on the wire. The positive ions drift slowly to the cathode where they are neutralised. Space charge of low-mobility positive ions near the sense wires can accumulate from previous events resulting in local changes in v_d, α and the gas gain [35]. These are collected on the intermediate field plane and create no problem at 1987 luminosities. Ultra-violet photons produced by recombining argon ions are prevented from creating spurious showers elsewhere in the CD by the quenching properties of the ethane. The (x, y) hit coordinates are given by the wire position and the drift time and the z-coordinate by charge division (see §3.1). The position resolution of individual hits is $\sim 300\mu m$ in the xy-plane and 1·7% of the wire length in z.

Radiation damage to the CD can result in a degraded chamber performance. Ageing effects, due to field distortions caused by organic depositions on, and damage to, the wire surfaces, are expected to occur when the integrated charge collected on a wire reaches about $1Cm^{-1}$ [36]. At the start of the 1987 run, the wires in the Green chambers and those close to the beam-pipe were approaching

this figure. The first symptom of ageing is a drop in the pulse-height, followed by the onset of a continuous corona discharge ultimately leading to complete breakdown, or sparking, whereupon the chamber is unusable. In anticipation, the gas gain of the chamber was reduced fourfold and the pre-amplifier gain was increased correspondingly to keep the signal optimally in the range of the FADC's. This unfortunately increased the noise contribution to the pulse. Fig. 3.3 shows a comparison of the single hit pulse-height for data taken before and after the 1987 run. No decrease is seen in the pulse size. The long tail for the 1988 data is due to the increased noise relative to 1985. Comparisons of regions of high and low irradia-

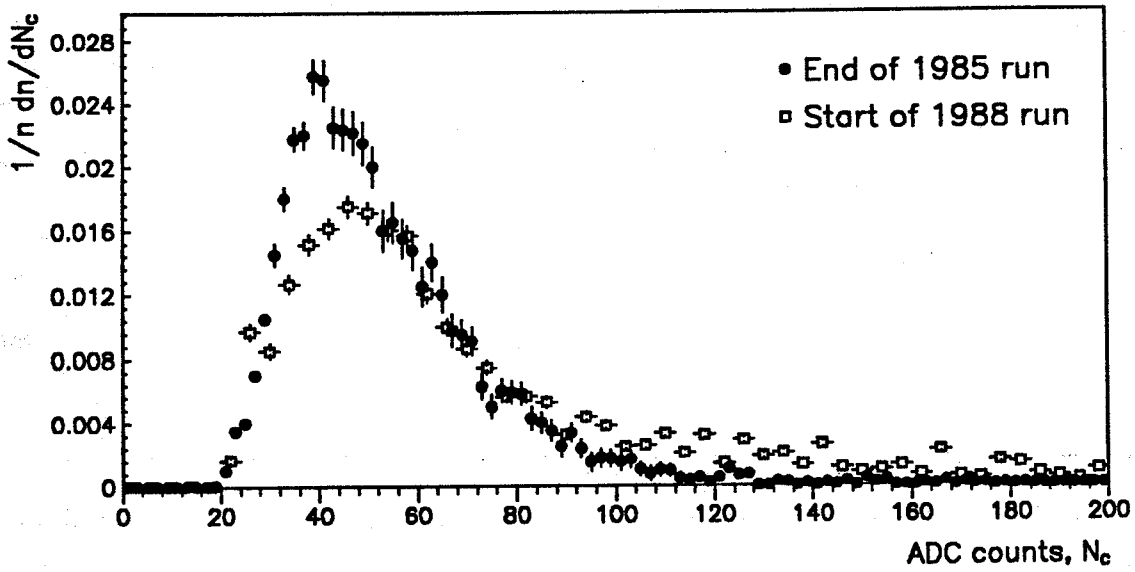

Figure 3.3: Single hit dE/dx in ADC counts

tion, and of data with positive and negative polarity magnetic field, revealed no systematic differences in the pulse-height spectra. Furthermore, no increase in the dark current of the chamber was observed up to the end of the 1987 run. Thus, although the CD did not noticeably suffer from ageing during the 1987 run the reduction in the gas gain reduced the signal to noise ratio of the hits.

3.3 Charged Track Reconstruction

The charged track reconstruction comprises two distinct operations — track-finding and track-fitting. The former uses xy information only and proceeds by associating sets of up to eight hits in short track segments which are then combined to form full length tracks [34]. Unassociated hits are flagged as background due to detector noise. The track fitting assumes that the particle has a helical trajectory which, projected in the bending plane, forms the arc of a circle of radius

$$R_{xy} = \frac{p.\cos\lambda}{0.2998B} \tag{3.3}$$

where p is the momentum in GeV/c, λ is the dip angle of the helix with respect to the xy-plane (fig.2.2), and B is the magnetic field in Tesla. The component in the direction of the field is expressed as

$$z = c_1 s + c_2 \tag{3.4}$$

where s is the track length in the xy-projection; c_1 and c_2 are constants to be determined. The track fit may be factorised due to the two orders of magnitude difference in the relative accuracies of xy and the z measurements. Thus, the problem is reduced to two independent fits with three free parameters (*e.g.* the circle centre and radius) in the xy-plane and two (c_1 and c_2) in sz-space. Both fits use the method of least squares, combining the statistical errors (from studies of the track residuals) and systematic errors (from studies of cosmic rays) of each hit in quadrature. The typical momentum resolution is $\Delta p/p = 0{\cdot}01p(GeV/c)$ with a two-track resolution of $\sim 5mm$.

Fig. 3.4 is a graphical representation, in the xy plane, of an event in the CD showing the raw hits (above) and the acceptable reconstructed tracks (below).

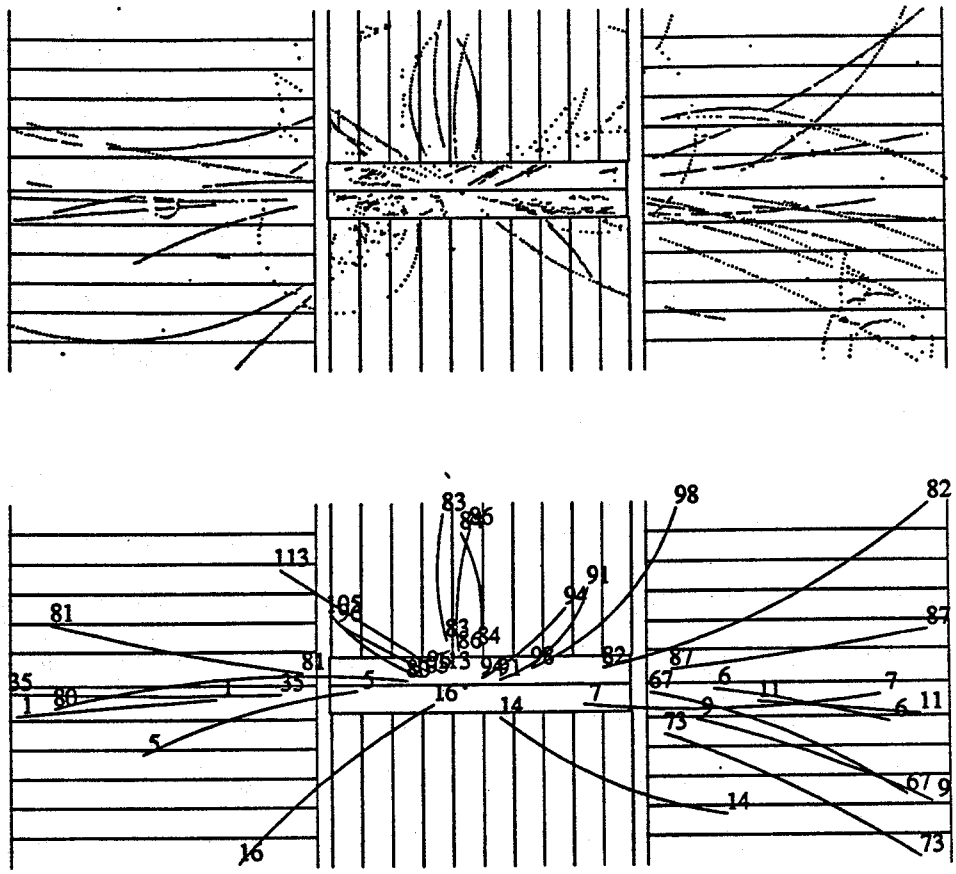

Figure 3.4: Event display of the CD showing raw hits and reconstructed tracks in the xy-plane.

3.4 Vertex Finding

The V^0-finding method used requires the primary event vertex and the V^0 decay point to be carefully measured. Since the beam position is well defined the primary interaction vertex is accurately known in the transverse plane. The length of the p and $\bar{p}$ bunches in the x-coordinate results in a large spread in the x coordinate of the primary vertex. The primary $p\bar{p}$ interaction vertex and secondary vertices from particle decays and interactions in the chamber are found using the reconstructed track information [33]. If a clear peak is seen in the x-coordinate distribution of the extrapolated tracks, evaluated on the beam axis, then its mean is used for the x position of the primary vertex. A double peak is indicative of two $p\bar{p}$ interactions in the same event. If no vertex candidates are forthcoming a bubble-method is used. For each track, the number of tracks passing within a bubble of radius $5mm$ centred at the x crossing point of the track with the beam-line are counted. If a bubble has more than five tracks passing through it then it is considered to be a vertex. If no vertex is found then the number of tracks required is reduced to three and, if still no candidates result, the bubble size is increased to $10mm$. The x and y coordinates of the vertex(ices) found are then accurately fitted using all the associated tracks. The x and y vertex distributions are shown in figure 3.5. The z coordinate of the vertex is $z = 0$, by definition, since no improvement on the nominal beam-position is possible using the charge-division coordinate.

A secondary vertex search is made within $10mm$ in the xy-plane of the end points of tracks from the primary vertex which terminate in the CD. A successful vertex candidate must have have three or more associated tracks each with a radius of curvature $R_{xy} > 1.0m$ ($p_{xy} > 210MeV/c$). Similarly, an attempt is made to find secondary vertices by examining the starting points of all the unassociated tracks. These tracks must have $R_{xy} > 0.5m$ ($p_{xy} > 105MeV/c$). As many as six tracks may be demanded if the secondary vertex candidate is close to an established vertex or the beam-line.

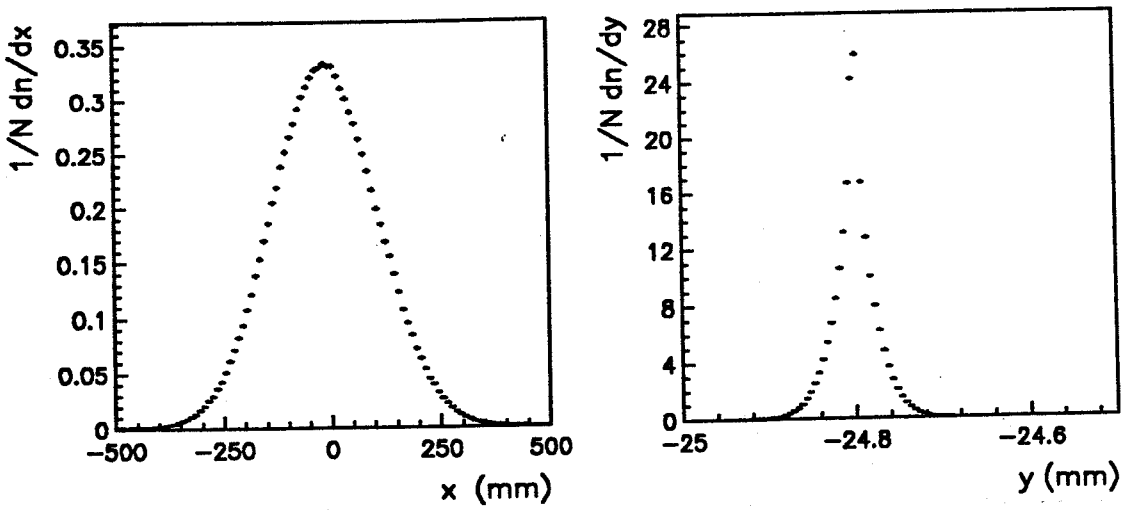

Figure 3.5: Primary vertex distributions in x and y

Finally, a search is made for two-track vertices from the decays of neutral V^0 particles. The method used is discussed in detail in chapter 6. There may still be unassociated tracks from, for example, beam-halo, cosmic rays, or split low-energy tracks such as electron spirals. All tracks are written in data banks according to whether they are associated to a primary vertex, a secondary vertex, a V^0 vertex, or no vertex at all.

4. Calibration of the Central Detector

4.1 Standard calibration procedure

The task of maintaining a good calibration of the CD is a difficult one because the number of channels is large and since it is sensitive to systematic effects on a short timescale. Slight changes in the field or gas composition, if not carefully monitored, can easily lead to large errors during track reconstruction.

The statistical errors in the CD are found by studying the residuals of the fitted tracks with respect to the raw data points, in the xy-plane and the z-coordinate. These tend to be relatively stable in time. The systematic errors are less accessible but may be minimised through continuous monitoring and re-calibration. The voltages applied to the wires and the field-shaping copper strips are monitored, ensuring that they are kept at the values originally selected to give a uniform field in the CD. Calibration is performed at two levels: chamber by chamber on a daily basis and wire by wire, typically twice weekly. The former monitors the effects of global changes, such as gas composition and pressure, and magnetic field, which affect the re-measurement of the drift velocity v_d, the drift angle α, and the drift reference time t_0. Real data tracks are used, fitted as usual but with v_d, α and t_0 as additional free parameters. In each chamber many tracks at different orientations are used. The fact that the drift directions are opposite in adjacent drift gaps is exploited to provide constraints for the fit.

Close to the sense-wire the shower no longer moves with constant v_d and α, but accelerates directly towards the wire. Since the drift-time is measured from the start of the pulse, tracks with different orientations will have slight systematic

differences in their measured xy-positions. An angular correction factor is calculated to account for this effect. A time-slewing correction is also calculated to account for a slight dependence of the drift-time measurement on the dE/dx or signal size. Smaller signals will tend to be shifted to slightly later times as a result of the ADC threshold, which cuts above the pedestal. This correction is applied hit-by-hit depending on the total signal size above threshold.

The channel by channel calibration, also using real tracks, exploits the expected symmetries of the event. The measured z, and dE/dx distributions for all wires are compared, enabling wire-by-wire corrections to be made for gain differences and charge-division offsets. A good xy measurement requires a well calibrated t_0, corresponding to the limit of zero drift length. For each wire the time spectrum of all hits is plotted. The spectrum is flat for the bulk of the drift volume with a small enhancement for tracks passing close to the wire but on the opposite side to the drift volume. The t_0 is defined as the time half way up the rising edge of the spectrum thereby giving the same relative timing for all channels.

A laser calibration system was installed and successfully tested in the 1987 run [37]. Four nitrogen lasers were used to produce straight tracks in one module of the CD for the study of systematic space charge distortions occurring at high luminosities. An ionisation seed, TMPD (Tetra-Methyl-Phenylene-Diamine), was introduced to the gas at the ppb level which is an insufficient concentration to cause ageing. The luminosities achieved in 1987 were, however, too low to cause space-charge problems so no laser corrections were applied to the data.

4.2 Charge division asymmetry

The z-coordinate is obtained using the method of charge division by measuring the total charge, q_T, collected and that on the left $(-z)$ side, q_L. The full expressions for the left signal, Q_L, and the total, Q_T, input to the FADC's are then

$$Q_L = g_L q_L + \delta_L + \sigma_1 \tag{4.1}$$

$$Q_T = (g_R q_R + \delta_R) + (g_L q_L + \delta_L) + \sigma_2 \tag{4.2}$$

where g_L and g_R are the left and right gains, δ_L and δ_R represent the random noise in the chamber and the electronics and $\sigma_1 \approx \sigma_2$ is the D.C. offset of the FADC input. The measured distance ξ, normalised to the wire length $2w$, of the hit from the right $(+z)$ side of the chamber is then

$$\frac{\xi}{2w} = \frac{Q_L}{Q_T} = \frac{(g_L q_L + \delta_L) + \sigma_1}{(g_R q_R + \delta_R) + (g_L q_L + \delta_L) + \sigma_2} \tag{4.3}$$

The pre-amplifier gains, set by Digital to Analogue Converters or DAC's under software control, are balanced to give a symmetrical response to large dE/dx hits for which the noise is negligible. The D.C. levels, σ_1 and σ_2, of the FADC inputs may also be adjusted via DAC's. Due to technical difficulties in calibrating these DAC settings they were set to a nominal value close to zero for all channels. With the introduction of ACOL the gas gain of the chamber was reduced by a factor of four, to prevent ageing in the chamber [36]. The gains of the pre-amplifiers were increased correspondingly in order to maintain the original FADC accuracy with the result that intrinsic chamber noise increased fourfold compared to the signal.

Expressing eq. 4.3 in terms of the standard UA1 coordinate, $z = w - \xi$, gives the measured z value:

$$\frac{z_{\text{meas}}}{w} = \frac{(g_R q_R - g_L q_L) + (\delta_R - \delta_L) + (\sigma_2 - 2\sigma_1)}{(g_R q_R + g_L q_L) + (\delta_R + \delta_L) + \sigma_2} \tag{4.4}$$

With neither noise nor D.C. offsets, this expression gives the true position of the hit:

$$\frac{z_{\text{true}}}{w} = \frac{g_R q_R - g_L q_L}{g_R q_R + g_L q_L} \tag{4.5}$$

Equations 4.4 and 4.5 may be combined to yield an expression for the measured z value in terms of the true value:

$$z_{\text{meas}} = z_{\text{true}} - \Delta z \tag{4.6}$$

where the shift, Δz, is given by

$$\Delta z = \left(\frac{2\sigma_1 - \sigma_2}{Q_T}\right) w + \left(\frac{\delta_L - \delta_R}{Q_T}\right) w + \left(\frac{\delta_R + \delta_L + \sigma_2}{Q_T}\right) z_{\text{true}} + \mathcal{O}\left(\frac{\delta}{Q_T}\right)^2 \tag{4.7}$$

The first and third terms result in a systematic shift in the $-z$ direction while the second term simply degrades the resolution.

Figure 4.1 shows the measured distribution of hits for three bands of dE/dX. Only hits used in the xy track fit and on "good" wires are shown. The curve for

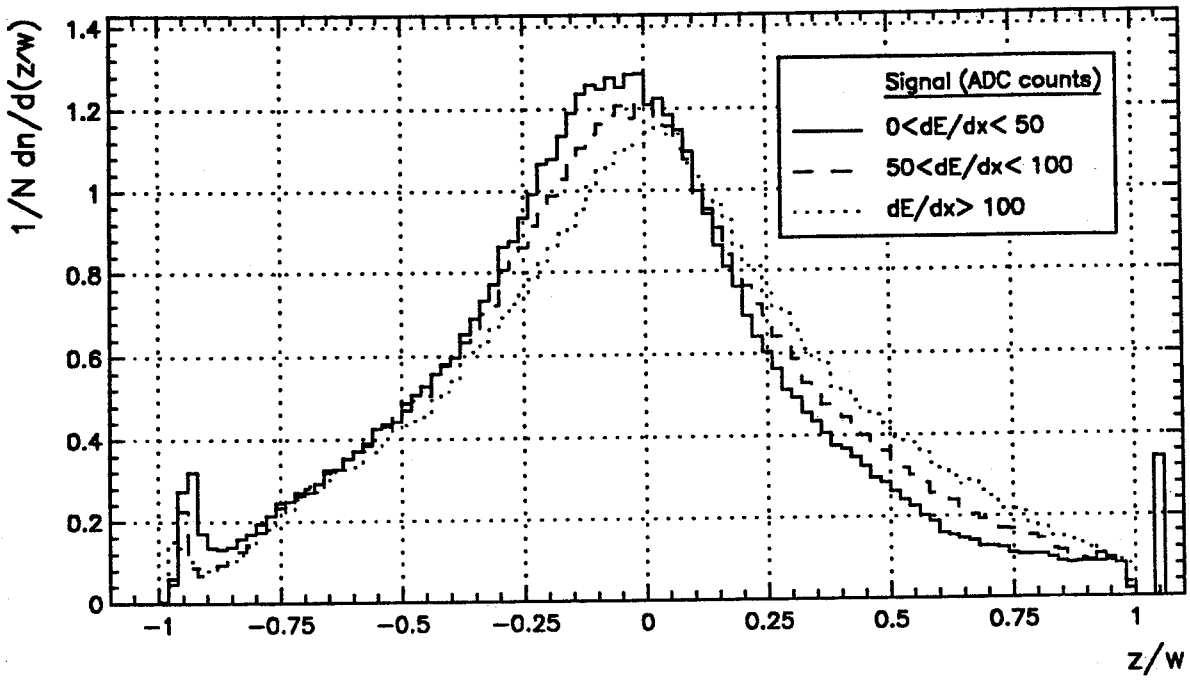

Figure 4.1: Measured z-distribution of single wire hits as function of dE/dx

large dE/dx hits is seen to be almost symmetric, with $z_{\text{meas}} \approx z_{\text{true}}$. The lower dE/dx curves, however, show the predicted systematic shift in the $-z$ direction and are slightly skewed.

No correction to the data could be made at the level of single wires (*i.e.* using the z-hit information) since, to reduce the event size, the raw hit data banks were not retained when the initial event processing was carried out. [1] Only the affected reconstructed tracks parameters, namely the momentum and the dip angle, could be corrected.

The track-finding is unaffected by this shift since only xy information is used.

[1] Fig. 4.1 comes from a small sample of re-processed events for which the raw hit banks were kept.

The track fitting, however, uses the z information to evaluate the dip angle λ, and the track momentum, $p = p_{xy}/\cos\lambda$. The measured dip angle distribution is shown in fig. 4.2. The data exhibit a systematic shift of about $20mrad$ in the direction

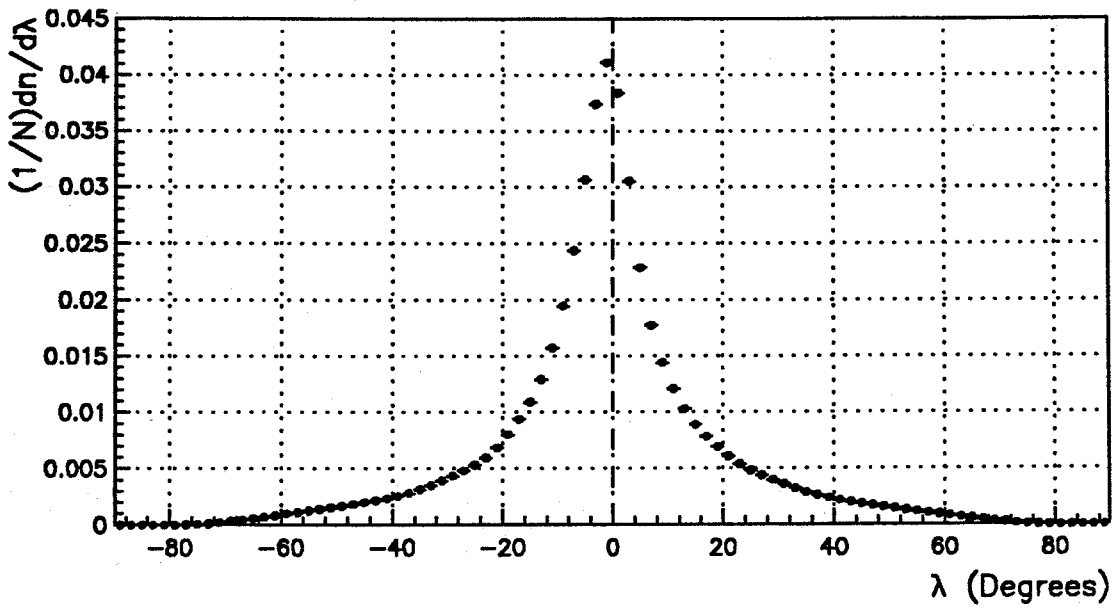

Figure 4.2: Charged track dip angle (uncorrected)

of $-\lambda$. The systematic shift in z causes an excess of tracks for $\phi \approx \pm 180°$and the depletion for $\phi \approx 0$.

The shift in the dip angle is small but since the p_t distribution is rapidly falling it is particularly sensitive to slight miscalibrations. Tracks with negative dip angle are shifted away from the bending-plane so that p_t is systematically too high; the converse is true for positive dip angles. Fig. 4.3 shows the p_t distributions for all charged tracks satisfying the basic track quality requirements (table A.1), separately for $+\lambda$ and $-\lambda$. The upward shift in the p_t for tracks with negative λ is clearly seen.

4.3 Fiducial cut in Φ

For a given p_t, the measured λ and p_t are most affected in the horizontal plane where the z coordinate is most important. Furthermore, noise associated with the

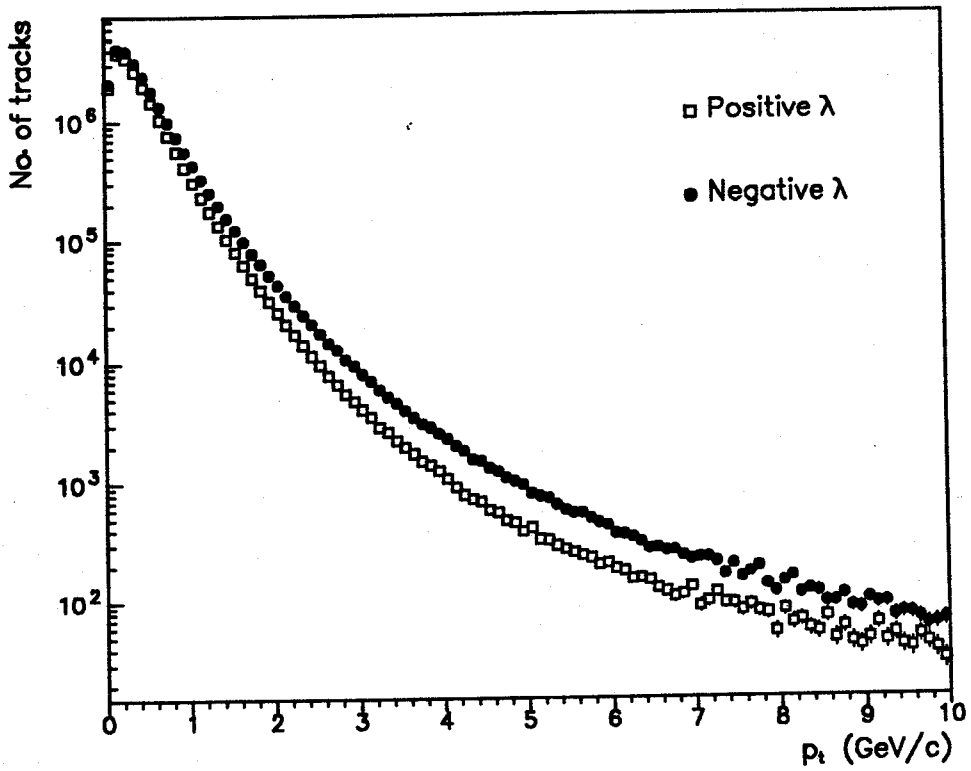

Figure 4.3: Charged track p_t spectra for $+\lambda$ and $-\lambda$ (uncorrected)

beam is greater at small Φ angles. The differences in the p_t spectra, $f^+(p_t)$ and $f^-(p_t)$ for positive and negative dip angles respectively, were studied for different regions of Φ_{wrtb} (angle in projected plane with respect to the beam). The ratio $f^+(p_t)/f^-(p_t)$ was formed to show more clearly the asymmetry. Figure 4.4 shows this ratio for (a) $0< \Phi_{\text{wrtb}} <5°$, (b) $5°< \Phi_{\text{wrtb}} <10°$, (c) $10°< \Phi_{\text{wrtb}} <20°$, and (d) $\Phi_{\text{wrtb}} >20°$. The large discrepancy between the $+\lambda$ and $-\lambda$ regions for small Φ_{wrtb} suggests the application of a fiducial cut on low angle tracks. It is appropriate to cut a *wedge* in Φ since this removes noisy *wires* which pass close to the beam. Cutting in rapidity removes a *cone* around the beam-pipe so tracks at low ϕ can still cause hits on noisy wires. Furthermore, the cut in Φ does not completely cut the acceptance at high rapidity since tracks largely in the bending plane are retained. Fig. 4.5 shows the effects of different Φ cuts on the acceptance in the $\eta - \phi$ plane. Cutting at Φ_{wrtb}=5°removes 10% of all tracks in the region η <2·5,

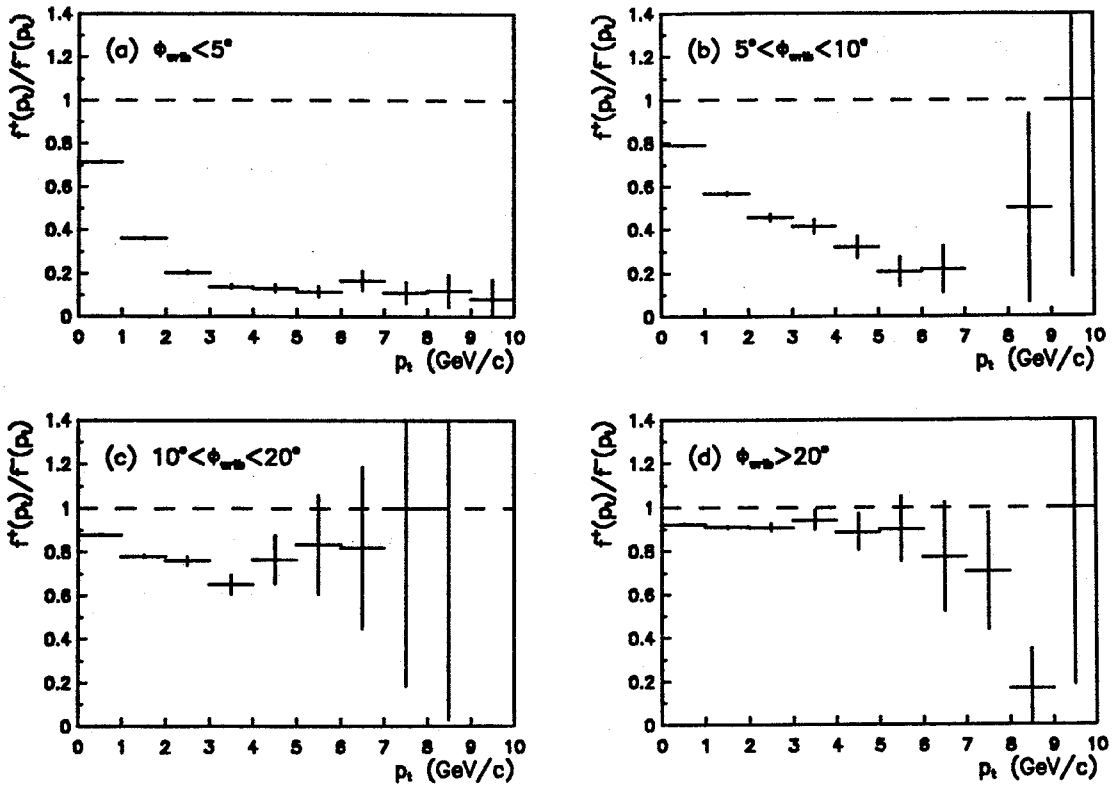

Figure 4.4: $f^+(p_t)/f^-(p_t)$ as a function of $\Phi_{\rm wrtb}$ (uncorrected)

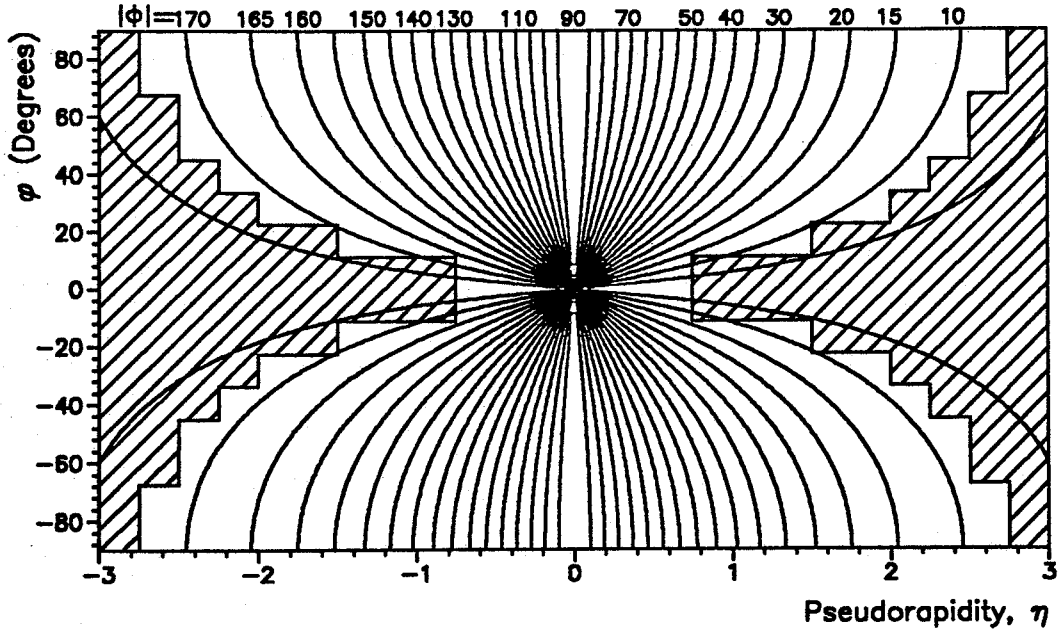

Figure 4.5: Fiducial Φ cut in the $\eta - \phi$ plane

which increases to 17·5% for $\Phi_{\rm wrtb}$=7·5°and to 25% for $\Phi_{\rm wrtb}$ =10°. The drop in the V^0 reconstruction efficiency is more dramatic since the V^0 is rejected if either of the two decay tracks is within $\Phi_{\rm wrtb}$ of the beam. A fiducial cut was therefore applied to all charged tracks by setting the CD acceptance of all those $\eta\phi$ bins to zero whose central value of $\Phi_{\rm wrtb}$ was less than 7·5° and then renormalising the other $\eta\phi$ bins in the same p_t interval (see appendix A). The hatched region of fig. 4.5 shows the effect of this cut in the $\eta\phi$ plane.

The systematic asymmetry is greatest for small $\Phi_{\rm wrtb}$ but is present for all Φ due to beam noise at low angles and electronics noise and offsets affecting the whole chamber. In the next section a correction to the track dip angle and momentum is discussed which is used in conjunction with this fiducial Φ cut.

4.4 Dip angle correction

Given that s measures the arc length of the track in the projected plane, the dip angle is calculated from the gradient of the track fit in sz-space:

$$\tan\lambda = \frac{z}{s} \tag{4.8}$$

which, by differentiation, gives the shift, $\Delta\lambda$, in the dip angle in terms of Δz:

$$\Delta\lambda = \frac{\Delta z}{s}\cos^2\lambda \tag{4.9}$$

The interpretation of $\Delta\lambda$ and Δz in this equation is not straightforward. For a single *hit*, Δz may be calculated from eq. 4.7 to predict the shift in the dip angle $\Delta\lambda_{\rm hit}$ using eq. 4.9. The λ measured in the sz fit is, however, the dip angle of a *track* coming from a fit including many hits. Since it is not possible to propagate the combined effects of many different hit corrections to predict the effect on the dip angle and track momentum, a more empirical method was used.

Eq. 4.7 gives the shift Δz of a single hit to be a linear function of z. From eq. 4.9 a reasonable ansatz for the shift in the dip angle is therefore

$$\Delta\lambda = \alpha(1+\beta\lambda)\cos^2\lambda \tag{4.10}$$

Since the dip distribution is peaked around $\lambda = 0$, the transformation of the z dependence may be seen as a polynomial expansion of $\tan\lambda$, in which quadratic and higher order terms are neglected, with the parameters α and β implicitly averaged over δ, w and dE/dx for many hits.

To allow for variations in the systematics for different parts of the chamber the CD is divided into 36 wedges each subtending 10° in Φ at the origin. A track is defined to lie in a given wedge if Φ_C, defined as the Φ angle of the chord joining the primary vertex and the track end-point, is within the limits of the wedge. With this definition, more hits on the track are contained within the wedge than if the standard Φ of the track is used.

The parameters α and β must be extracted from the experimental dip distributions. Since the effect is small, great care must be taken to ensure that the extracted parameters are not dependent on the method used to obtain them. Symmetrisation of the dip distribution must not change its underlying form. For example, an ansatz to order λ^2 could not be used since the width of the corrected dip distribution would not be unique. Three methods of obtaining of α and β have been studied:

- **Method 1: Fit to predicted dip distribution**

The expected dip distribution of tracks, $f(\Phi, \lambda)$ may be calculated analytically (see appendix B). Assuming that the charged particle p_t distribution is flat in pseudorapidity and azimuth:

$$f(\Phi, \lambda) = A\left(\frac{\cos\lambda}{1 - \cos^2\Phi\cos^2\lambda}\right) \tag{4.11}$$

Using equation 4.10 to define $\Delta\lambda$ a fit of the form $f(\Phi, \lambda = \lambda_{\text{meas}} - \Delta\lambda)$ was made to the data. The distribution for each Φ wedge is implicitly averaged over Φ so, in addition to α and β, Φ (in eq. 4.11) was allowed to vary slightly. The dip distributions must be corrected for the CD acceptance (see appendix A) for this method to make sense.

• **Method 2: Minimisation of mean and skewness**

This method aims to symmetrise the dip distributions irrespective of their functional form. Allowing the constants α and β to vary freely, $\lambda = \lambda_{\text{meas}} - \Delta\lambda$ was calculated for each λ_{meas} bin. The bins used were of width $1mrad$ to ensure sufficient accuracy in the measurement of α and β. The "corrected" mean μ_1, and coefficient of skewness, $\gamma_1 = \mu_3/\mu_2^{3/2}$ are evaluated, where the n^{th} moment, μ_n, of the dip distribution is defined as

$$\mu_n(\Phi) = \frac{\sum f(\Phi,\lambda)\lambda^n}{\sum f(\Phi,\lambda)} \tag{4.12}$$

where $f(\Phi, \lambda = \lambda_{\text{meas}} - \Delta\lambda)$ is the measured dip distribution and $\Delta\lambda$ comes from eq. 4.10. Final values for α and β are obtained by simultaneously minimising $|\mu_1|$ and $|\gamma_1|$.

• **Method 3: Symmetrisation χ^2**

This method is similar to the previous one but instead of the skewness an asymmetry parameter ε is used to measure the asymmetry:

$$\varepsilon^2 = \left(\frac{1}{N_{\text{bins}}}\right)\sum_{\text{bins}}\left(\frac{(f(\Phi,+\lambda) - f(\Phi,-\lambda))^2}{\sigma^2_{f(\Phi,+\lambda)} + \sigma^2_{f(\Phi,-\lambda)}}\right) \tag{4.13}$$

where again $f(\Phi, \lambda = \lambda_{\text{meas}} - \Delta\lambda)$ is the measured dip distribution, σ is the statistical error, and N_{bins} is the number of bins in the histogram. For a symmetrical distribution, $\varepsilon^2 \rightarrow 1$. To obtain α and β, the mean dip angle, $\langle\lambda\rangle$, is normalised to its statistical error, $\sigma_{\langle\lambda\rangle}$, and the function

$$\chi^2_{\text{symm}} = \frac{1}{2}\left(\frac{\langle\lambda\rangle^2}{\sigma^2_{\langle\lambda\rangle}} + \varepsilon^2\right) \tag{4.14}$$

is minimised. In principle, the ε^2 term is sufficient but the first term more explicitly requires the corrected distribution to be centered about $\lambda = 0$.

Method 1 is attractive since the fit is dominated by the high statistics region around $\lambda = 0$. The acceptance correction method does not, however, produce a flat ϕ distribution since the acceptance of particularly poor regions of the detector is necessarily set to zero and the other bins in ϕ (same p_t and η) are scaled to compensate (see appendix A). Thus, the predicted form given by eq. 4.11 is not strictly valid. The fit χ^2's were too large for this method to be used, although the values obtained for α were similar to those of the other two methods which gave consistent results for both α and β. Methods 2. and 3. do not require the data to be acceptance-corrected. In using the skewness, the second method is particularly sensitive to the high λ tails where the statistics are poor, so the third method was finally used.

The dip correction parameters α and β obtained using method 3. are presented in table 4.1. To apply this correction to a given track the dip angle is modified using eq. 4.10. From eq. 3.3, the corrected momentum is then given by

$$p_{corr} = p\frac{\cos\lambda_{\rm meas}}{\cos(\lambda_{\rm meas} - \Delta\lambda)} \tag{4.15}$$

The charged track p_t distributions, for $+\lambda$ and $-\lambda$ are presented in fig. 4.6, after application of the fiducial cut in Φ and the dip correction. Comparison with fig. 4.3 shows that that the data are greatly improved.

The ratios of the corrected p_t spectra, for $+\lambda$ and $-\lambda$, are shown in fig. 4.7 for (*a*) $\Phi_{\rm wrtb}$ <7·5°and (*b*) $\Phi_{\rm wrtb}$ >7·5°. Even after dip correction the fiducial cut in Φ is clearly necessary. For $\Phi_{\rm wrtb}$ >7·5°, the ratio is approximately flat for all p_t. Since the dip distribution is sharply peaked at λ=0, only a small systematic error in λ is needed for the dip angle of many tracks to change sign, resulting in $f^+(p_t)/f^-(p_t)$ <1·0. The measured value of p_t is, however, relatively insensitive to this residual error. An *upper* limit on the error in the measurement of p_t is estimated by making the extreme assumptions that the departure from the expected result $f^+(p_t)/f^-(p_t)$ =1·0 is due solely to the mis-measurement of p_t and that the sign of λ is always correct. The two curves were fitted with a power

Φ range	α	β
-180 → -170	-0.0237	0.66
-170 → -160	-0.0153	2.46
-160 → -150	-0.0124	8.08
-150 → -140	-0.0053	0.31
-140 → -130	-0.0081	2.41
-130 → -120	-0.0030	2.99
-120 → -110	-0.0061	0.16
-110 → -100	-0.0041	5.49
-100 → -90	-0.0127	7.16
-90 → -80	-0.0080	-0.43
-80 → -70	-0.0214	0.19
-70 → -60	-0.0135	8.91
-60 → -50	-0.0215	0.69
-50 → -40	-0.0130	7.61
-40 → -30	-0.0167	7.70
-30 → -20	-0.0100	-0.26
-20 → -10	-0.0154	9.50
-10 → 0	-0.0181	-0.25

Φ range	α	β
0 → 10	-0.0173	0.70
10 → 20	-0.0163	0.10
20 → 30	-0.0145	7.03
30 → 40	-0.0162	9.44
40 → 50	-0.0122	8.47
50 → 60	-0.0035	2.70
60 → 70	-0.0098	0.76
70 → 80	-0.0181	1.07
80 → 90	-0.0248	0.76
90 → 100	-0.0160	1.02
100 → 110	-0.0068	3.64
110 → 120	-0.0075	0.72
120 → 130	-0.0088	1.71
130 → 140	-0.0073	1.68
140 → 150	-0.0023	0.66
150 → 160	-0.0117	7.52
160 → 170	-0.0106	4.94
170 → 180	-0.0256	-0.10

Table 4.1: Dip correction constants

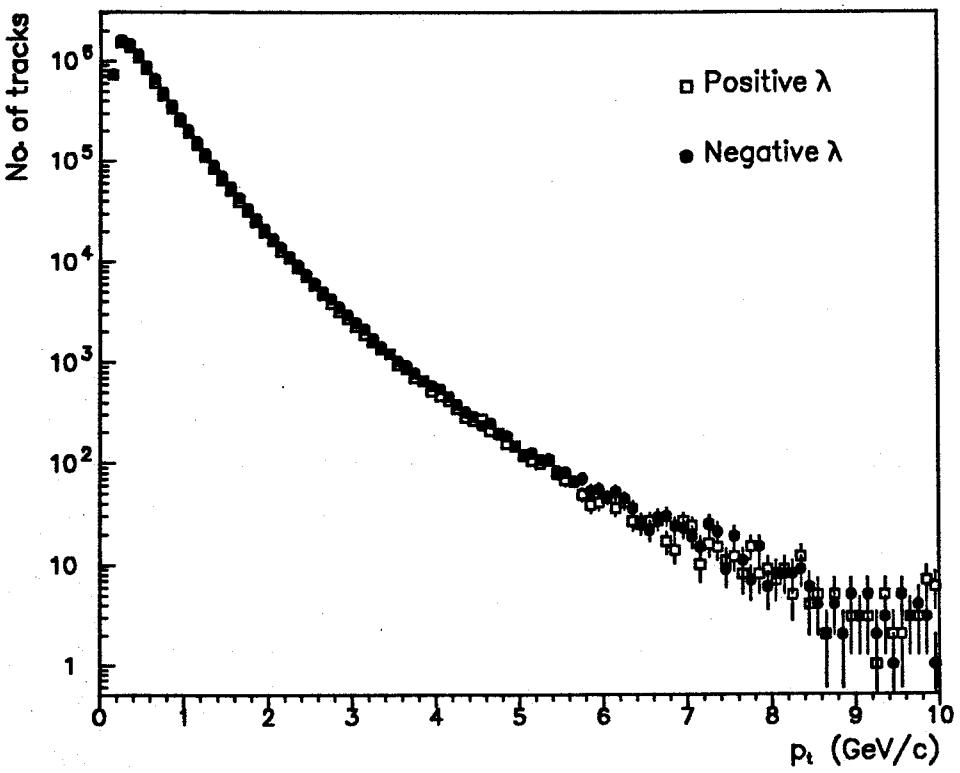

Figure 4.6: Charged track p_t spectra for $+\lambda$ and $-\lambda$ (corrected)

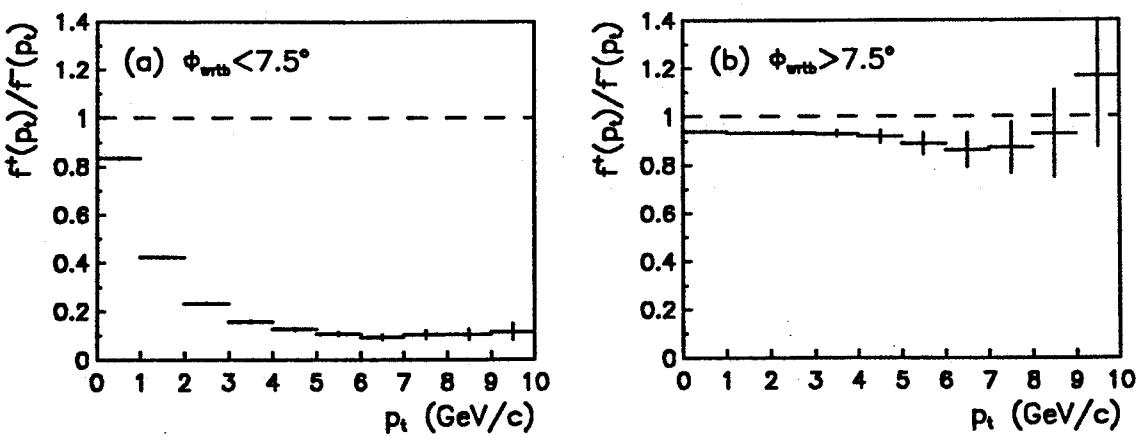

Figure 4.7: $f^+(p_t)/f^-(p_t)$ after dip correction. (a) $\Phi_{\rm wrtb}$ <7·5°and (b) $\Phi_{\rm wrtb}$ >7·5°

law (eq. 5.2 with p_0=1·42GeV/c). The p_t of the plot entries was scaled by a factor $(1+\delta)$ for $+\lambda$ and $(1-\delta)$ for $-\lambda$ and then the curves were re-fitted. By requiring $f^+(p_t)/f^-(p_t)$ to be unity for the fits, δ was estimated to be $\delta \approx 0{\cdot}005$. The systematic p_t error due to the z asymmetry, therefore, is estimated to be less than 0·5%.

4.5 Magnetic field correction

The measurement of track momenta in the CD uses a parametrisation of the magnetic field derived from detailed measurements at many points in x, y and z. Since the original survey, the separation of the magnetic yokes was increased slightly thereby reducing the magnetic field slightly. This effect is not taken into account by the standard track reconstruction program, resulting in a systematic overestimate of the track momenta. The field is predicted [38] to be globally lower than the nominal value by a factor:

$$f_B = 99.465\% \tag{4.16}$$

In this analysis, therefore, the momenta of all reconstructed tracks have been scaled by a factor f_B.

5. Charged Particle Production

5.1 Inclusive charged particle cross-section

The inclusive charged particle cross-section, $\sigma = 1/2((\sigma(p\bar{p} \rightarrow h^+X) + \sigma(p\bar{p} \rightarrow h^-X))$, has been measured for $|\eta| < 2{\cdot}5$ and $p_t > 0{\cdot}15\ GeV/c$. The dip angle and the momentum of all tracks have been corrected for the systematic error in the z coordinate using the procedure described in chap.4. The magnetic field correction factor, described in §4.5, was used to correct the momenta of all charged particles. The data have been corrected for the acceptance of the CD using the method described in appendix A. A correction has been made for the track-finding efficiency of 96% [34], which is approximately independent of p_t, η and ϕ. The contamination from strange particle decays, gamma conversions and secondary interactions in the beam-pipe and chamber walls has been studied using the Isajet Monte-Carlo [39] and the standard UA1 detector simulation program. These are found to increase the number of tracks associated to the primary vertex by 1·5%[40]. A global factor of 1/1·015 has therefore been applied to the measured cross-section. The ratio of the p_t distributions for positive and negative charged particles separately was checked and found to be consistent, within errors, with unity for the full range of p_t.

The invariant inclusive cross-section may be expressed:

$$E\frac{d^3\sigma}{dp^3} \approx \frac{1}{\Delta\phi\Delta\eta}\frac{d\sigma}{p_t dp_t} \tag{5.1}$$

where $\Delta\phi = 2\pi$ and $\Delta\eta$=5 in this analysis.

The distribution has been corrected for the smearing effect of the CD resolution

(see appendix D). The inclusive invariant cross-section for charged particle production within the pseudo-rapidity region, $|\eta|$ <2·5, is shown in fig. 5.1, together with previous UA1 results [41] for $\sqrt{s}$=200,500 and $900GeV$. The minimum-bias cross-sections used in the 1985 analysis were $40{\cdot}3mb$ and $44{\cdot}6mb$ at $\sqrt{s} = 500GeV$ and $\sqrt{s} = 900GeV$ which, assuming a logarithmic dependence on $\sqrt{s}$, gives $42{\cdot}0mb$ at $630GeV$. Following improved measurements of the total, elastic and single-diffractive cross-sections by UA4 and UA5 [24,25], the UA1 trigger was recalibrated [26,27]. The resulting minimum-bias cross-section for 1987 was (σ_{MB} = $37{\cdot}1\pm2{\cdot}6)mb$. For comparison with this analysis, the 1985 data have therefore been scaled by a factor 37·1/42·0=0·88. It is likely that a similar correction should be applied to the pre-1987 cross-sections of UA4 and UA5. The solid line is the result of a hybrid fit described in §5.2. The systematic error on the normalisation from the uncertainty in the minimum-bias trigger cross-section is, from eq. 2.4, 7·0%.

5.2 Charged multiplicity and mean p_t

In previous analyses [42,41,43], the invariant cross section was fitted with the semi-empirical function:

$$E\frac{d^3\sigma}{dp^3} = A\left(\frac{p_0}{p_t + p_0}\right)^n \tag{5.2}$$

A summary of the fit parameters from these analyses is shown in table 5.1, where the errors quoted are statistical only. The CDF collaboration requires a minimum p_t value of $0{\cdot}4GeV$ to ensure high and uniform reconstruction efficiency, since charged particles with p_t below $0{\cdot}33GeV/c$ spiral in the solenoidal field. The hardening of the p_t spectrum with increasing centre-of-mass energy is apparent in the decreasing power n.

To evaluate the mean charged track multiplicity, $\langle n_{ch}\rangle$, and the mean transverse momentum, $\langle p_t\rangle$, it is necessary to integrate the p_t spectrum. A correction must then be applied to correct for the p_t <$0{\cdot}15GeV/c$ cut by extrapolating the fit to

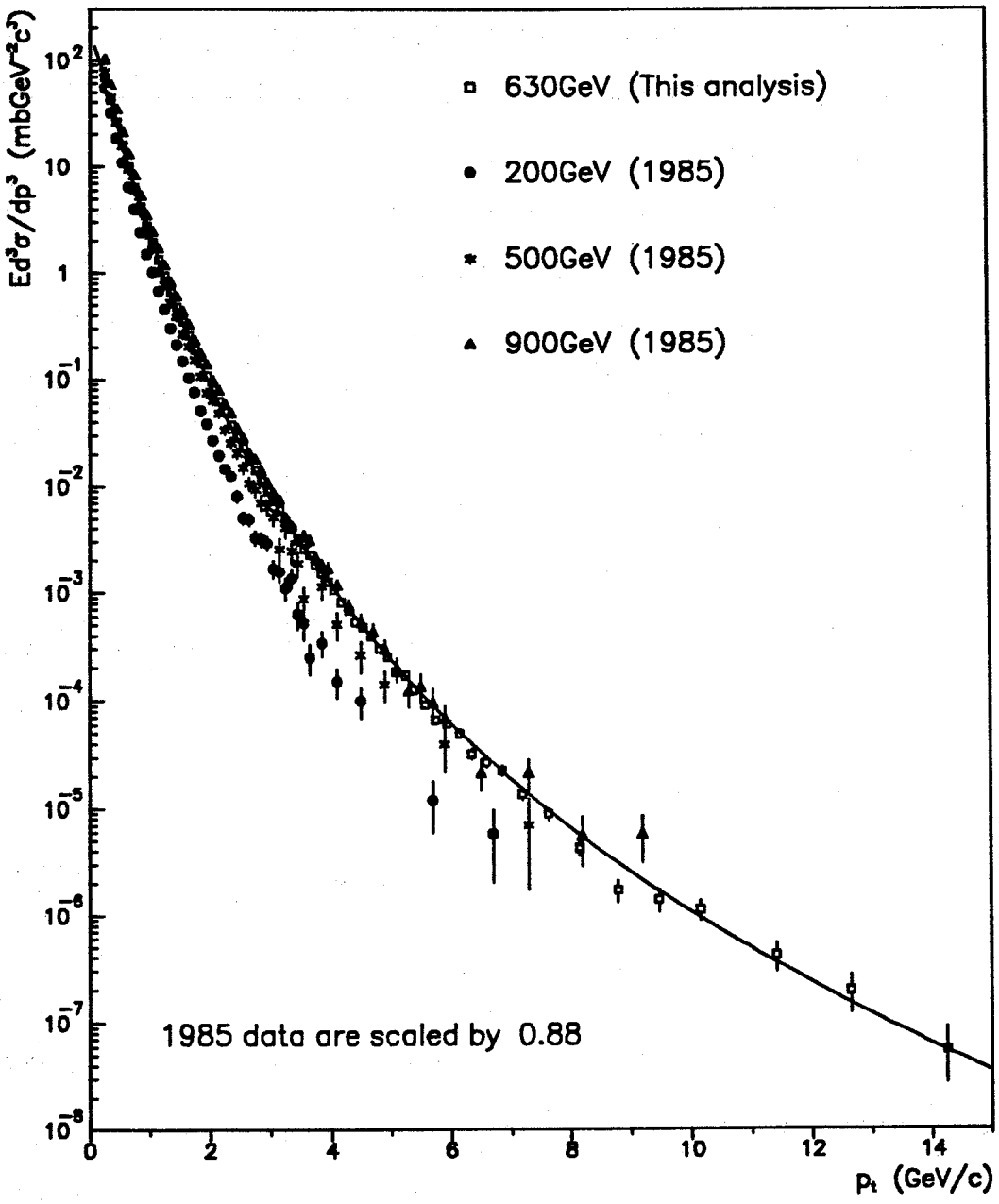

Figure 5.1: Inclusive charged particle invariant cross-section for $|\eta|$ <2·5 (the 1985 UA1 data is from ref. [41]).

	$\sqrt{s}$ (GeV)	Fit range (GeV/c)	A $(mbGeV^{-2}c^3)$	p_0 (GeV/c)	n
UA1 [42]	546	0.3 - 2.0	460 ± 10	1.30 fixed	9.14 ± 0.02
UA1 [41]	200	0.2 - 10.0	286 ± 17	1.80 ± 0.10	12.14 ± 0.39
	500	0.2 - 10.0	408 ± 24	1.61 ± 0.08	10.64 ± 0.31
	900	0.2 - 10.0	382 ± 20	1.56 ± 0.05	9.96 ± 0.17
CDF [43]	630	0.4 - 10.0	330 ± 10	1.30 fixed	8.89 ± 0.06
($\|\eta\| < 1.0$)		0.4 - 10.0	270 ± 10	1.63 ± 0.13	10.20 ± 0.56
	1800	0.4 - 10.0	450 ± 10	1.30 fixed	8.28 ± 0.02
		0.4 - 10.0	450 ± 10	1.29 ± 0.02	8.26 ± 0.08

Table 5.1: Previous fit results to the inclusive charged particle cross-section, of the form $Ed^3\sigma/dp^3 = Ap_0^n/(p_t + p_0)^n$

p_t=0. Since the p_t distribution is falling so rapidly, the calculation of $\langle n_{ch} \rangle$ and $\langle p_t \rangle$ is particularly sensitive to this extrapolation. In this analysis a hybrid expression [5] has been used to fit the invariant cross-section:

$$E\frac{d^3\sigma}{dp^3} = \begin{cases} Be^{-\beta m_t} & ; \text{ if } p_t < p_1 \\ A\left(\frac{p_0}{p_t+p_0}\right)^n & ; \text{ if } p_t \geq p_1 \end{cases} \tag{5.3}$$

where the transverse mass, m_t, is defined according to

$$m_t^2c^4 = m_\pi^2c^4 + p_t^2c^2 \tag{5.4}$$

The Boltzmann form of this expression at low p_t is predicted qualitatively by thermodynamics ($\beta \equiv (k_BT)^{-1}$, where k_B is the Boltzmann constant, may be used to define the temperature, T, of the interaction). The parameters B and β are constrained by A, p_0, n and p_1 (see eqs. C.4 and C.5 in appendix C) by requiring continuity of the cross-section and its first derivative at $p_t = p_1$.

Averaging over η and ϕ, the acceptance error is $\sigma(\mathcal{A}) \approx 0{\cdot}3\%$ for each of the five p_t bins used (see appendix A). At low p_t this error is larger than the statistical error. Therefore, to ensure that the fit was reliable, the data points falling within

each acceptance bin were allowed to vary by a common factor, $f_i = 1 \pm 3\sigma(\mathcal{A})_i$, with $i = 1, 5$. Non-uniqueness in the overall normalisation was avoided by constraining $f_3 \equiv 1.0$, this being the bin with the smallest acceptance error. The uncertainty in the normalisation, due to the error in the acceptance, is therefore given by $\sigma(\mathcal{A})_3 =$ 0·15%.

The solid line of fig. 5.1 shows the hybrid fit (using the full p_t range) to the inclusive charged particle cross-section. The fit parameters are given in table 5.2. The results for $p_1 \equiv 0.0$ are included to allow for comparison with the fit

Fit range (GeV/c)	A $(mbGeV^{-2}c^3)$	p_0 (GeV/c)	n	p_1 (GeV/c)
0.2 - 15.0	343.1 ± 2.9	1.42± 0.02	9.40 ± 0.08	0.44
0.2 - 15.0	330.1 ± 2.4	1.47± 0.02	9.54 ± 0.07	0.0 (fixed)

Table 5.2: Results of the fits to the inclusive charged particle cross-section.

parameters given in table 5.1. The mean multiplicity and transverse momentum are calculated from the fit parameters using the method described in appendix C. From eqs. C.10 and C.12, the hybrid fit yields

$$\langle n_{ch} \rangle = 17.2 \pm 0.4 \quad (|\eta| < 2.5) \tag{5.5}$$

$$\langle p_t \rangle = (0.477 \pm 0.005) GeV/c \tag{5.6}$$

The choice of the function used to extrapolate to $p_t = 0$ introduces a significant systematic error. Fig. 5.2 shows the fits for the power law (*i.e.* $p_1 \equiv 0$) and hybrid parametrisations at low p_t. No real distinction can be made between the power law and the hybrid fits on the basis of the fit χ^2 although the hybrid fit has more physical justification. Using the results of the pure power law fit, the values obtained are $\langle n_{ch} \rangle = 18.7 \pm 0.4$ and $\langle p_t \rangle = (0.449 \pm 0.005) GeV/c$, which are respectively 9% higher and 6% lower than for the hybrid fit due to the increased

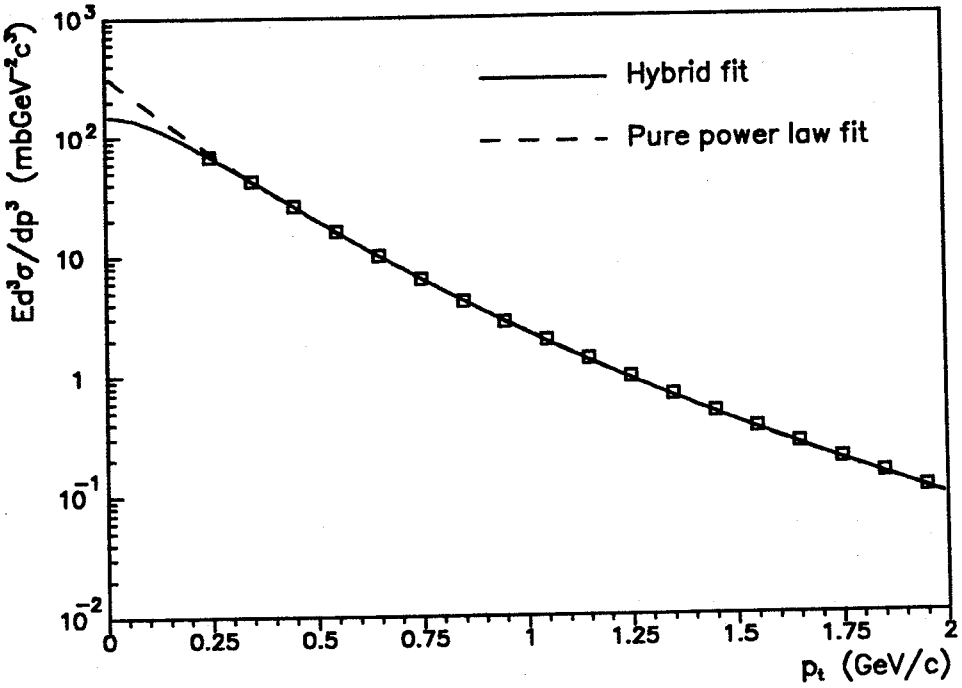

Figure 5.2: Hybrid and power-law extrapolations to p_t =0 of the inclusive charged particle cross-section.

bias from the low p_t region. The 7.0% error in the minimum-bias cross-section (eq. 2.4) does not affect the calculation of $\langle n_{ch} \rangle$ or $\langle p_t \rangle$.

The value of $\langle n_{ch} \rangle$ obtained in this analysis is seen to be in excellent agreement with previous analyses, shown in fig. 5.3 as a function of $\sqrt{s}$. The UA1 (1985), UA5 and NA22 data are taken from refs. [41,44,45,46]. Purely phase-space arguments predict a logarithmic growth of $\langle n_{ch} \rangle$ with $\sqrt{s}$ which seems to fit the data well. Measurements over the full rapidity range [47] indicate, however, that the increase is slightly faster with $\sqrt{s}$ (a term in $(\log s)^2$ is added) due to the onset of hard QCD processes. The evolution of $\langle p_t \rangle$ with $\sqrt{s}$ is shown in fig. 5.4 [41]. The increase in the hard scattering component is clearly indicated by the increase in the mean transverse momentum with increasing $\sqrt{s}$. The increases in $\langle n_{ch} \rangle$ and $\langle p_t \rangle$ with $\sqrt{s}$ are, as expected, highly correlated. Fig. 5.5 shows the invariant charged track cross-section for three ranges of the charged multiplicity, n_{ch}: 4–20, 20–40 and

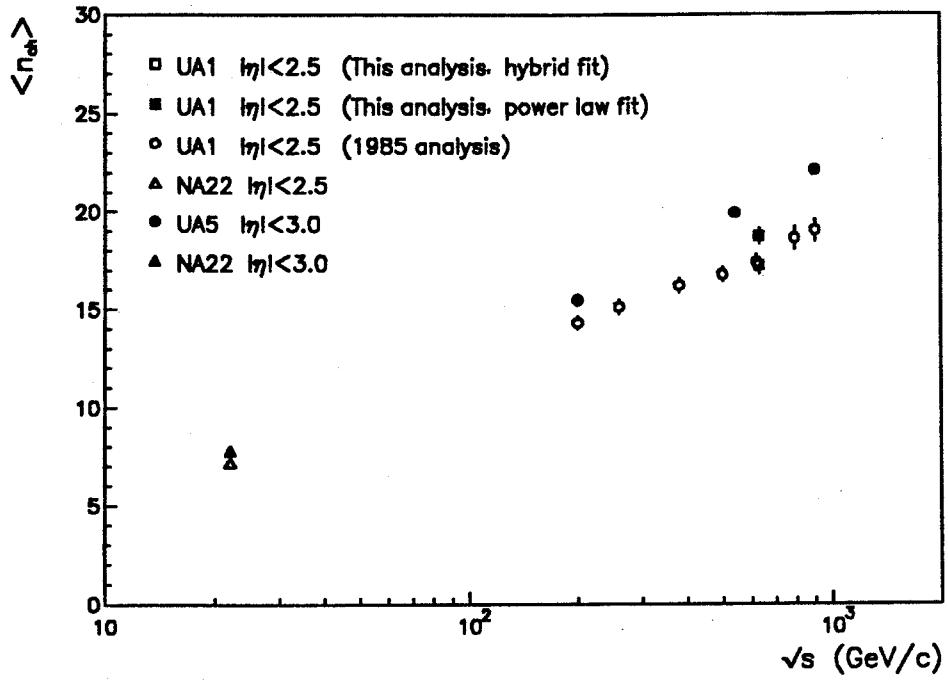

Figure 5.3: Variation of charged particle $\langle n_{ch} \rangle$ with $\sqrt{s}$ (the UA1, UA5 and NA22 data are taken from refs. [41,44,45,46]).

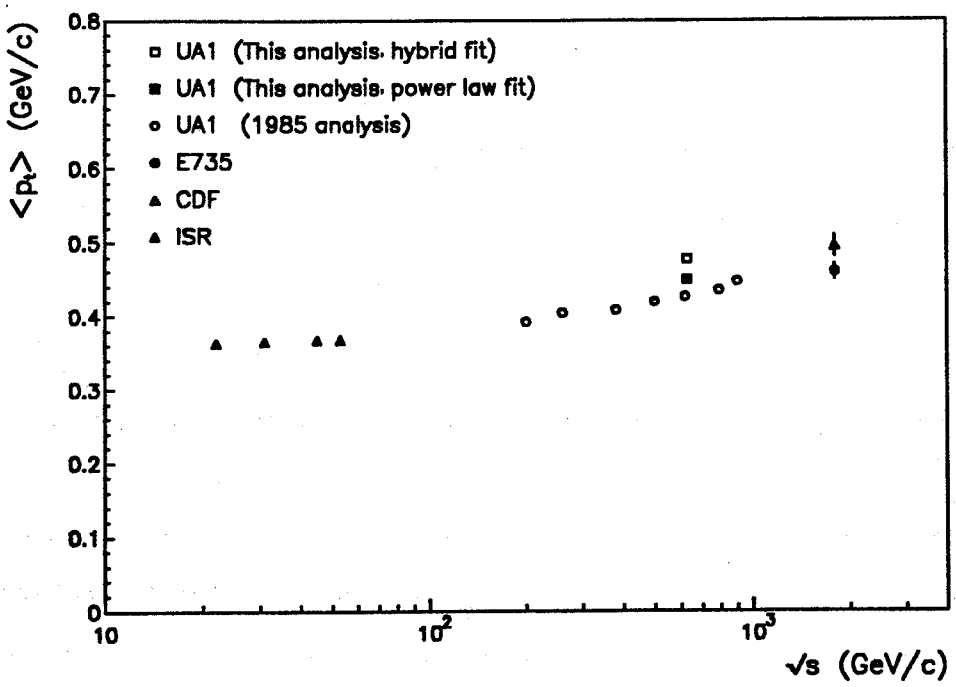

Figure 5.4: Variation of $\langle p_t \rangle$ for charged particles with $\sqrt{s}$ (ref. [41, and references therein]).

40–∞. To facilitate comparison of the relative shapes the two higher multiplicity

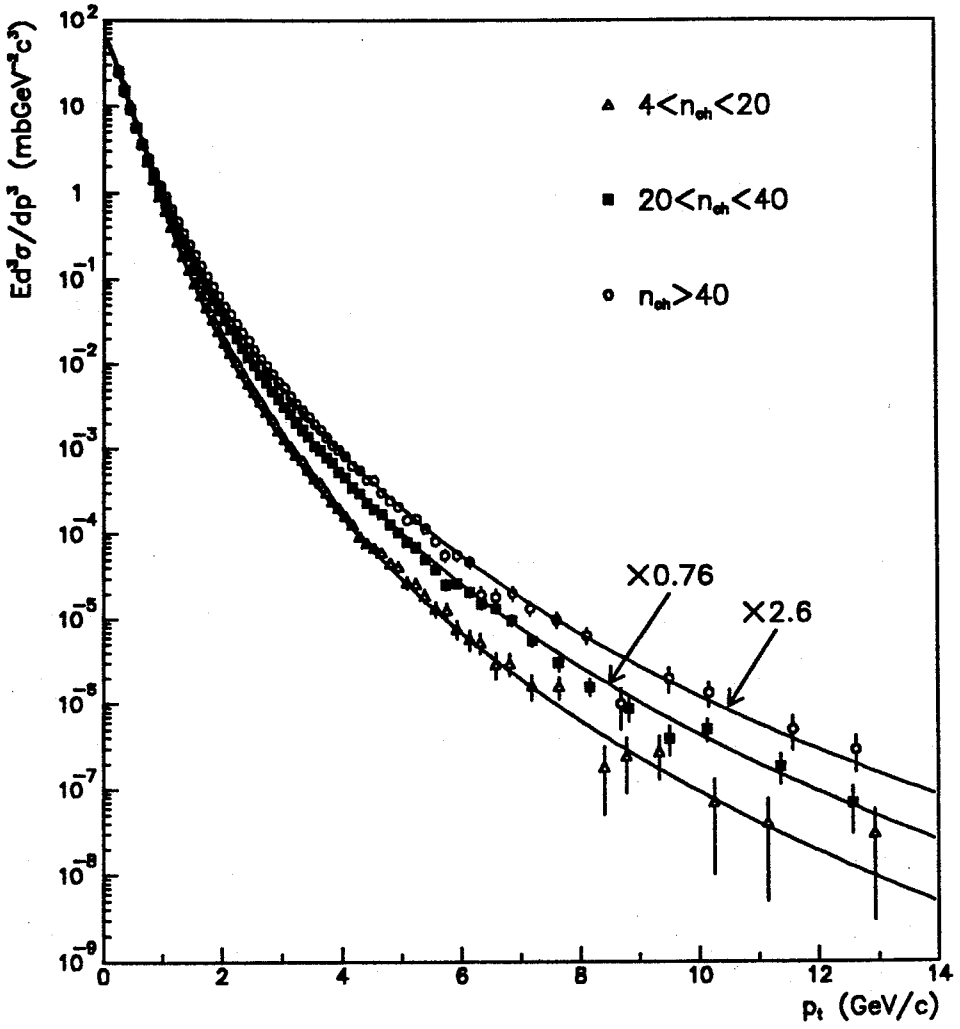

Figure 5.5: Invariant charged particle cross-section for different n_{ch} intervals.

curves have been normalised to the first data point of the lowest multiplicity curve. To extract the mean transverse momentum for the three curves, the data were fitted with the hybrid form of eq.5.3. The fit parameters are presented in table 5.3 and the resulting curves by the solid lines of fig. 5.5. The behaviour at low p_t is similar for each interval of n_{ch} but the high multiplicity events contain more high p_t particles, leading to a difference in $\langle p_t \rangle$ of $75 MeV/c$ between the low

and high multiplicity curves.

n_{ch}	A $(mbGeV^{-2}c^3)$	p_0 (GeV/c)	n	p_1 (GeV/c)	$\langle p_t \rangle$ (GeV/c)	κ
4–20	251±11	1.21±0.05	9.74±0.25	0.71	0.439±0.013	1.182
20–40	141±3	1.54±0.04	9.60±0.16	0.36	0.489±0.011	1.153
40–∞	36.0±1.0	1.51±0.06	8.95±0.22	0.17	0.514±0.019	1.136

Table 5.3: Fit results of $Ed^3\sigma/dp^3$ for different n_{ch} intervals.

The results presented so far have been corrected for the p_t cut of $0{\cdot}15 GeV/c$ by extrapolation of cross-section to $p_t = 0$. Fig. 5.5 clearly shows that the multiplicity dependence of this correction must be considered when evaluating the topological cross-section $d\sigma/dn_{ch}$. The final column of table 5.3 gives three values for the multiplicative factor, $\kappa(n_{ch})$, required to correct n_{ch} for the p_t cut. The values for κ are constant within 4% for the full range of n_{ch}, so n_{ch} is corrected assuming a linear dependence of κ on n_{ch}. The corrected inclusive charged track multiplicity, for the pseudorapidity region $|\eta|$ <2·5, is presented in fig.5.6.

As discussed above, the 1985 data have been scaled by a factor of 0·88 to correct for the different minimum-bias cross-section used in the 1985 analysis. The good agreement of the curves for low multiplicity events reflects the slow variation with $\sqrt{s}$ of the soft-hadronic part of the total cross-section. The increase with $\sqrt{s}$ in the number of high multiplicity events is due to the hard QCD component.

The KNO-scaling hypothesis [48] predicts that the normalised multiplicity distribution, $(\langle n \rangle/\sigma_{\rm MB})d\sigma_{\rm n}/dn_{\rm ch}$, behaves as a universal function of the variable, $z = n/\langle n_{\rm ch} \rangle$, in the asymptotic limit ($\sqrt{s} \rightarrow \infty$). That is, that the shape of the KNO distribution is independent of $\sqrt{s}$. The UA5 collaboration has observed KNO scaling violations in non-single diffractive events (all η) due mainly to very high multiplicity events ($z > 4$) [49]. The KNO multiplicity distributions are pre-

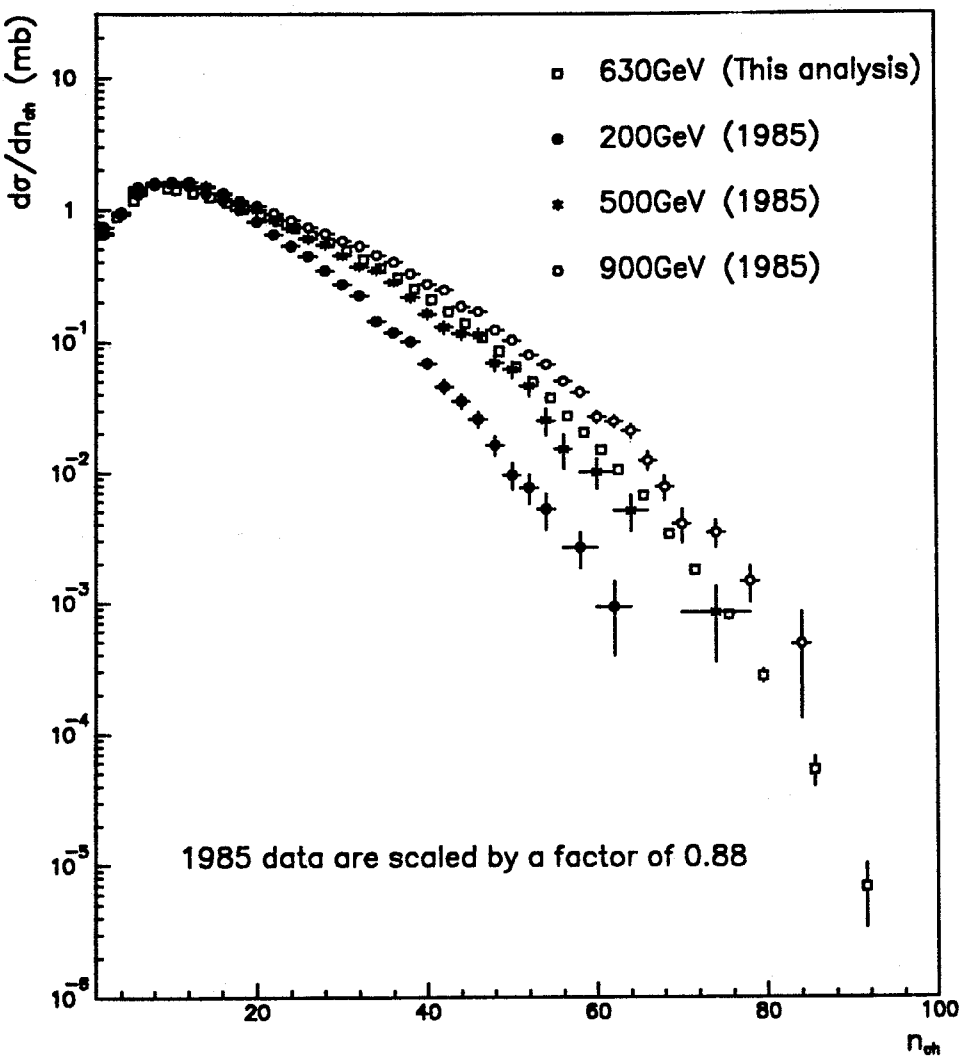

Figure 5.6: Topological cross-section, $d\sigma/dn_{ch}$, for $|\eta| < 2{\cdot}5$ (1985 UA1 data are from ref. [41]).

sented in fig. 5.7 in terms of the KNO-scaling variables. The data are consistent

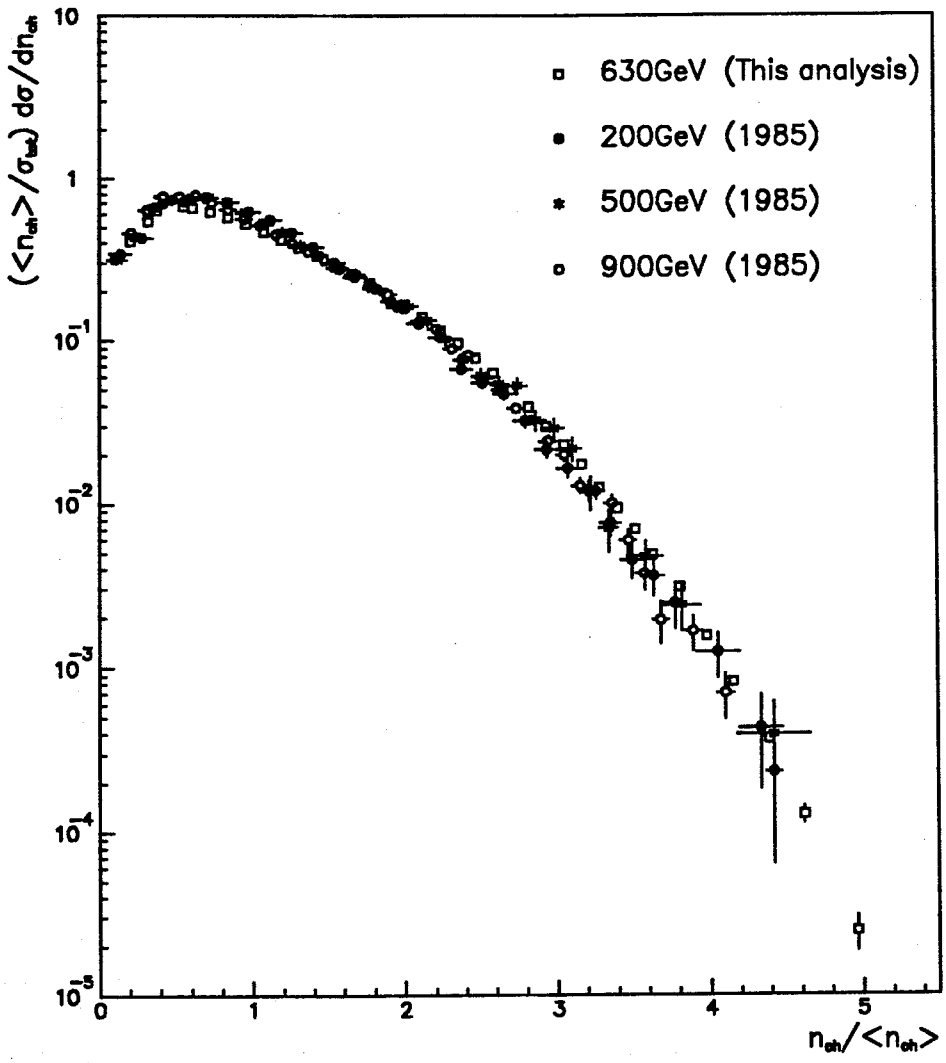

Figure 5.7: KNO multiplicity distributions $|\eta| < 2{\cdot}5$ (1985 UA1 data are from ref. [41]).

with a unique distribution.

The detailed variation of the mean transverse momentum with charged track multiplicity has been measured. A multiplicity-dependent correction factor for the p_t cut has been applied to the mean transverse momentum in a similar way to the κ correction of n_{ch}. The variation of $\langle p_t \rangle$ with n_{ch} is shown in fig. 5.8. For low multiplicities the mean p_t is particularly sensitive to whether a power

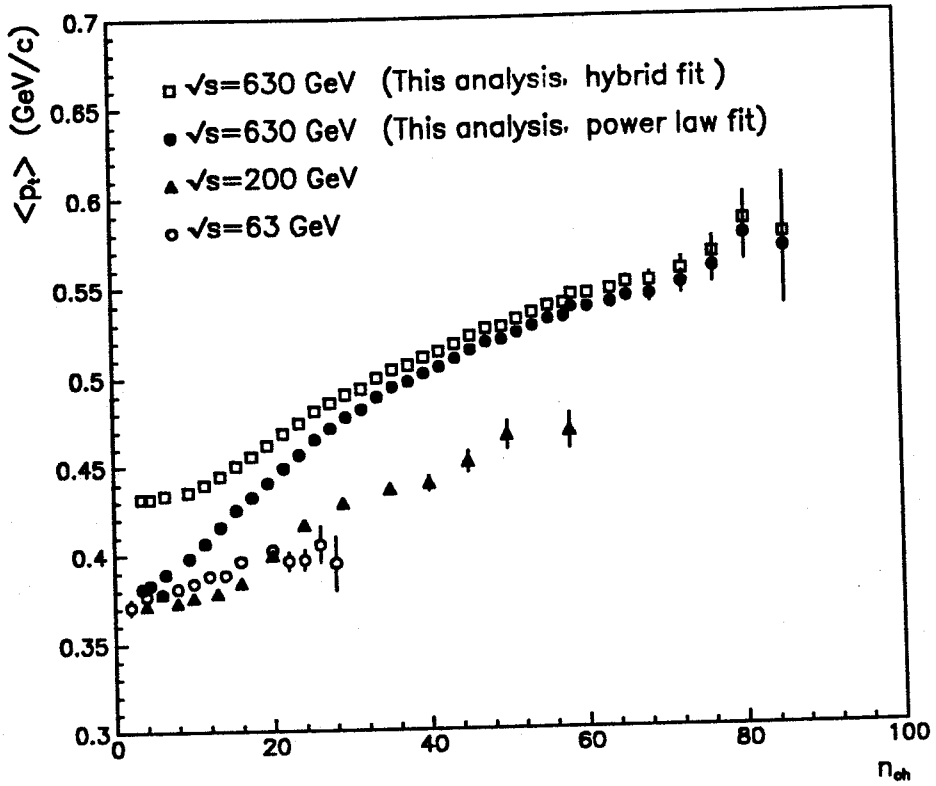

Figure 5.8: Mean p_t as a function of the charged particle multiplicity (the lower energy data are from ref. [41]).

law or a hybrid form is used in the extrapolation to $p_t = 0$ so corrected curves for both assumptions are shown. Lower energy $p\bar{p}$ data [41] at $\sqrt{s} = 63GeV$ and $\sqrt{s} = 200GeV$ are shown for comparison. For low multiplicity events the mean p_t is almost independent of $\sqrt{s}$. The strong correlation between $\langle p_t \rangle$ and n_{ch} may be a result of the increased gluon radiation in high q^2 interactions. At large multiplicities, the mean p_t reaches a value comparable with the mean p_t measured in events containing jets with large transverse energy [50].

6. V^0 reconstruction

A V^0 may be defined as any electrically neutral particle which decays into two charged particles with a V-like topology. Two tracks are seen in the drift chamber originating from the same point in space. There is no incoming track since the neutral parent causes no ionisation in the gas. By searching for track pairs with this characteristic shape, the following decays:

$$K_S^0 \rightarrow \pi^+\pi^- \tag{6.1}$$

$$\Lambda^0 \rightarrow p\pi^- \tag{6.2}$$

$$\bar{\Lambda}^0 \rightarrow \bar{p}\pi^+ \tag{6.3}$$

may be reconstructed. Neutral pions are abundantly produced which decay to gamma pairs with B =98·8%. In the electric field of a nucleus, for example in the beam-pipe or the chamber walls, these may subsequently convert to e^+e^- pairs [51], which are also reconstructed as V^0's.

The decay: $K_L^0 \rightarrow \pi^+\pi^-\pi^0$ has a branching fraction of 12·4% and a mean decay length of $c\tau$ =15·54m. A small fraction of these decays occur within the chamber, and since the π^0 is not observed they have a V^0 topology. The reconstructed V^0 momentum vector does not, however, account for the unseen π^0 so the V^0 will not be associated to the primary vertex.

6.1 V^0 finding

The standard UA1 event processing software includes routines for the identification of K_S^0, Λ^0 and $\bar{\Lambda}^0$ decays and γ-conversions [52,53,54]. The output from the

V^0	Mass (MeV)	Lifetime (sec)	Decay length (cm)
γ	—	—	—
K^0_S	$497 \cdot 67$	$(0.8922 \pm 0.0020) \times 10^{-10}$	2.675
$\Lambda^0/\bar{\Lambda}^0$	$1115 \cdot 63$	$(2.631 \pm 0.020) \times 10^{-10}$	7.89

Table 6.1: Properties of V^0 particles

production includes V^0 data banks with very loose selection criteria eliminating the need for repetitive and time-consuming computation each time V^0 studies are made on a particular data-set.

All pairs of positive and a negative tracks are considered as the possible products of a V^0 decay, provided the tracks pass the basic track quality cuts (table A.1). To ensure that the momentum is well measured, the track must also satisfy $\sigma_p/p < 20\%$. Each of the decay tracks is required to have $p > 100MeV/c$, since very low momentum tracks suffer from multiple scattering. Those V^0 candidates with $p_t < 200MeV/c$ or rapidity y >3·0 are rejected. Unlike the combinatorial background, the tracks of the V^0 decay products do not, in general, point back to the primary vertex. A track association χ^2 is defined:

$$\chi^2_{i,ass} = (b_i/\sigma_{b_i})^2 \tag{6.4}$$

where b_i is the impact parameter of track i (fig. 6.1) with an error σ_{b_i}. Cutting at $2\sigma_{b_i}$, by requiring $\chi^2_{i,ass} > 4.0$ for both decay tracks, greatly reduces the background of random pairs from the primary vertex which fake a V^0 decay. The association of the V^0 to the primary vertex is required by rejecting those candidates with $b(V^0) > 3mm$. This cut reduces the efficiency for V^0's coming from secondary decays, for example $\Xi^- \rightarrow \Lambda\pi^-$ with a branching fraction $B \simeq 100\%$ and a decay length of $c\tau$=4·91cm. In addition, candidates with $b(V^0)/\sigma_{b(V^0)}$>3·0 are rejected.

The two tracks must cross within a tolerance of $3mm$ in the xy-plane and $30cm$ in z — the latter being a very weak requirement. Depending on where the wire

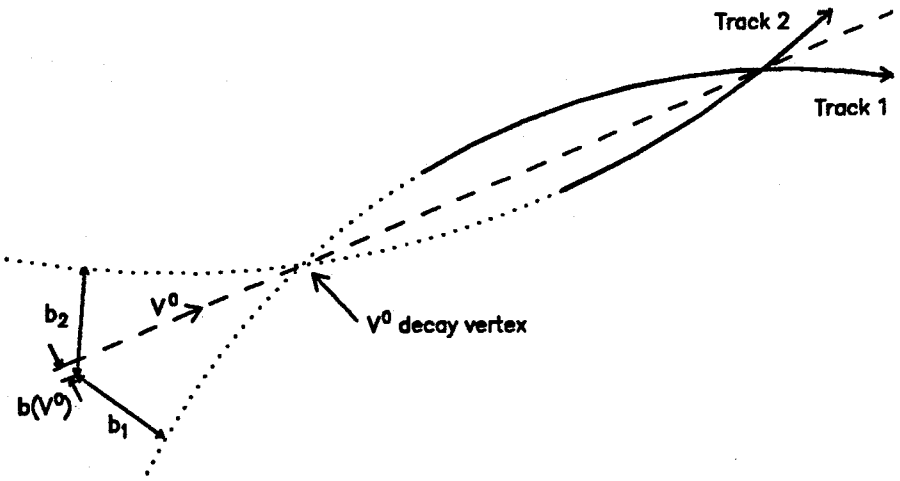

Figure 6.1: V^0 decay topology

hits start there are either one or two possible V^0 vertices. Candidates are rejected if the decay distance of the V^0 is negative, or if the digitisings start before the first crossing point from the vertex, thereby violating causality. There is a tolerance on the latter condition of $10mm$, corresponding to the separation of adjacent sense wires. The two tracks are then fitted in the sz-plane constraining each track to start at the same point. If there are still two possible crossing-points then that with the smaller χ^2_z is selected.

The invariant mass, M, in a 2-body decay may be written

$$M = \sqrt{(p_1^2 + m_1^2) + (p_2^2 + m_2^2) + 2\sqrt{p_1^2 + m_1^2}\sqrt{p_2^2 + m_2^2} - P^2} \qquad (6.5)$$

where M, P and p_i, m_i $(i = 1, 2)$ are the masses and momenta of the initial and final state particles. The invariant mass spectra of the V^0, evaluated assuming each of the hypotheses (eqs.6.1–6.3) in turn, are presented in fig. 6.2. Broad mass windows (table 6.2) were defined for each hypothesis and the V^0 candidate was rejected if, for no hypothesis, did it fall within the appropriate mass window. The mass cut reduces the size of the sample with negligible loss of K^0_S's ($< 0.1\%$). At this stage, it is possible for candidates to satisfy more than one mass hypothesis.

For the 1987 data sample, no cuts were made on the V^0 decay length nor on

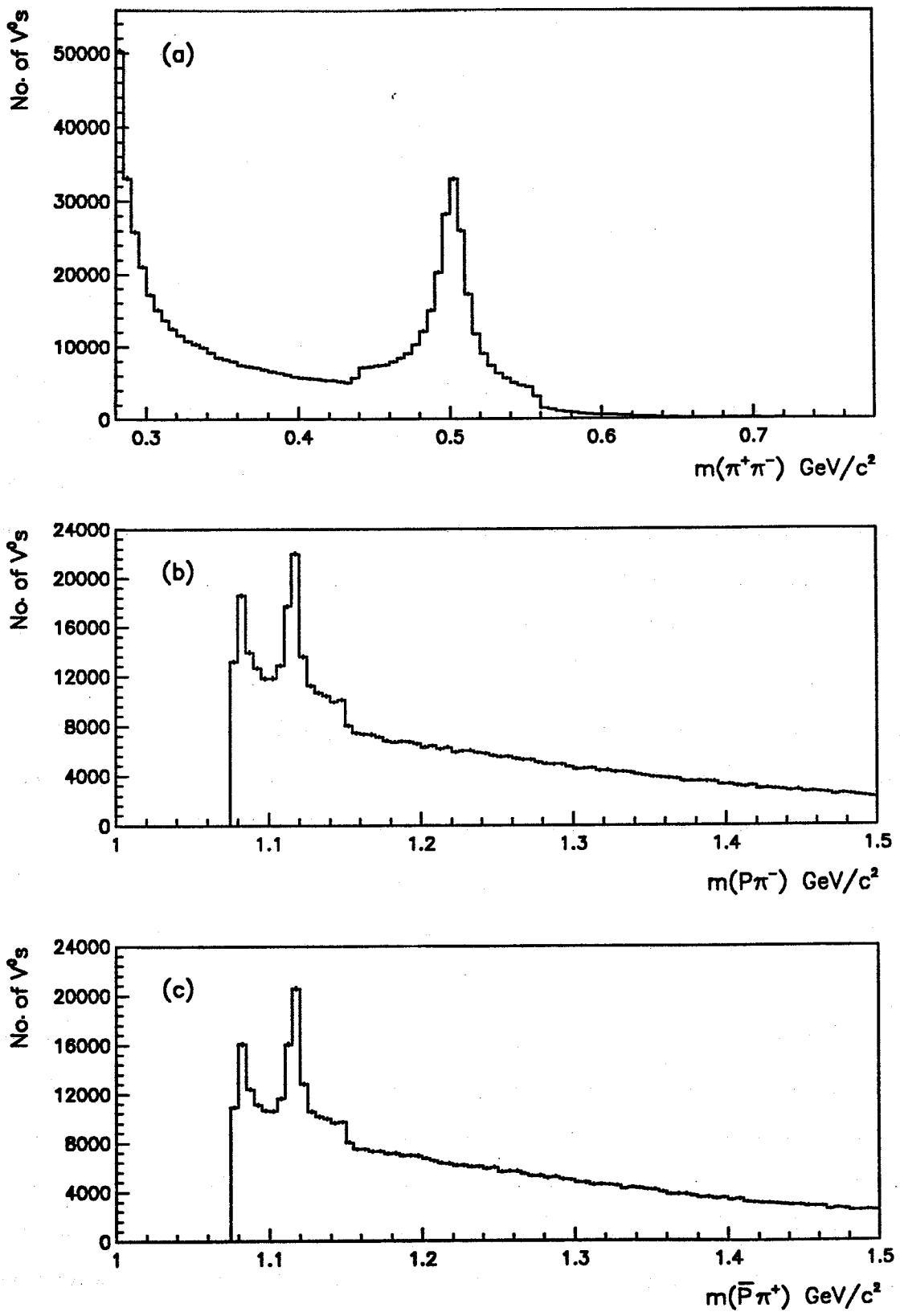

Figure 6.2: V^0 mass spectra (production cuts): (a) K^0_S, (b) Λ, and (c) $\bar{\Lambda}$

V^0	Production Mass Window (MeV)	Tight mass window (MeV)
γ	0 - 70	—
K^0_S	438 - 558	477.7 - 517.7
$\Lambda^0/\ \bar{\Lambda}^0$	1081 - 1151	1110.6 - 1120.6

Table 6.2: Mass Windows V^0 selection

the p_t of the decay products relative to the V^0.

For all track pairs surviving these cuts, a V^0 data structure was created to store basic information on the candidate, including reference links to the data banks describing the daughter tracks, the decay vertex, and their associated errors. From these the kinematic variables of the V^0 may easily be calculated, so such information was not stored. Track-sharing may occur at this stage where the same track is used by more than one V^0 candidate.

The cuts described so far are referred to as the "production cuts". From fig 6.2 it can be seen that there is still a large background in the V^0 samples. In particular, the K^0_S is contaminated by γ-conversions, the random selection of track pairs with a similar topology to the decay products of the K^0_S, and the $\Lambda/\bar{\Lambda}$ reflection.

To help understand the characteristics of these backgrounds, a sample of 5000 minimum-bias events was generated using the Isajet Monte-Carlo [39], passed through the detector simulation and fully reconstructed. Neutral pions were permitted to decay to two photons which could then convert to an e^+e^- pair in the beam-pipe, CD walls and the chamber gas. The production of K^0_S and $\Lambda/\bar{\Lambda}$ was simulated and these decayed to hadrons according to the appropriate lifetimes and branching fractions. Furthermore, their secondary production through hadronic interactions in the detector material was simulated. These events were analysed in the same way as the real data with the advantage that the generated and reconstructed events could be compared. In particular the particle identities of the reconstructed tracks were considered known if the majority of the points used

corresponded to the simulated digitisings of a single Monte-Carlo track.

Figure 6.3 shows the mass spectrum, for the $K^0_S \rightarrow \pi^+\pi^-$ hypothesis, of all reconstructed V^0 decays. The dominant source of background is from γ-conversions, shown by the hatched region. The remaining background is from track combinatorials with an almost negligible contamination from Λ decays. In the following

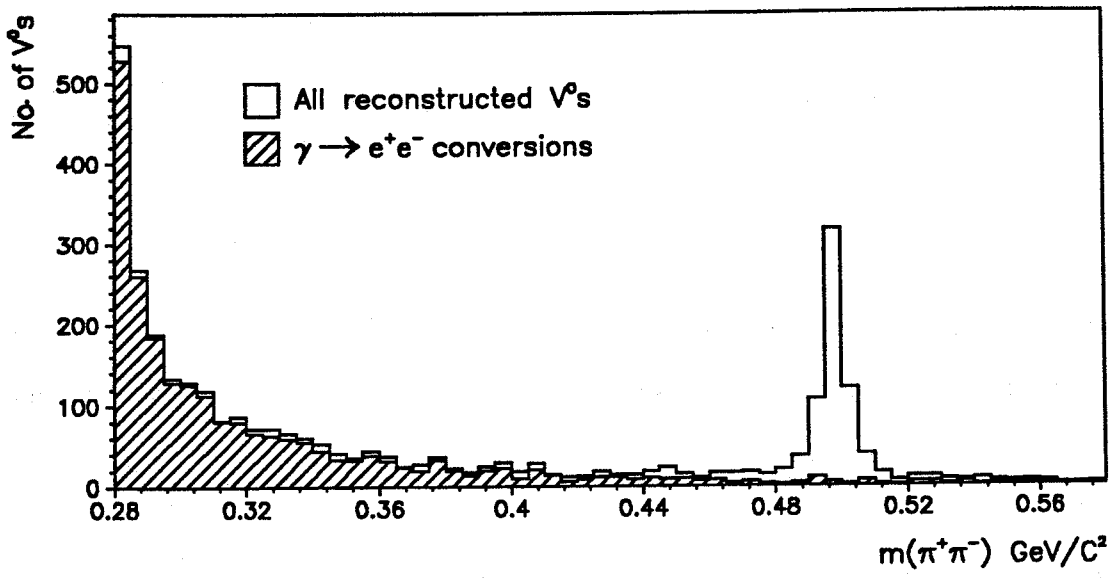

Figure 6.3: Simulation of $\gamma \rightarrow e^+e^-$ background to K^0_S signal

sections the *real data* is considered, and additional cuts for reducing the K^0_S background in the K^0_S sample are described; the Monte-Carlo data are used to predict some of the topological features of the background processes.

6.2 Decay time probability

Fig. 6.4 shows the V^0 decay length distribution (a) in the xy and (b) in the yz plane, for the production cuts only. In fig. 6.4(a) a peak is seen due to photon conversions in the CD chamber wall at $x \simeq \pm 1m$. Similarly, in fig. 6.4(b) a peak at $r \simeq 10cm$, corresponding to the beam-pipe and the CD inner wall, is apparent. In the xy-plane fiducial cuts could be applied to remove some V^0s with vertices in material boundaries but for most of the detector this is not practical due to

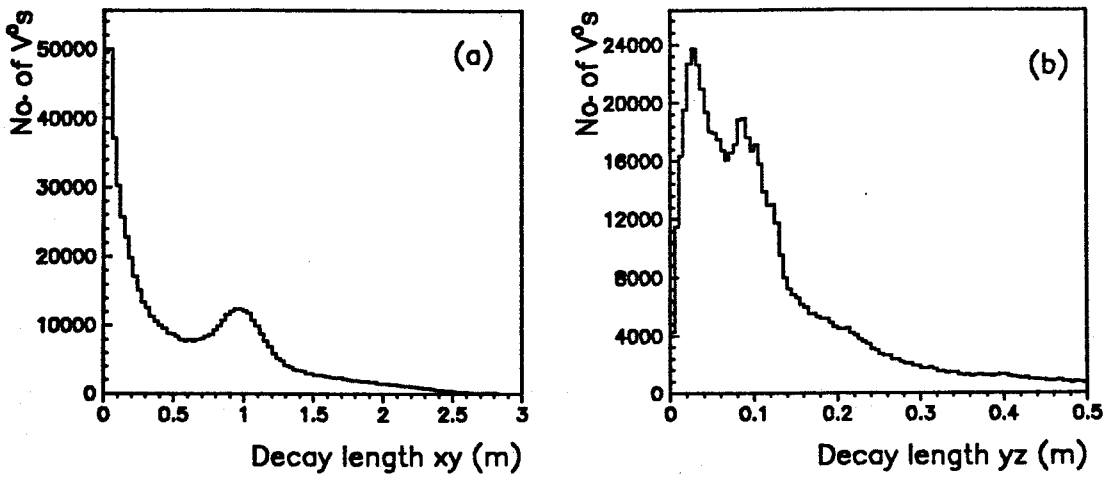

Figure 6.4: V^0 decay length in (a) the xy plane and (b) the yz plane.

the poorer resolution of the CD in the z coordinate. Cutting the decay length is also undesirable since this removes high transverse momentum V^0s decaying some distance from the vertex.

Since the K^0_S lifetime distribution is decreasing exponentially with time, the probability P_d that a particular K^0_S of momentum, p, decays within a decay length d is given by

$$P_d = 1 - e^{-d/c\tau\beta\gamma} \tag{6.6}$$

where $c\tau = 2.675cm$ for K^0_S, and $\beta\gamma = p/m_{K^0}$ is the time dilation factor. Equal bins of P_d should contain the same number of V^0s, so the dn/dP_d distribution should be flat in P_d.

The experimental decay probability distribution is shown in fig. 6.5(a). The drop in the distribution at low values of P_d is due to the loss of efficiency for short decay lengths when the decay products tend to be associated to the primary vertex. For example, for a K^0_S with $p = 500MeV/c$, the region P_d <0·2 corresponds to a decay length of less than $6mm$. The spikes at $P_d \approx 1$ correspond to V^0 candidates which are anomalously long compared to the K^0_S lifetime. Fig. 6.5 also shows (inset) the Monte-Carlo decay lifetime probability distributions for (b) gamma conversions, and (c) the combinatorial background, assuming the K^0_S hypothesis;

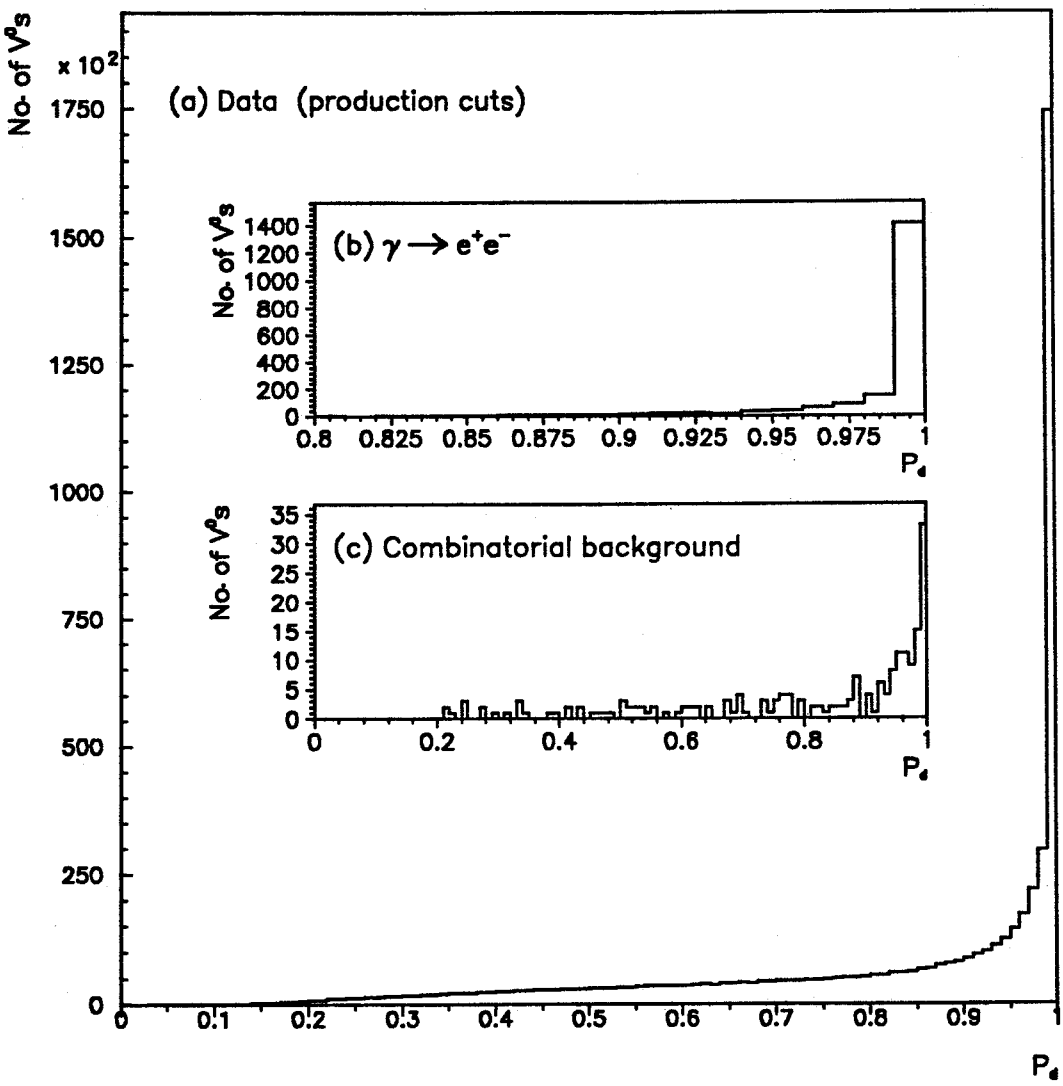

Figure 6.5: Decay probability, P_d: (a) Data (production cuts), and Monte-Carlo, (b) $\gamma \rightarrow e^+e^-$ and (c) combinatorial background.

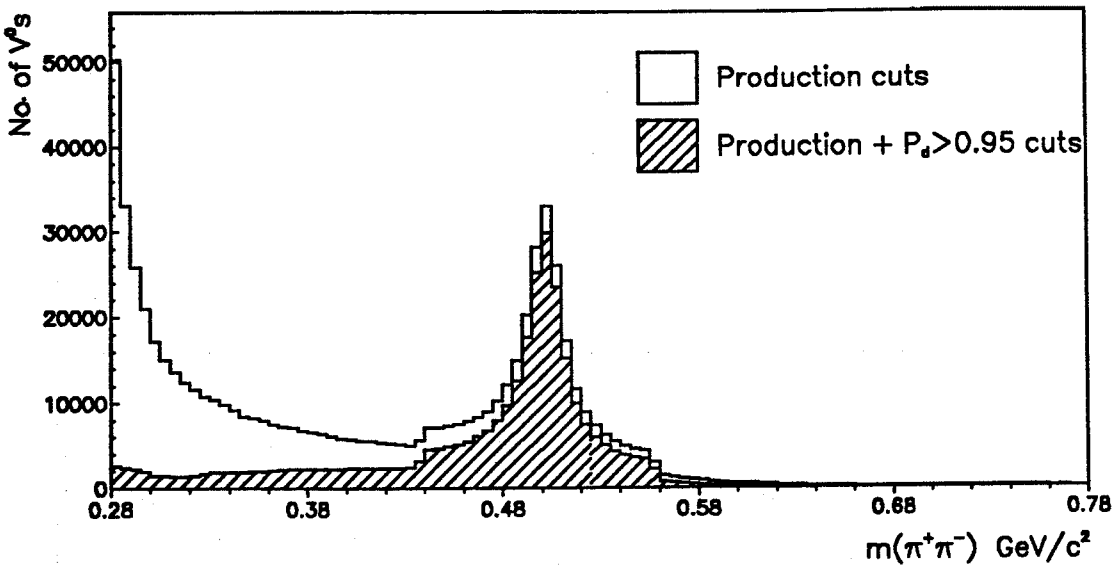

Figure 6.6: Mass for K^0_S hypothesis showing the effect of the P_d >0.95 cut.

note the different horizontal scales. The Monte-Carlo gamma data is strongly peaked at $P_d \simeq 1$, which is expected for low momentum photons converting some distance from the primary vertex. There may also be a small contribution to the combinatorial background from the secondary interactions of hadrons in the beam-pipe and the chamber walls.

Fig. 6.6 shows the effect on the K^0_S mass spectrum of applying a cut of P_d >0·95 in addition to the production cuts. The hatched region corresponds to those candidates surviving the P_d cut. There is no p_t bias with this cut; the K^0_S reconstruction efficiency (chap. 7) decreased by a factor of only 0·97±0·07 at $p_t = 5GeV/c$. Thus, all V^0 candidates with a decay lifetime probability of P_d >0·95 were rejected.

6.3 Cos$\theta^\star$

From Monte-Carlo it was found that 97% of gamma conversions have an opening angle in the projected plane of less than 2°, suggesting this as a powerful cut to reduce the K^0_S background. High transverse momentum K^0_S's, however, also tend to have small opening angles so such a cut is hardest on that part of the sample with lowest statistics. By considering the angular distribution of the decay in the

rest-frame of the V^0 a less biased and equally effective cut is possible.

In the V^0 rest-frame, θ^* is defined to be the angle between the positive decay track and the V^0 line of flight. Since the K^0_S has zero spin it decays isotropically in its rest-frame. A uniform decay distribution in solid angle, $d\Omega^* = \sin\theta^* d\theta^*$, corresponds a flat differential distribution in $\cos\theta^*$. The experimental $\cos\theta^*$ distribution for the K^0_S hypothesis is shown in fig. 6.7(a). For gamma conversions,

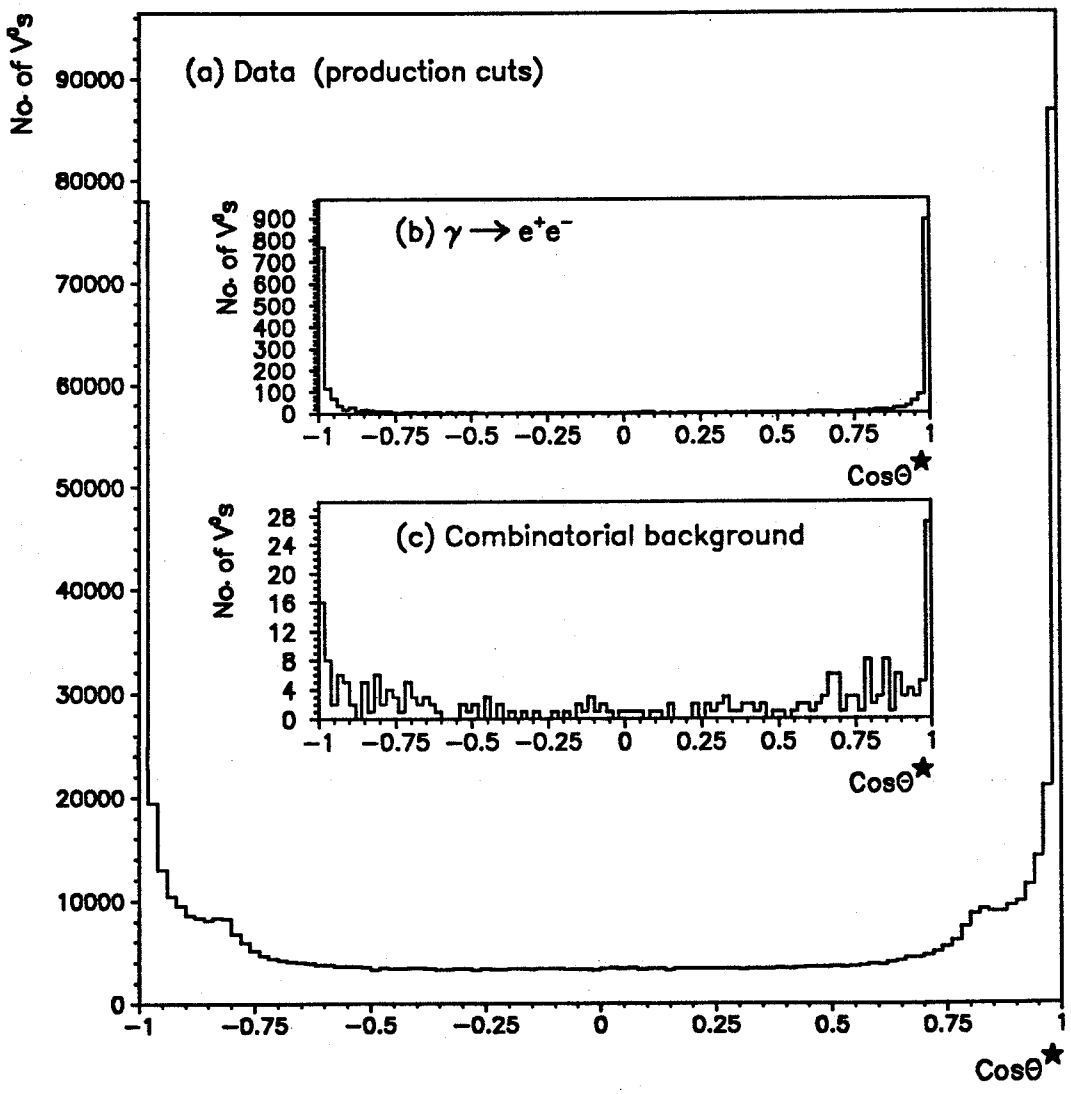

Figure 6.7: K^0_S hypothesis: $\cos\theta^*$ for (a) data (production cuts) and Monte-Carlo, (b) $\gamma \rightarrow e^+e^-$ and (c) combinatorial background.

the incorrect Lorentz boost of the two electrons under the K^0_S decay hypothesis, results in sharp peaks at $\cos\theta^* \simeq \pm 1$, as shown in fig. 6.7(b) for the Monte-Carlo

sample. Fig. 6.7(c) shows the $\cos\theta^*$ distribution for the random background. This is also biased towards $|\cos\theta^*| \simeq 1$, with the untagged K^0_S's populating the whole spectrum.

The mass spectrum under the K^0_S hypothesis with the production cuts is shown in figure 6.8. The hatched region shows the effect of adding a cut of $|\cos\theta^*| > 0{\cdot}75$. From single K^0_S Monte-Carlo studies (chap. 7) this reduction factor was found to

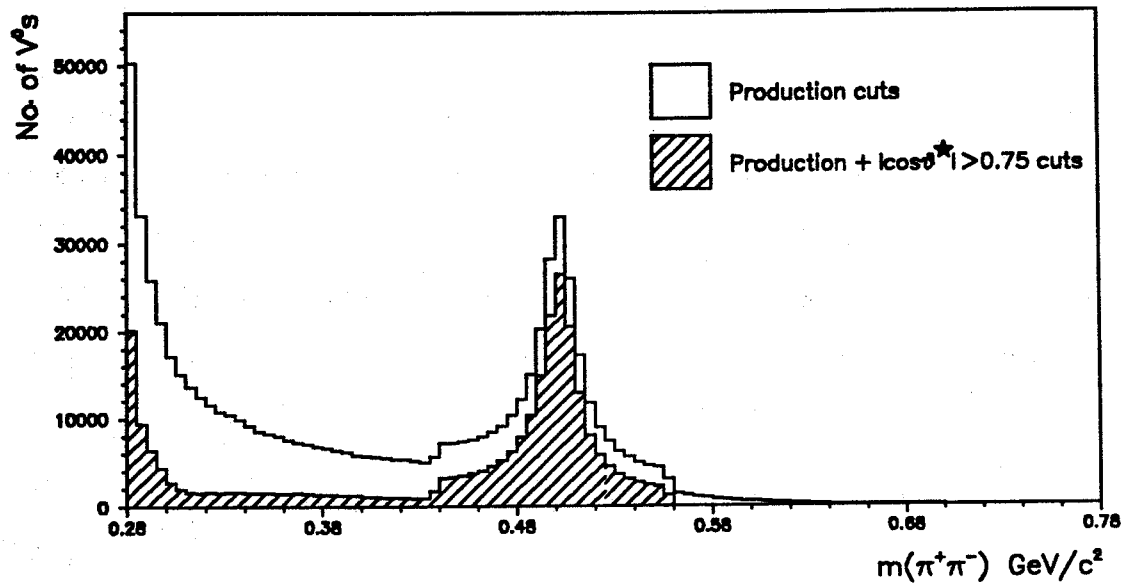

Figure 6.8: Mass for K^0_S hypothesis showing the effect of the $\cos\theta^* > 0.75$ cut.

be independent of p_t, as expected. Thus, a cut was made in $\cos\theta^*$, under the K^0_S hypothesis, if $|\cos\theta^*| > 0{\cdot}75$.

6.4 Fiducial Φ and decay plane orientation cuts

Prior to analysis, the dip-angle correction described in §4.4 was applied to all the tracks in the event, including the V^0 decay tracks. As discussed in §4.3, the wires close to the beam are particularly affected by noise. In line with the charged particle analysis, a fiducial cut was made whereby all V^0's having either decay track within 7·5°, in the projected plane, of the x-axis were removed from the sample.

The poor resolution in the charge-division coordinate adversely affects the V^0 reconstruction, especially in the horizontal plane. The track-fitting of the event requires that the tracks of the V^0 be coplanar, within errors, with the primary event vertex. A unit vector normal to this decay plane is then defined:

$$\vec{n} = (n_1, n_2, n_3) = \frac{\vec{p}_{pos} \times \vec{p}_{neg}}{|\vec{p}_{pos}||\vec{p}_{neg}|} \tag{6.7}$$

where the components, n_i, are the direction cosines of the normal vector, and $\vec{p}_{pos}$ and $\vec{p}_{neg}$ are the momentum vectors of the decay products. For $n_3 \simeq \pm 1$ the decay plane of the V^0 coincides with the bending plane so the tracks are well measured. For small values of $|n_3|$ the momenta of the decay tracks have large z components and so suffer from the poor resolution in the charge division coordinate. Furthermore, the tracks tend to have fewer hits and, being largely in the direction of the magnetic field, they have little curvature. This results in a less accurate measurement of the momentum.

Fig. 6.9 shows the K^0_S mass spectrum for different ranges of $|n_3|$. A loss in reconstruction efficiency is seen as $|n_3| \rightarrow 0$, so all V^0's with $|n_3|$ <0·3 were rejected. The decay plane normal is ill-defined for V^0's with very small opening angles such as gamma conversions. These, however, are efficiently removed by the p_d and $\cos\theta^*$ cuts. The width of the distributions shown in fig. 6.9 is seen to increase with decreasing n_3 as the track parameters become less well measured. The $\pi^+\pi^-$ invariant mass spectra are shown in fig. 6.10 for different ranges of the mass error, σ_m. There is no γ component in the region $\sigma_m < 10MeV/c^2$ because in the production, a nominal $10MeV/c^2$ was added to σ_m for all V^0's satisfying the γ mass hypothesis, to allow for the large uncertainty in σ_m for almost co-linear tracks. For $\sigma_m > 40MeV/c^2$ the K^0_S signal is small compared to the background but these tend to be the higher transverse momentum K^0_S's with small opening angles. Adding a cut of $\sigma_m > 40MeV/c^2$ to the production cuts reduces the K^0_S reconstruction efficiency (calculated as described in chap. 7) by a factor of 1·8±0·2 at p_t=5GeV/c, so to maintain statistics at high p_t no cut was made on σ_m.

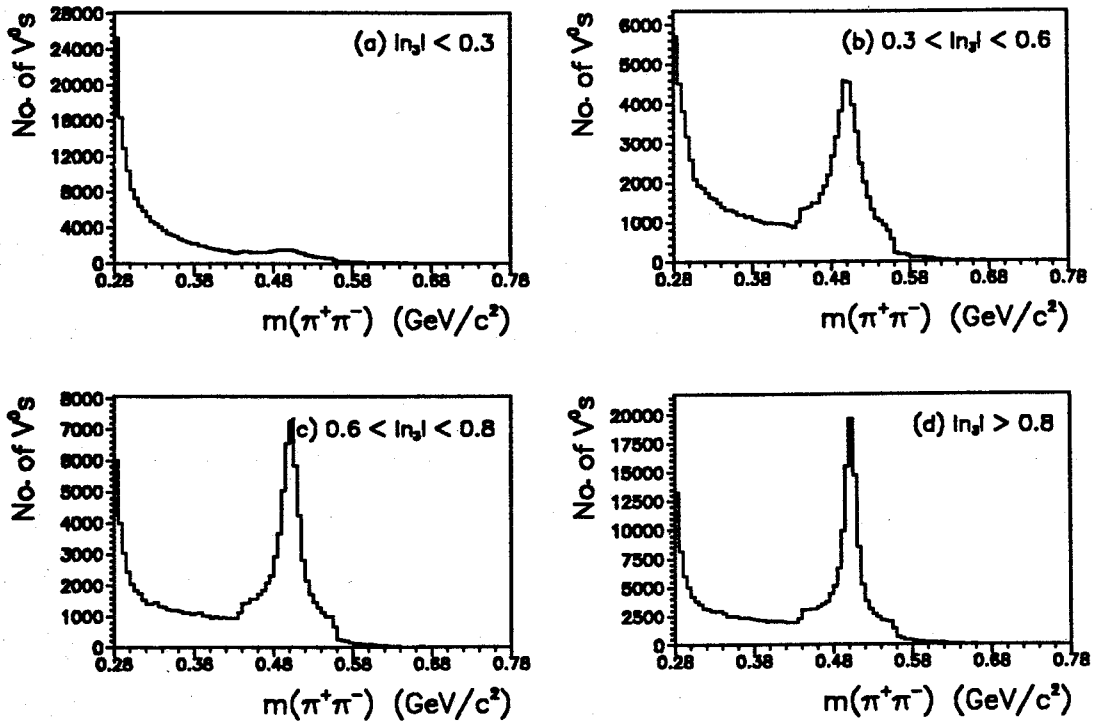

Figure 6.9: Mass spectra for K^0_S hypothesis as a function of n_3.

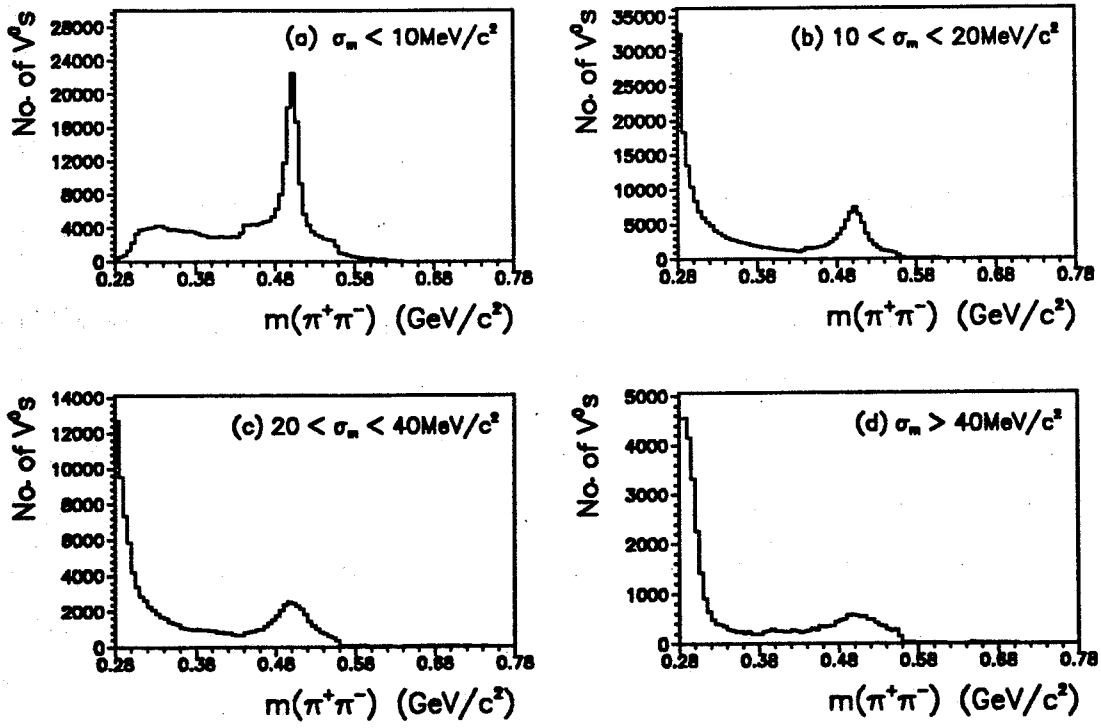

Figure 6.10: Mass spectra for the K^0_S hypothesis as a function of the mass error.

6.5 K^0_S/Λ ambiguities

It is possible for V^0 candidates to have a sensible reconstructed mass for both the K^0_S and the $\Lambda/\bar{\Lambda}$ hypotheses. Due to the low Q-value for the $\Lambda \rightarrow p\pi$ decay, and since the proton is much heavier than the pion, Λ decays are asymmetric in the laboratory frame with the proton emitted forwards in the Λ direction. Mis-identification of Λ decays can occur with the momentum imbalance of the pion and proton being absorbed by the Lorentz boost to the (assumed) K^0_S rest-frame in which the decay tracks will be at small angles with respect to the K^0_S line of flight. The $\cos\theta^*$ distribution is therefore peaked at +1 due to mis-assigned $\Lambda \rightarrow p\pi^-$ decays and at -1 due to $\bar{\Lambda} \rightarrow \bar{p}\pi^+$. The $\cos\theta^*$ cut described above removes the Λ decays which contaminate the K^0_S sample. Fig. 6.11 is the Dalitz plot for the K^0_S and $\Lambda/\bar{\Lambda}$ hypotheses for the production cuts only, which is to be compared with fig. 6.12 which has in addition the cut $|\cos\theta^*| > 0{\cdot}75$. With the $\cos\theta^*$ cut,

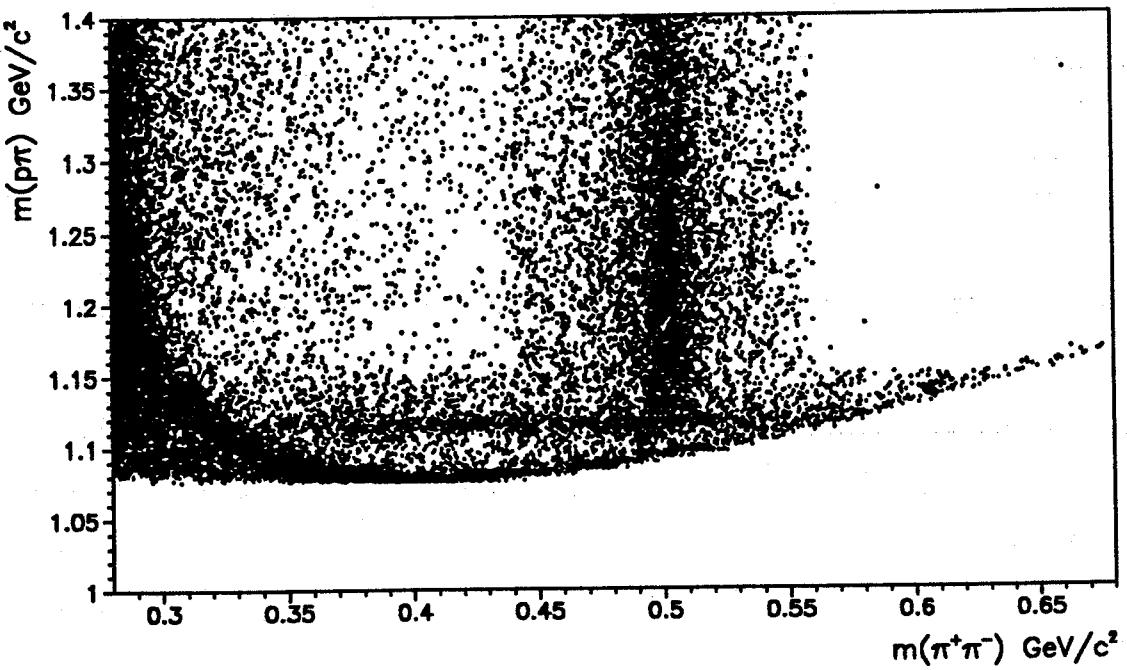

Figure 6.11: K^0_S – $\Lambda/\bar{\Lambda}$ Dalitz plot (production cuts)

no Λ or $\bar{\Lambda}$ signal is seen for candidates falling in the loose mass window of the K^0_S

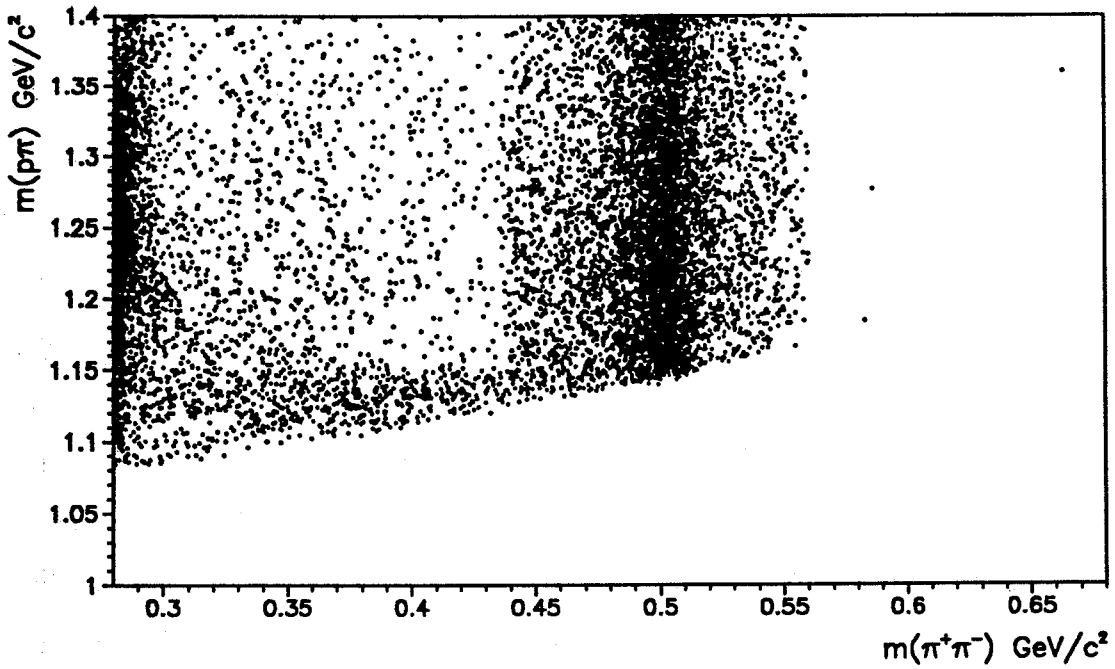

Figure 6.12: K^0_S – $\Lambda/\bar{\Lambda}$ Dalitz plot (production and $|\cos\theta^*|$ >0·75 cuts)

hypothesis. By cutting all V^0s with $|\cos\theta^*|$ >0·75 under the K^0_S hypothesis, no cut was needed on the V^0 invariant mass for the $\Lambda/\bar{\Lambda}$ hypotheses.

6.6 Track-sharing ambiguities

It is possible for two or more V^0 candidates to share common tracks although after the application of the cuts described less than 1% of the candidates in the tight mass window were ambiguous. These ambiguities were resolved by taking the V^0 candidate with the smallest impact parameter and rejecting any other V^0s sharing a track with it.

6.7 K^0_S mass spectrum and signal/background ratio.

Fig. 6.13 shows the invariant mass spectrum for the K^0_S hypothesis after all the cuts described have been applied to the V^0 sample (the horizontal scale is chosen for

compatibility with fig. 6.14). The effect of the production mass window (shown by the arrows in fig. 6.13) is clearly seen. There is clearly still a significant

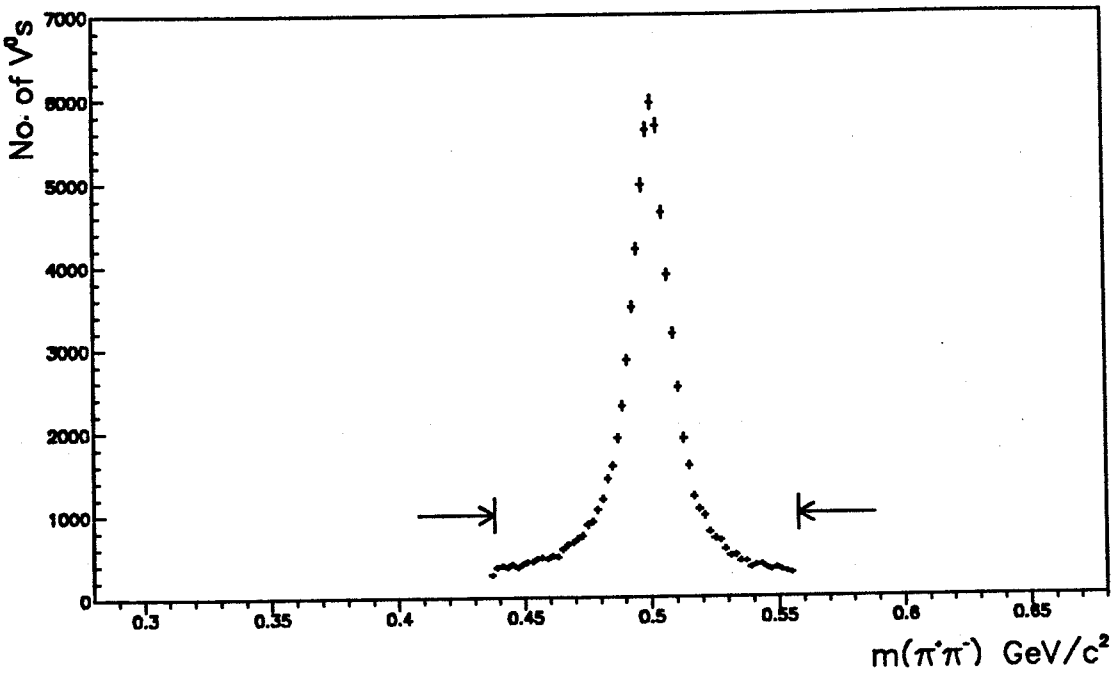

Figure 6.13: Mass spectrum for K^0_S hypothesis (all cuts).

background. The spectrum is, however, not wide enough for the background under the peak to be estimated by interpolation from the signal-free regions on either side. It was not possible to simply re-run the V^0 finding algorithm using a wider mass window since the raw hit information, which is needed for the track-fitting, was not retained after the original event processing. A sample of over 80000 raw events was therefore re-processed with the mass window, for the K^0_S hypothesis, widened to $m_{K^0} \pm 200 MeV/c^2$. The K^0_S mass spectrum for this sample is shown in fig. 6.14. The shape of the K^0_S background is now more apparent.

As discussed in appendix D, $1/p$ has a gaussian error distribution. Thus, the momentum and the invariant K^0_S mass errors are non-gaussian. Apart from the slightly wider tails, however, the mass peak is reasonably approximated by a gaussian. The mass peak has therefore been fitted with the sum of two gaussians with

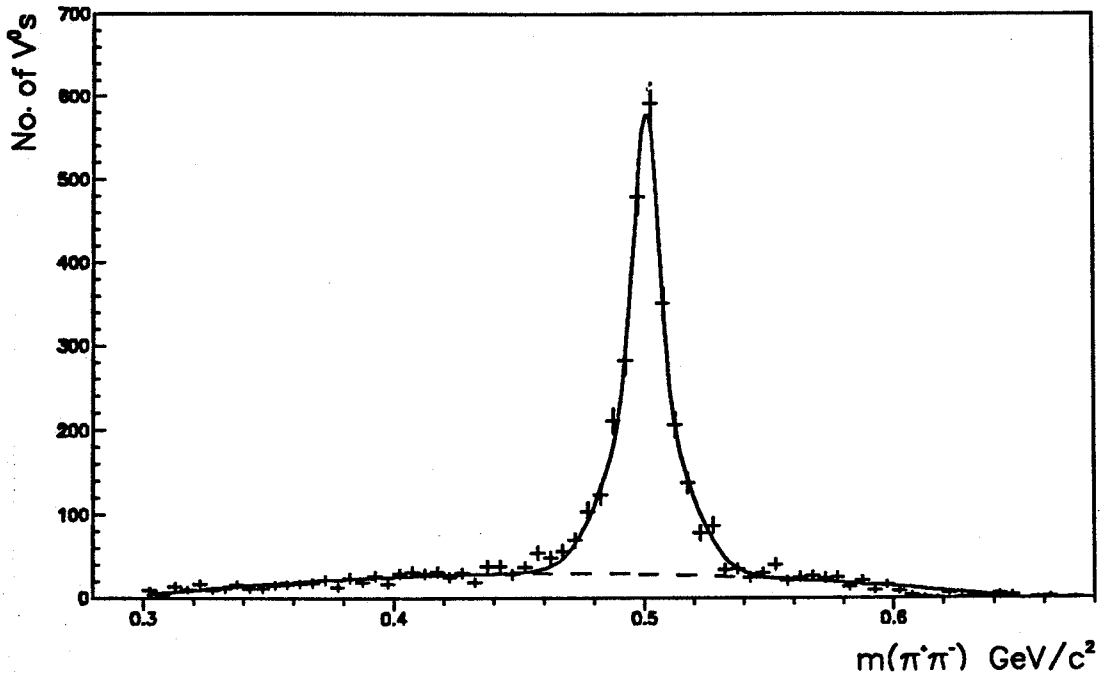

Figure 6.14: Mass spectrum for K^0_S hypothesis (all cuts and mass window of $m_{K^0} \pm 200 MeV/c$.

different widths but constrained to have the same mean value. [1] The background has been approximated by a second order polynomial. The solid line of fig. 6.14 shows the result of a fit of the form

$$f(m) = (A + Bm + Cm^2) + \frac{De^{-(m-\bar{m})^2/2\sigma_1^2}}{\sqrt{2\pi}\sigma_1} + \frac{Ee^{-(m-\bar{m})^2/2\sigma_2^2}}{\sqrt{2\pi}\sigma_2} \qquad (6.8)$$

The dashed line shows the polynomial background under the K^0_S mass peak.

In order to obtain the final K^0_S mass and the signal:background ratio, a fit was made to the mass spectrum for the full K^0_S sample. The shape of the background, obtained from the fit of the wide mass window sample, was imposed by allowing A to vary and constraining the ratios $B:A$ and $C:A$. The resulting fit is shown in fig. 6.15. The K^0_S mass, obtained from the full data sample was

[1] This form has been checked using a Monte-Carlo sample of 24000 single K^0_S's generated with the experimentally measured p_t spectrum. The simulated decay track digitisations were mixed with those of a real event and the standard reconstruction algorithm was applied. The reconstructed and the Monte-Carlo decay tracks were then matched to give a background-free K^0_S sample (see chapter 7 for a detailed discussion of this technique).

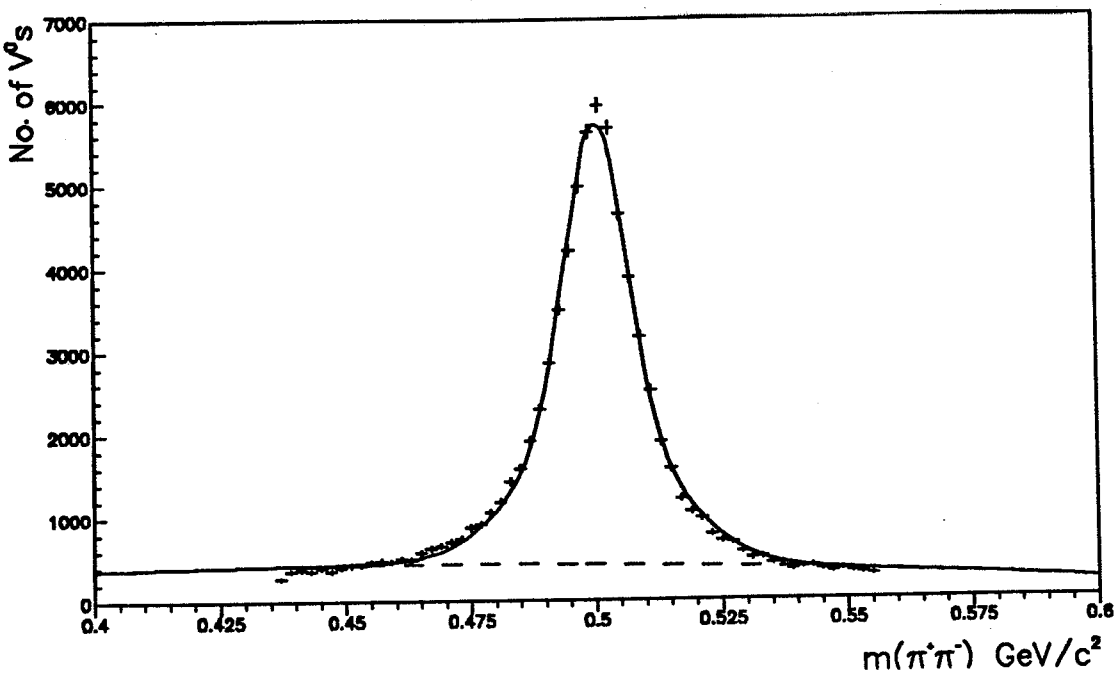

Figure 6.15: Fit to K^0_S mass spectrum (all cuts)

$$m(K^0_S) = (500.3 \pm 0.3) MeV/c^2 \tag{6.9}$$

The full width at half maximum (FWHM) of the gaussian (measured with the background subtracted) is $17{\cdot}2 GeV/c^2$. The mass is in excellent agreement with the accepted value [14] of $m(K^0_S) = (497{\cdot}671 \pm 0{\cdot}030) MeV/c^2$. The 0·5% discrepancy could be attributed to a systematic error in p_{xy} arising from the uncertainty in the magnetic field. It could, however, also be due to the residual error in the dip angle (see §4.4). The use of the K^0_S mass measurement to make a *global* correction to the momentum of each track is therefore not justifiable.

The K^0_S's used to obtain the cross-section are required to be within the tight mass window of $m_{K^0_S} \pm 20 MeV/c^2$. From the fit to the K^0_S mass spectrum, the signal to background ratio is $\mathcal{S}/\mathcal{B}$= 6·16, corresponding to K^0_S purity of $\mathcal{P} = \mathcal{S}/(\mathcal{S}+\mathcal{B})$ =86·0%.

To obtain a final cross-section a correction has to be made for the K^0_S's excluded by the tight mass window requirement. From the fit to the mass-spectrum, the fraction of genuine K^0_S's with a reconstructed mass inside this window was found to

be $f_W = 91{\cdot}1\%$. The K^0_S data were corrected by scaling the measured cross-section, within the tight mass window, as follows:

$$\partial\sigma(p_t, \phi, \eta) \rightarrow \partial\sigma(p_t, \phi, \eta) \times \frac{\mathcal{P}}{f_W} \tag{6.10}$$

7. K^0_S reconstruction efficiency

In order to calculate the K^0_S production cross-section it is necessary to know, for all regions of phase-space, the efficiency of the K^0_S-finding method described in Chapter 6. A previous study [55] used a sample of 50000 Isajet Monte-Carlo [39] events. These were passed through the UA1 detector simulation program and fully reconstructed. The V^0-finding algorithm, described in §6.1, was then applied to yield a K^0_S efficiency:

$$\epsilon_{MC}(p_t, \phi, \eta) = \frac{\text{No. of } K^0_S \text{ found}}{\text{No. of } K^0_S \text{ generated}} \tag{7.1}$$

To achieve high statistics for all momentum ranges, a similar study was made [56] in which single K^0_S's were generated. These were forced to decay to a pair of charged pions in an otherwise empty detector. After detector simulation and event reconstruction, the efficiency is also given by equation 7.1. These two methods were consistent within errors, showing the independence of the efficiency on the surrounding tracks, at least for simulated events. The efficiencies obtained by these purely Monte-Carlo methods prove to be over-optimistic.

A method has been developed [54] for evaluating the efficiency of reconstructing K^0_S decays which relies less on the detector simulation by using information from real events. A single K^0_S is generated, with some chosen p_t, η, and ϕ and its decay is simulated in an empty detector. The raw hits on the CD wires, caused by the two charged pions from the K^0_S are then combined with those from a *real* event. Noise and systematic effects in the real events make the track reconstruction more difficult resulting in a lower, and more realistic, efficiency compared to the single K^0_S method. The *single* K^0_S efficiency was evaluated for five p_t and twenty $\eta\phi$ bins.

A correction was then made, to allow for the coarseness of the p_t binning, using the detailed p_t variation of a single "average" $\eta\phi$ bin. The efficiency for K^0_S-finding in mixed events was evaluated for five bins in p_t and applied to the single K^0_S result to account for the relative ease of reconstructing an isolated Monte-Carlo K^0_S compared to one in real event.

In this analysis, the single and mixed efficiency methods are also combined since the CPU time required for full event reconstruction precluded the use of solely mixed events. The high statistics of the sample, however, necessitated a more complete treatment. In particular, the detailed variation of the efficiency with p_t has been measured and the dependence of the mixed K^0_S efficiency on η and ϕ taken into account. In mixing a Monte-Carlo generated K^0_S with a real event, the correct treatment of the primary vertex is important since a major requirement in the V^0 reconstruction is the association of the V^0 and the non-association of its decay products to the primary vertex. The treatment of the K^0_S at the primary vertex is discussed in §7.1. The multiple scattering of the charged pions in the beam-pipe and CD chamber walls affects the impact parameter of the reconstructed K^0_S. This effect has been included in the standard detector simulation (see §7.2).

7.1 K^0_S primary vertex

The K^0_S is initially generated at (0,-15mm,0) [1] while the primary vertex of the real event in which it is merged may be some distance away (fig. 3.5). The K^0_S starting point is therefore redefined, prior to simulation, to be the measured vertex coordinates, $(x^{evt}_{vtx}, y^{evt}_{vtx}, 0)$, smeared according to the associated errors, σ_x and σ_y.

The vertex error distribution, shown in fig. 7.1, is derived by the track fit to the vertex, as described in §3.4. The large spread of the vertex position in x is

[1] The nominal beam position in y is at -15mm so this is the standard number used in the Monte-Carlo. In 1987 the real position was at $y \approx -24{\cdot}8mm$ (fig.3.5).

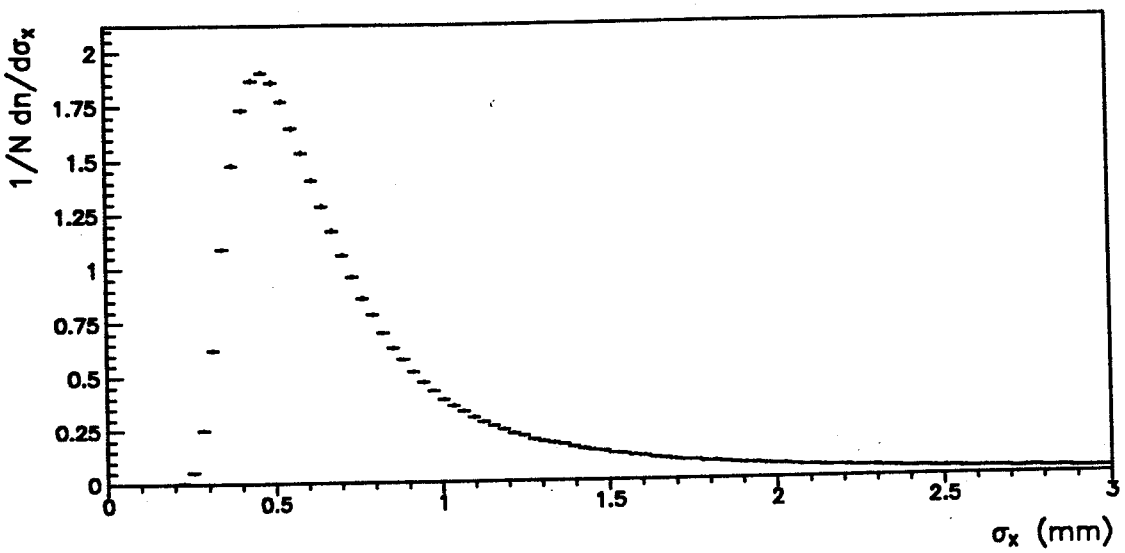

Figure 7.1: Primary vertex error distribution in x

due to the length of the p and $\bar{p}$ bunches. As a result, the error, σ_x, on the vertex position in x is considerably larger than the error, σ_y, in y. In minimum-bias events this is exacerbated by low track multiplicities particularly transverse to the beam direction which make the x measurement more difficult. The x coordinate of the K^0_S at the event vertex was defined to be

$$x^{K^0}_{z=0} = x^{evt}_{vtx} + \sigma_x \mathcal{G}_x \tag{7.2}$$

where $\mathcal{G}$ is a random number selected from a gaussian distribution of unit σ centered at zero, and σ_x is the x vertex error for the event.

To maintain luminosity, the beam position must be known to within about $100\mu m$ in y. Since this is used as a constraint in the vertex finding (§3.4), σ_y was taken to be $100\mu m$, from the width of the y_{vtx} distribution (fig. 3.5 (b)), so that:

$$y^{K^0}_{z=0} = y^{evt}_{vtx} + \sigma_y \mathcal{G}_y \tag{7.3}$$

Both the K^0_S and the real event vertices are at $z = 0$ by definition.

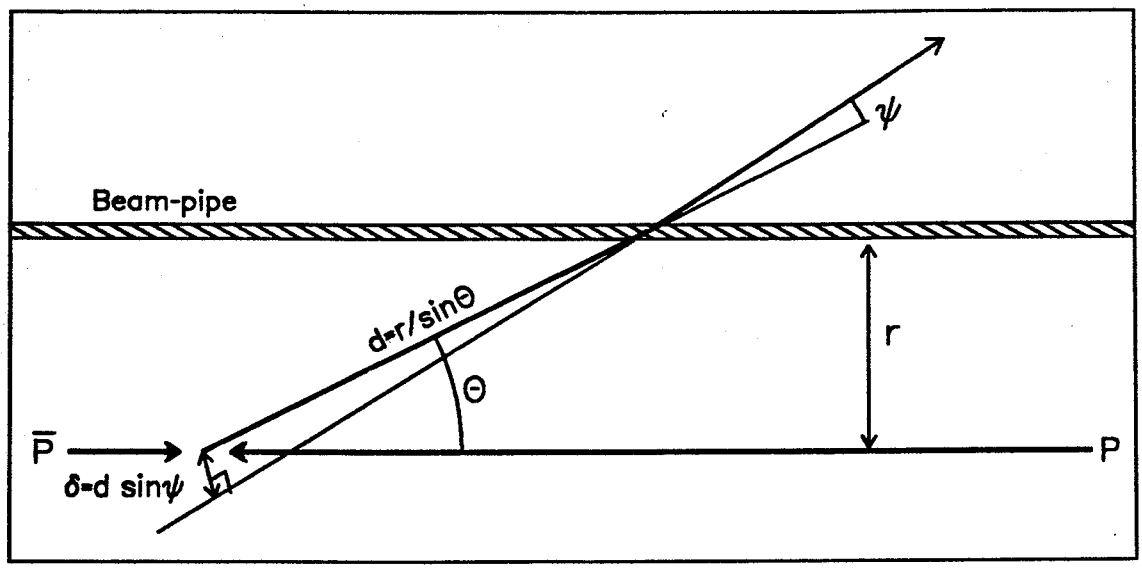

Figure 7.2: Geometry of multiple scattering

7.2 Simulation of Multiple Scattering

The multiple Coulomb scattering of charged particles in the beam-pipe and CD chamber walls does not greatly alter the measured track parameters. It can, however, have a significant effect on the impact parameters of the pions and the K^0_S, and hence on the reconstruction efficiency. The detector simulation allows charged particles to proceed through the detector in small steps correcting the track parameters for energy loss in the material but not for multiple scattering.

The angular deviation ψ (fig. 7.2) of a track of energy E and momentum p, passing through L/L_R radiation lengths of material, may be parametrised [57] by a gaussian distribution of width

$$\sigma_\psi = 14.1 MeV/c \times \frac{E}{p^2}\sqrt{\frac{L}{L_R}}\left(1+\tfrac{1}{9}\log_{10}(L/L_R)\right) \quad \text{radians} \qquad (7.4)$$

This expression was used to simulate the multiple scattering of the K^0_S decay products in the beam-pipe and CD walls. The correction ψ to the track was chosen randomly from a normal distribution of width σ_ψ. The azimuthal angle of the shift about the unscattered track direction was randomly chosen assuming a flat distribution. The multiple scattering in the beam-pipe was found to be the

dominant contribution to the uncertainty in the impact parameter. The beam-pipe is corrugated to prevent low angle tracks from passing through a large thickness of material so the number of radiation lengths was approximated by a constant $L/L_R = 0.025$.

The displacement, $\delta = r\sin\psi/\sin\theta$, of the track at the primary vertex corresponds to a mean shift in each vertex coordinate of

$$\delta_i = \frac{1}{\sqrt{3}}\left(\frac{r\sin\psi}{\sin\theta}\right) \qquad (i = x, y, z) \tag{7.5}$$

where θ is the angle of the track with respect to the beam (fig. 7.2). For example, for a 0·5GeV pion passing through a beam-pipe of radius $r = 10cm$, $\sigma_\psi \approx 5mrad$ which gives, for $\theta = 45°$, a displacement in x, y, or z of $\delta_i \approx 0{\cdot}37mm$ at the vertex, corresponding to $0{\cdot}53mm$ in the bending plane.

7.3 Single K^0_S efficiency

A single K^0_S is generated at a specific p_t, with η and ϕ randomised within specified intervals of $\Delta\eta$ and $\Delta\phi$. The fourfold ϕ symmetry of the detector is exploited by only generating K^0_S's in the first quadrant, which is subdivided into four intervals: [0,22·5°], [22·5°,45°], [45°,62·5°], and [62·5°,90°]. Similarly, the rapidity is assumed to be symmetric about the $x = 0$ plane and divided into five bins: [0,0·5], [0·5,1·0], [1·0,1·5], [1·5,2·0], and [2·0,2·5]. For each $\eta\phi$ bin, the efficiency is calculated for nineteen non-equidistant values of p_t (see figs. 7.3-7.6). The generated K^0_S is allowed to decay in the detector, with an exponential lifetime distribution, under the constraint that the two pions produced are charged. These are then tracked through the CD and the hits on the wires are simulated. The event is reconstructed and the V^0-finding software attempts to find the K^0_S in the otherwise empty detector. A new K^0_S is then generated at the next value of p_t and the procedure is repeated. This method is applicable for an arbitary set of values of the cuts described in chapter 6, since the V^0-finding software used is identical to

that used for real data.

The efficiencies for reconstructing a single K^0_S, as a function of p_t and for all $\phi - \eta$ bins, are shown in figs. 7.3-7.6. The efficiency is small at low p_t due to the cut in the decay track p_t of $100MeV$ and because these K^0_S's do not benefit from the time-dilation factor so the decay tracks tend to be associated to the primary vertex. The greater multiple scattering for low momentum particles also reduces the probability of reconstructing the K^0_S. The efficiency decreases at high p_t since the decays occur futher into the CD resulting in shorter measured pion tracks. Such decays have smaller opening angles which can result in losses due to the non-association requirement of the cut $\chi^2_{i,all} < 4$ applied to both tracks.

The efficiency as a function of η and ϕ is shown in fig. 7.7, for three values of p_t. The efficiency increases with ϕ since decay tracks are better measured in the bending plane. This effect is enhanced by the decay plane cut described in §6.4. At high η the efficiency is low, largely due to the fiducial cut in Φ while at low η the reduced track length (and hence number of points) reduces the efficiency.

7.4 Mixed K^0_S efficiency

The mixed K^0_S efficiency has been evaluated for five ranges of p_t ([0·2,0·5], [0·5,1·0], [1·0,3·0], [3·0,5·0] and [5·0,10·0]), with two bins in ϕ ([0,45°] and [45°,90°]) and two in η ([0,1·25] and [1·25,2·5]).

First, a real minimum-bias event, including the CD raw hit information, is read from cassette and held in memory. As for the single K^0_S case, a Monte-Carlo K^0_S is generated and its decay in the detector is simulated. If the K^0_S is successfully reconstructed in the empty detector, then the simulated raw hits are merged with those of the real event. All the digitisings are then passed through the standard track-reconstruction. If greater than 50% of the hits of a given track originate from the Monte-Carlo then that track is flagged with its Monte-Carlo track code. The V^0-finding algorithm is then applied to these tracks alone. The procedure is

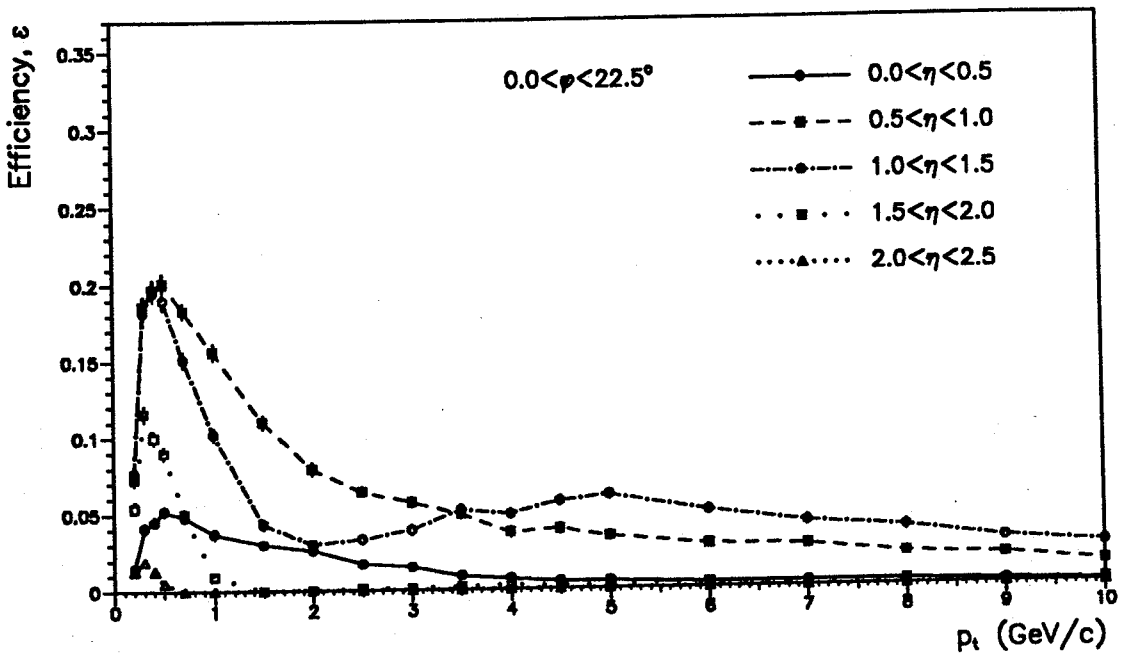

Figure 7.3: Single K^0_S efficiency vs. p_t ($0 \leq \phi < 22.5°$)

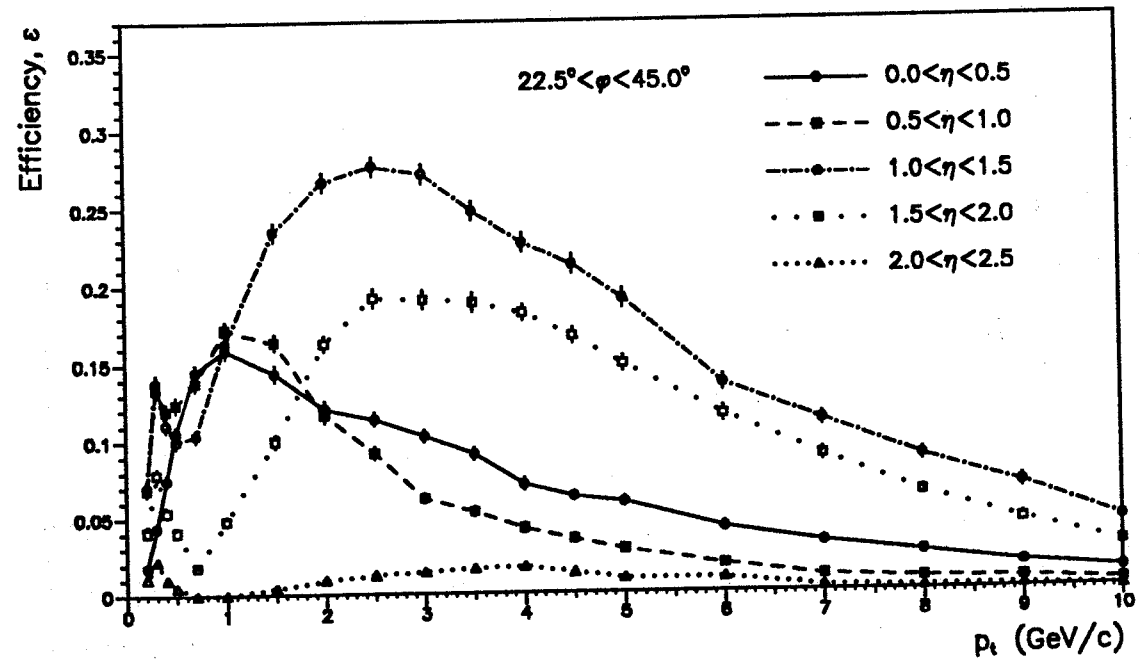

Figure 7.4: Single K^0_S efficiency vs. p_t ($22.5° \leq \phi < 45.0°$)

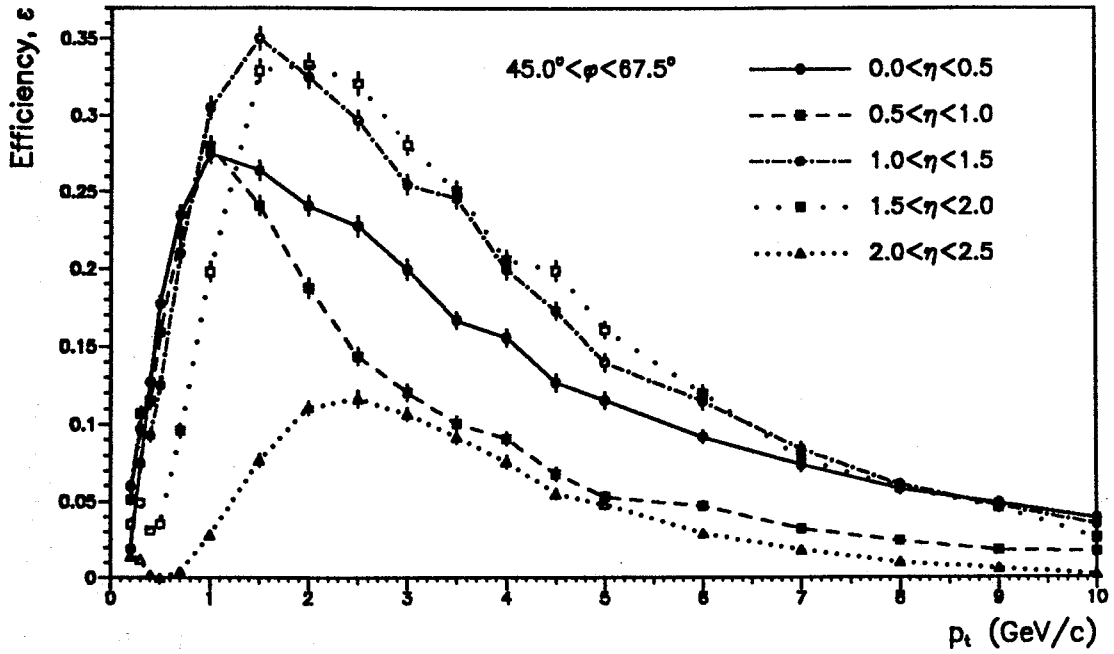

Figure 7.5: Single K^0_S efficiency vs. p_t (45·0°$\leq \phi <$67·5°)

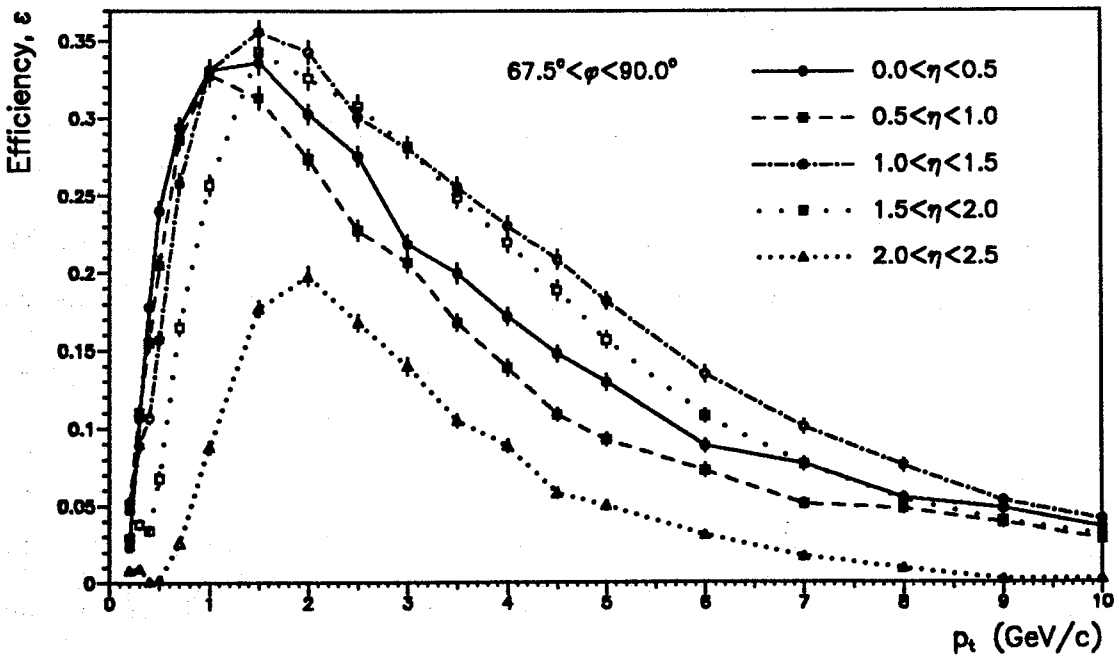

Figure 7.6: Single K^0_S efficiency vs. p_t (67·5°$\leq \phi <$90·0°)

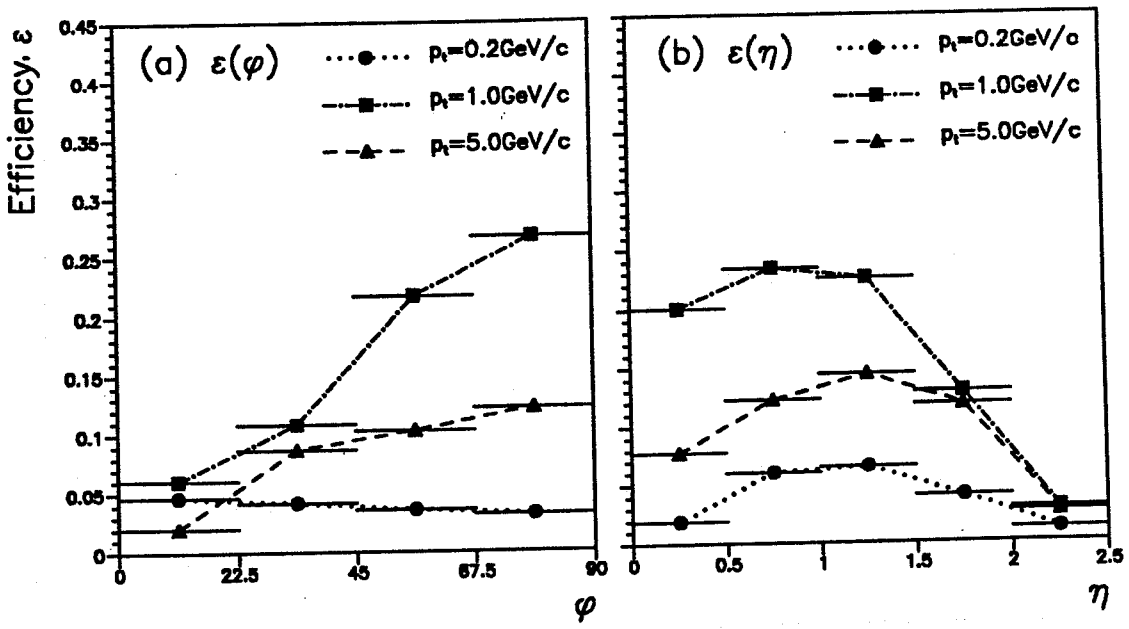

Figure 7.7: Single K^0_S reconstruction efficiency vs. (a) ϕ and (b) η.

repeated for the next value of p_t, until the maximum value ($10 GeV/c$) is reached whereupon the real event is dropped and another is read in. A correction factor, $C_\epsilon(p_t, \phi, \eta)$, which measures the relative probability of finding the K^0_S after and before mixing with a real event, is therefore defined as

$$C_\epsilon(p_t, \phi, \eta) = \frac{\text{No. of } K^0_S \text{ found after mixing}}{\text{No. of } K^0_S \text{ found before mixing}} \tag{7.6}$$

Table 7.1 gives $C_\epsilon(p_t, \phi, \eta)$, expressed as a percentage. The values of C_ϵ vary by only 20% within a given $\eta\phi$ bin and by 30% over all phase-space. The difference between the single and mixed efficiencies is greatest for $0 \leq \phi < 45°$ and $0 \leq \eta < 1{\cdot}25$ where the track parameters depend more on the z coordinate.

The finite resolution of the CD results in a spread of the reconstructed K^0_S track parameters with respect to those of the generated K^0_S. As discussed in app. D this can result in significant smearing of rapidly changing distributions. For the efficiency this introduces the question of whether a K^0_S generated with particular values of p_t, ϕ and η is reconstructed with very different values. If this is the case then the differences between the efficiency as a function of the generated

	$0 \leq \phi < 45°$		$45° \leq \phi < 90°$	
	$0 \leq \eta < 1.25$	$1.25 \leq \eta < 2.5$	$0 \leq \eta < 1.25$	$1.25 \leq \eta < 2.5$
$0{\cdot}2 \leq p_t < 0{\cdot}5$	77·1±1·2	82·8±1·5	78·0±1·2	77·5±2·1
$0{\cdot}5 \leq p_t < 1{\cdot}0$	69·5±1·5	89·1±1·7	82·6±0·7	86·5±1·0
$1{\cdot}0 \leq p_t < 3{\cdot}0$	63·5±1·5	88·1±1·3	83·2±0·7	86·7±0·7
$3{\cdot}0 \leq p_t < 5{\cdot}0$	61·3±2·0	84·1±1·4	79·7±1·0	83·5±0·9
$5{\cdot}0 \leq p_t < 10{\cdot}0$	61·8±2·7	70·6±2·4	75·0±1·7	75·4±1·8

Table 7.1: Mixing correction factor, $C_\epsilon(p_t, \phi, \eta)$ (%)

and reconstructed parameters must be considered. To address this question, the changes in the K^0_S parameters due to the reconstruction of the mixed event have been studied. The difference, $(p_t^{gen} - p_t^{rec})$, in the generated and reconstructed transverse momenta is shown in fig. 7.8 for different ranges of p_t. As expected the difference is larger at high p_t where the resolution is worse, but the widths of the distributions are in all cases much smaller than the distance between the points at which the efficiency is evaluated. The shift in η and ϕ is measured by the quadratic combination of the individual shifts, *i.e.* $\Delta R = \sqrt{(\Delta\eta)^2 + (\Delta\phi)^2}$, where $\Delta\phi$ is measured in radians. Fig. 7.9 shows that ΔR, for all p_t, is small compared to each bin which measures $\Delta\eta \times \Delta\phi = 0{\cdot}5 \times 0{\cdot}39$. The efficiency is therefore assumed to be the same as a function of the reconstructed and the generated K^0_S parameters.

7.5 Full K^0_S efficiency

Since the single K^0_S efficiency is evaluated at discrete p_t values, and is quite rapidly changing with p_t, a way of obtaining it for an arbitary p_t is needed. For a given $\eta\phi$ bin, an empirical fit of the form $\epsilon_S(p_t) = Ap_t^\alpha(1 - e^{\beta p_t + \gamma p_t^2})$ reproduced the efficiency distributions well apart from a slight systematic difference in the region

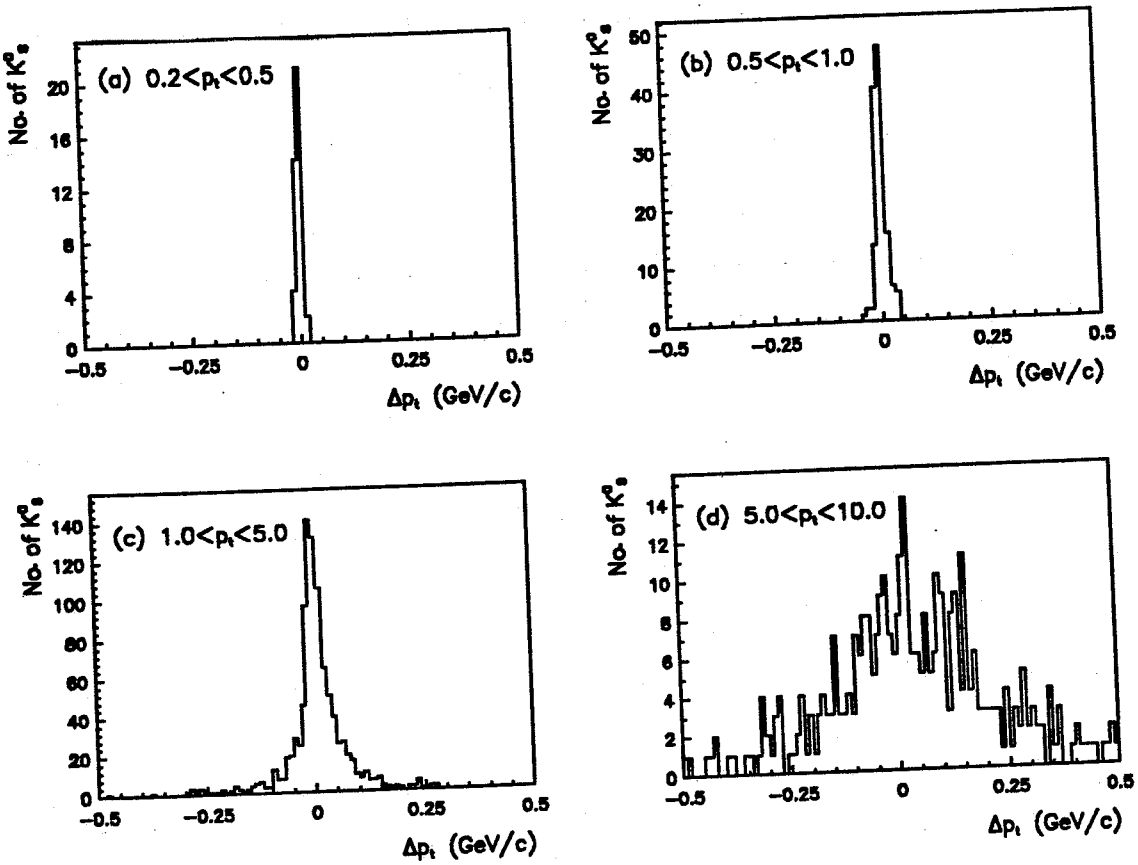

Figure 7.8: Change in K^0_S p_t after reconstruction

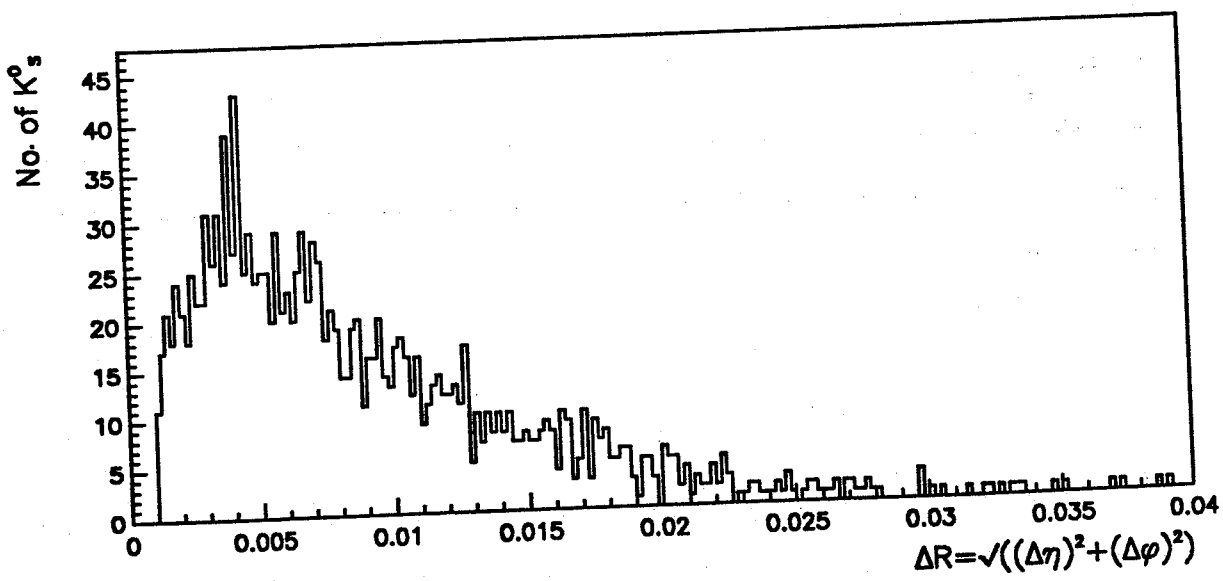

Figure 7.9: ΔR of reconstructed K^0_S *c.f.* generated K^0_S.

1-3GeV/c. The interpretation of the error on ε_S from such a fit is, however, difficult unless there is an underlying physical reason for the functional form. Therefore, to preserve generality, both the efficiency and its associated error were obtained at an arbitrary p_t by interpolation.

It can be seen from figs. 7.3-7.6 that the single K^0_S efficiency is close to zero for some regions of phase-space, particularly at high rapidity as a result of the fiducial Φ cut described in §6.4. For such regions, the error on the corrected number of K^0_S's is large. A threshold efficiency of ε_t has therefore been applied. It is desirable to choose a value of ε_t such that for $\varepsilon_S(\eta, p_t) > \varepsilon_t$ for at least one of the four ϕ ranges, for all the η and p_t regions. Then, setting $\varepsilon_S = 0$ if it is below ε_t and assuming the cross-section is flat in ϕ, the efficiencies above ε_t for a given η and p_t and different ϕ can re-scaled and both the η and p_t distributions can be evaluated. The efficiency at high rapidity and low p_t is, however, close to zero for *all* ϕ bins. The K^0_S cross-section is therefore assumed to be flat in both ϕ and η, and for fixed p_t the threshold is applied such that

$$\varepsilon_S(\phi,\eta) = \begin{cases} \varepsilon_S(\phi,\eta) \times \left(\frac{N_{\text{bins}}}{N_{\text{bins}}(\varepsilon_S(\phi,\eta)\geq\varepsilon_t)}\right) & ; \text{ if } \varepsilon(\eta,\phi) \geq \varepsilon_t \\ 0.0 & ; \text{ if } \varepsilon(\eta,\phi) < \varepsilon_t \end{cases} \tag{7.7}$$

where N_{bins} is the number of bins in ϕ and η. A threshold of ε_t =3% was chosen with the result that for $p_t < 6GeV/c$, 63 of the efficiency values (from a total of 280) were set to zero. For no value of p_t were all the efficiencies in ϕ and η below threshold.

The full K^0_S-finding efficiency, as a function of p_t, ϕ and η, is given by

$$\varepsilon(p_t,\phi,\eta) = \varepsilon_S(p_t,\phi,\eta) \times C_\varepsilon(p_t,\phi,\eta) \tag{7.8}$$

The efficiency correction is applied by scaling the number of reconstructed K^0_S's by a factor $1/\varepsilon(p_t,\phi,\eta)$. The error on the K^0_S p_t distribution due to the efficiency is 4% almost independently of p_t.

8. Inclusive K^0_S cross-section and K/π ratio

The inclusive production of K^0_S mesons has been studied by reconstructing the decay $K^0_S \rightarrow \pi^+\pi^-$ in the region -2·5 < y < 2·5 and 0 < ϕ < 2π. A total of 2 031 800 minimum-bias events have been analysed, yielding a sample of more than 91 000 K^0_S candidates satisfying the cuts described in chapter 6.

8.1 Lifetime

The K^0_S lifetime provides a check on the validity of the V^0 analysis. The lifetime, t, is related to the decay length, d by

$$ct = \frac{d}{\beta\gamma} \tag{8.1}$$

where $\beta\gamma = p/m$ is the time-dilation factor. Since the z resolution of the CD is comparable with a typical decay length the error on ct is considerable. The vectors describing the decay length and the V^0 momentum are, however, co-linear so the z-dependence may be factorised out and the lifetime written

$$ct = \frac{d_{xy}m}{p_{xy}} \tag{8.2}$$

Since this expression relies only on information from the track fit in the bending-plane the error on ct is a factor of $\sim$ 100 times smaller. The K^0_S lifetime is presented in fig. 8.1, where the errors shown are statistical. The distribution has been corrected for the reconstruction efficiency, calculated as a fuction of p_t, η and ϕ, using the method described in chapter 7. The drop in the distribution for short lifetimes is a result of the decay tracks being associated to the primary vertex. The distribution is truncated above three lifetimes ($ct > 8cm$) as a result of the cut in the decay

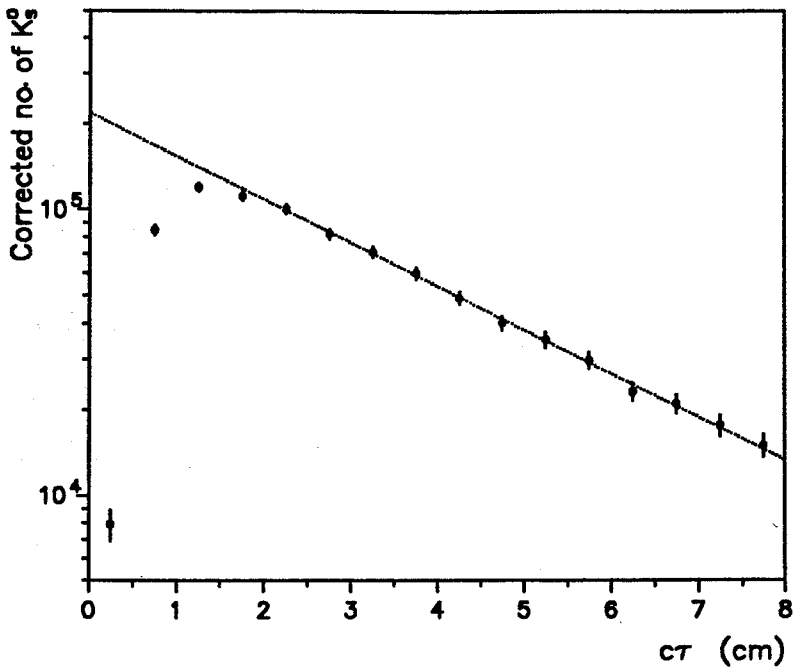

Figure 8.1: K^0_S lifetime (all cuts)

probability (defined in eq. 6.6) of $P_d > 0{\cdot}95$. The distribution has been fitted with an exponential distribution (shown by the dotted line in fig. 8.1), excluding the region $ct < 2cm$, yielding $c\tau_{meas} = (2{\cdot}86 \pm 0{\cdot}01)cm$ or $\tau_{meas} = (9{\cdot}56 \pm 0{\cdot}03) \times 10^{-11}s$. The lifetime is in reasonable agreement with the current world average value [14] of $c\tau = (2{\cdot}675 \pm 0{\cdot}006)cm$ or $\tau = (8{\cdot}92 \pm 0{\cdot}02) \times 10^{-11}s$. The reconstruction efficiency increases with increasing decay length. If the K^0_S sample were corrected with an efficiency depending explicitly on the decay length then the measured lifetime would decrease. The CPU time required prohibited such a study.

8.2 K^0_S cross-section

The invariant K^0_S cross-section as a function of p_t is shown in fig. 8.2 and listed in table 8.1. The statistical errors and the p_t-dependent errors in the K^0_S reconstruction efficiency have been combined in quadrature. The systematic error from the uncertainty in the minimum-bias cross-section is 7% (eq. 2.4). The data

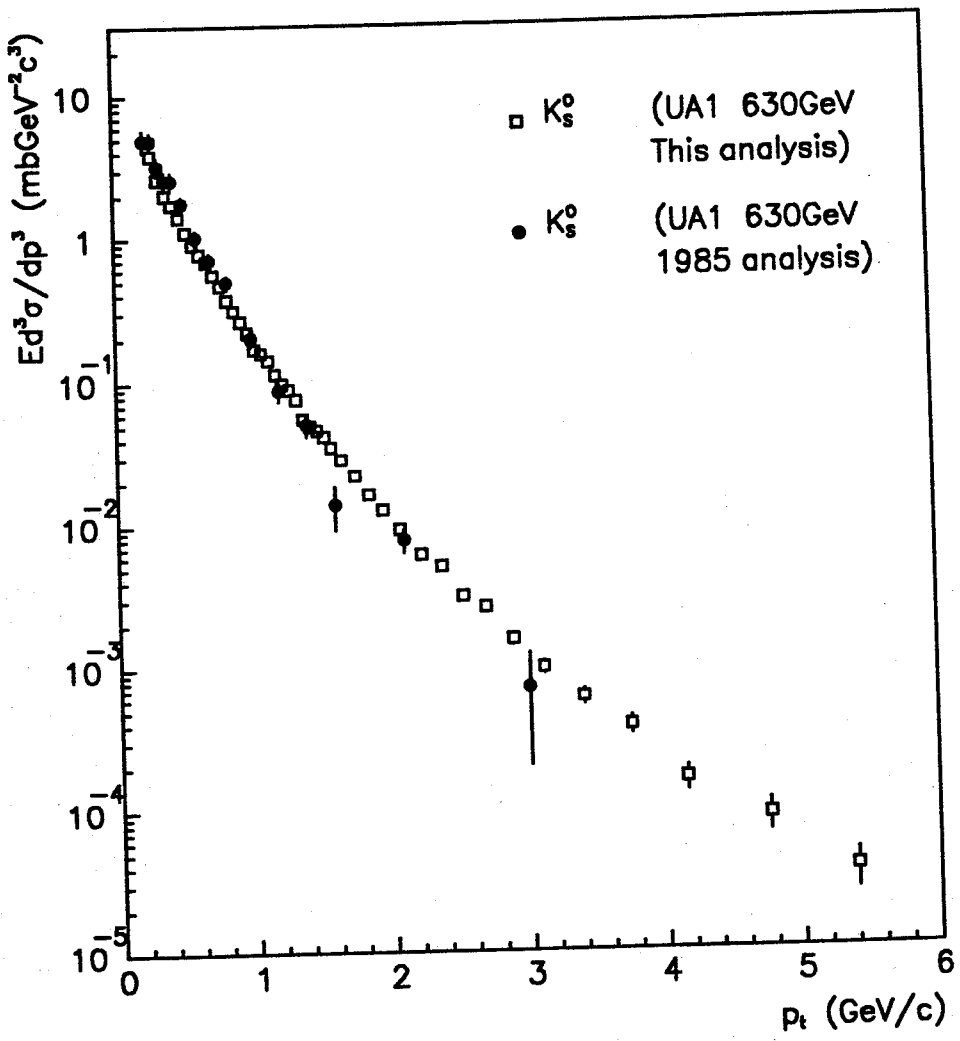

Figure 8.2: Inclusive K_S^0 cross-section measured by UA1 (the 1985 data are from ref. [58]).

p_t (GeV/c)	$Ed^3\sigma/dp^3$ $(mbGeV^{-2}c^3)$
0.225	6.425 ±0.127
0.275	3.866 ±0.066
0.325	2.631 ±0.046
0.375	2.031 ±0.036
0.425	1.731 ±0.030
0.475	1.408 ±0.025
0.525	1.114 ±0.020
0.575	0.9038 ±0.0163
0.625	0.7796 ±0.0142
0.675	0.6841 ±0.0126
0.725	0.5531 ±0.0105
0.775	0.4631 ±0.0090
0.825	0.3684 ±0.0076
0.875	0.3113 ±0.0067
0.925	0.2615 ±0.0058
0.975	0.2183 ±0.0050
1.025	0.1681 ±0.0042
1.075	0.1581 ±0.0040
1.125	0.1406 ±0.0037
1.175	0.1134 ±0.0032
1.225	0.0967 ±0.0029
1.275	0.0879 ±0.0027

p_t (GeV/c)	$Ed^3\sigma/dp^3$ $(mbGeV^{-2}c^3)$
1.325	0.0758 ±0.0025
1.375	0.0553 ±0.0020
1.425	0.0490 ±0.0018
1.475	0.0459 ±0.0018
1.525	0.0417 ±0.0017
1.575	0.0345 ±0.0015
1.649	0.02839 ±0.00097
1.749	0.02204 ±0.00083
1.850	0.01619 ±0.00069
1.948	0.01265 ±0.00061
2.072	0.00914 ±0.00041
2.225	0.00608 ±0.00032
2.370	0.00502 ±0.00029
2.524	0.00310 ±0.00024
2.689	0.00258 ±0.00019
2.888	0.00152 ±0.00014
3.108	0.000963±0.000099
3.400	0.000596±0.000072
3.749	0.000375±0.000051
4.153	0.000158±0.000029
4.763	0.000087±0.000021
5.399	0.000036±0.000011

Table 8.1: Inclusive K^0_S cross section, $Ed^3\sigma/dp^3(p\bar{p} \rightarrow K^0_S X)$

have been corrected for the K^0_S reconstruction efficiency and the branching ratio $B(K^0_S \rightarrow \pi^+\pi^-)$ =68·6%. The purity and mass window correction factors have been applied. The p_t value of each data point is the average of the p_t values of the individual K^0_S's within the bin *not* the value at the centre of the bin. The data are seen to be in good agreement with an independent UA1 analysis [58] of 3180 K^0_S's obtained from the 1985 minimum-bias data sample.

In fig. 8.3, the data are compared with the charged and neutral kaon inclusive cross-sections measured by the UA5 Collaboration [59] at $\sqrt{s}$= $546GeV$, and the charged kaon cross-section of UA2 at $\sqrt{s}$ = $540GeV$[60]. The data agree well within an overall normalisation factor which is due to a number of reasons: The UA2 trigger is more demanding than the minimum-bias trigger of UA1. In addition to a coincidence of hits in the up-stream and down-stream luminosity hodoscopes, hits are also required in hodoscopes covering the range $|\eta| < 0{\cdot}7$. This extra requirement tends to bias towards higher activity events which populate the central region. UA2 estimates a overall systematic error on the kaon cross-section of ±8% due to contamination from pions which could not be removed using the time-of-flight measurement. There is an additional systematic error of 17% in the overall normalisation due to the uncertainty in the trigger cross-section. The UA5 trigger is similar to the UA1 minimum-bias trigger so no appreciable difference is expected in the average physics content of the events. The non-single-diffractive cross-section assumed by UA5 was $\sigma_{\rm NSD}$ = $43{\cdot}2 \pm 1{\cdot}8mb$. As discussed in chapter 5, the value of $\sigma_{\rm NSD}$ used in 1985 was reduced by 13% following a recalibration of the UA1 luminosity monitors [26,27]. Probably, a similar correction should also be applied to the UA5 value of $\sigma_{\rm NSD}$. Since UA5 has no magnetic field, the mass of the K^0_S must be used as a constraint in the calculation of the p_t of the K^0_S. Thus, no subtraction of the background can be done using the mass spectrum from the *real* data. Instead they rely entirely on Monte-Carlo simulations which may underestimate the background. Furthermore, the UA5 geometrical efficiciency for

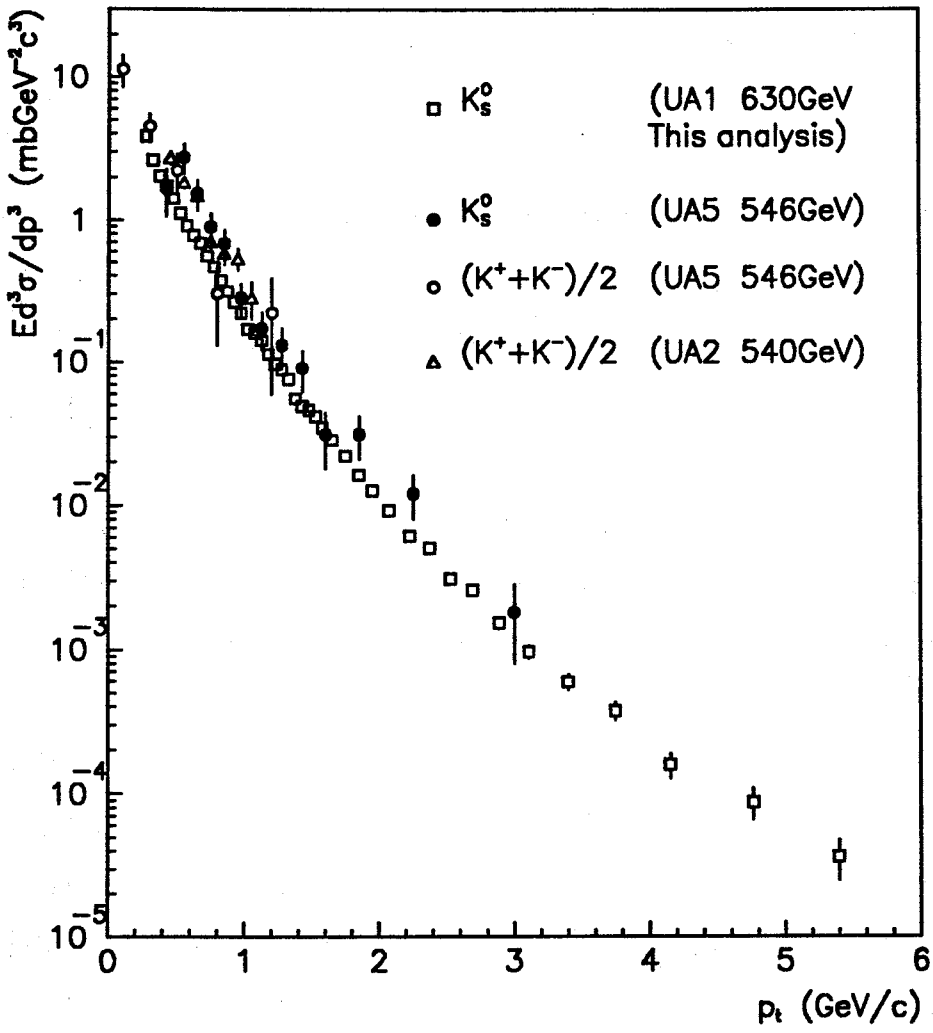

Figure 8.3: Inclusive K^0_S cross-section compared with UA5 [59] and UA2 [60] K^0_S and $K^{\pm}$ data.

K^0_S reconstruction is low (~4%) and therefore sensitive to systematic errors. For example, the efficiency increases by 30% if the mean K^0_S transverse momentum used in their Monte-Carlo is changed from $500 MeV/c$ to $600 MeV/c$. The statistical errors in the UA5 sample of $171 K^0_S$'s are also large, especially in the tail of their p_t distribution.

As discussed in chapter 5, the charged particle cross-section may be parametrised by an exponential in transverse mass at low p_t and by a power law for higher p_t (eq.5.3). Fig. 8.4 shows the result of this hybrid fit to the inclusive K^0_S cross-section. The fit parameters are given in table 8.2. The parameter A is constrained

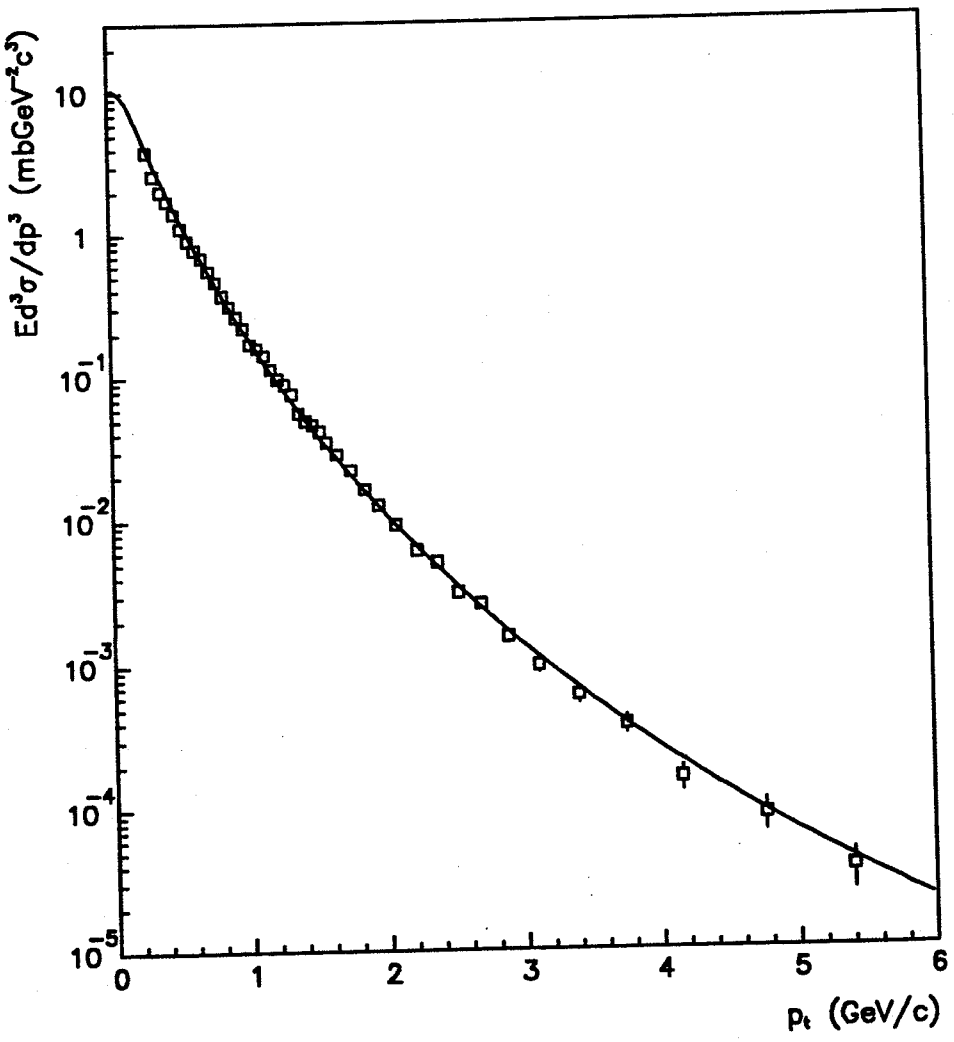

Figure 8.4: Hybrid fit to the inclusive K^0_S cross-section.

A ($mbGeV^{-2}c^3$)	p_0 (GeV/c)	n	p_1 (GeV/c)
15·53	1·65±0·03	9·00 ± 0·12	0·2 (fixed)

Table 8.2: Parameters of the hybrid fit to the inclusive K^0_S cross section.

by the overall normalisation of the data. The fit converged with $p_1 < 0{\cdot}2GeV/c$ so this parameter could not be determined from the data. Since the exponential in transverse mass is physically more justifiable than the power law at low p_t, the value of p_1 was set to $0{\cdot}2GeV/c$. Following the procedure described in appendix C, the mean number of K^0_S per event, $\langle n_{K^0_S} \rangle$, is obtained from the parameters of the fit:

$$\langle n_{K^0_S} \rangle = 0.62 \pm 0.02 \qquad (|\eta| < 2.5) \tag{8.3}$$

If a pure power law is used to extrapolate to p_t=0, then $\langle n_{K^0_S} \rangle$ increases by 0·01. This result is consistent with the 1985 UA1 analysis [58] which found $\langle n_{K^0_S} \rangle$ = $0{\cdot}64 \pm 0{\cdot}02_{\text{stat}} \pm 0{\cdot}04_{\text{sys}}$ for $|\eta| < 2{\cdot}5$, and with the UA5 result [59], obtained from combined $K^{\pm}$ and K^0_S data, of $\langle n_K \rangle = 0{\cdot}69 \pm 0{\cdot}06$.

The mean transverse momentum, $\langle p_t \rangle_{K^0_S}$, is evaluated from the fit parameters as described in appendix C. Using eq. C.12:

$$\langle p_t \rangle_{K^0_S} = 0.55 \pm 0.01 GeV/c \tag{8.4}$$

This value decreases by $0{\cdot}02GeV/c$ if the power law extrapolation is used. The variation of $\langle p_t \rangle_{K^0_S}$ with $\sqrt{s}$ is shown in fig. 8.5 [59,61, and references therein]. At the ISR ($\sqrt{s} < 63GeV$) the mean $\langle p_t \rangle$ slowly increases (approximately logarithmically) with $\sqrt{s}$. At the energies of the Sp$\bar{\text{p}}$S, the more rapid rise in $\langle p_t \rangle$ with $\sqrt{s}$ may be attributed to the increasing fraction of events containing high q^2 parton-parton interactions. The $\langle p_t \rangle$ for kaons is seen to be greater than the value measured for charged particles, which are predominantly pions, of $\langle p_t \rangle_{\text{ch}}$ = 0·477 ± 0·005. Fig. 8.6 shows the $\langle p_t \rangle$ for pions, kaons and protons as a function of $\sqrt{s}$.

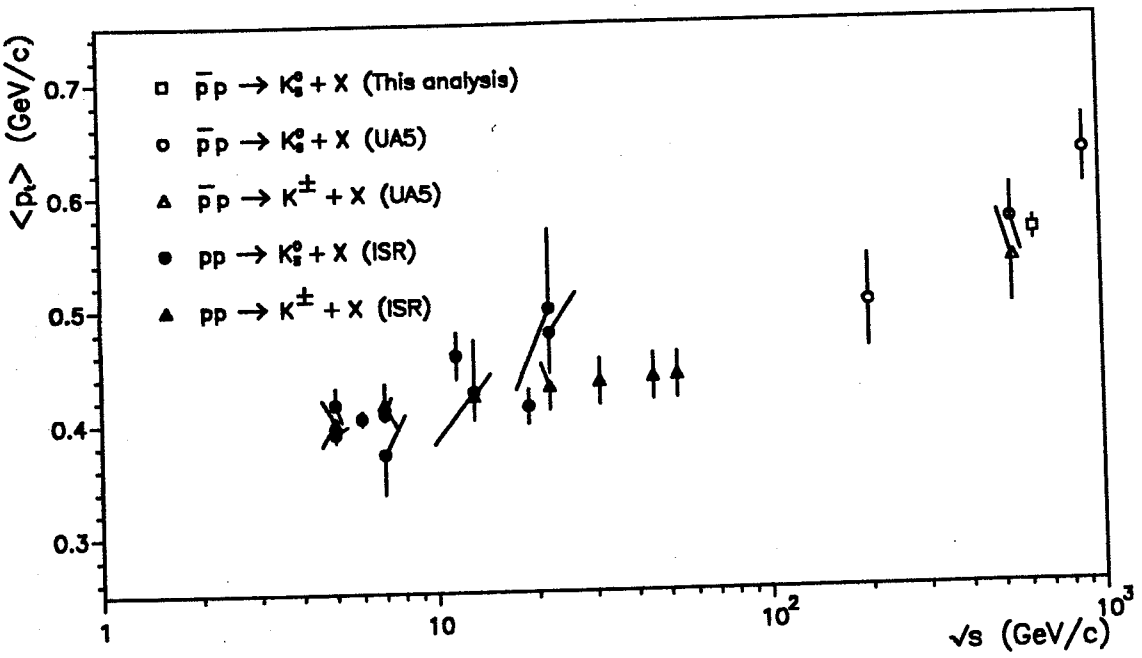

Figure 8.5: Mean p_t of kaons as a function of $\sqrt{s}$ [59,61].

At any given $\sqrt{s}$, protons have a larger $\langle p_t \rangle$ than kaons which themselves have a larger $\langle p_t \rangle$ than pions, since in resonance decays and jet fragmentation the higher mass particles take a larger fraction of the parent particle momentum.

Fig. 8.7 shows the inclusive K^0_S cross-section for three bands of charged track multiplicity. The data have been normalised to the first point of the graph for $4 < n_{ch} < 20$ to facilitate comparison of the three spectra. The solid lines show the hybrid fits to the three curves, the parameters of which are listed in table 8.3. As with the charged particle data shown in fig. 5.5, the p_t spectrum is harder (the power n is smaller) for higher multiplicity events. Quantitatively, there is an increase in the K^0_S mean p_t of about $100 MeV/c$ over the three multiplicity ranges.

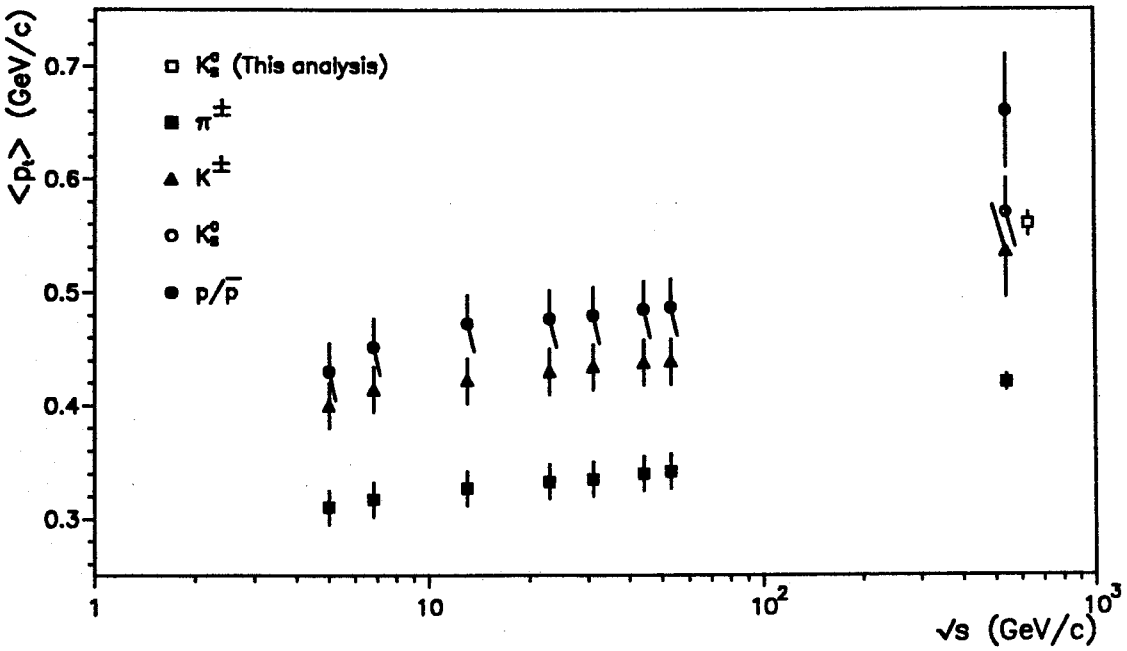

Figure 8.6: Mean p_t of pions, kaons and protons as a function of $\sqrt{s}$ [59,61].

A $(mbGeV^{-2}c^3)$	p_0 (GeV/c)	n	p_1 (GeV/c)	$\langle p_t \rangle$ (GeV/c)
5·90	2·28±0·08	11·83 ± 0·37	0·2 (fixed)	0·525±0·03
5·79	1·71±0·06	8·93 ± 0·24	0·2 (fixed)	0·585±0·02
1·27	1·38±0·09	7·42 ± 0·33	0·2 (fixed)	0·630±0·04

Table 8.3: Parameters of the hybrid fit to the inclusive K^0_S cross section for different n_{ch} intervals.

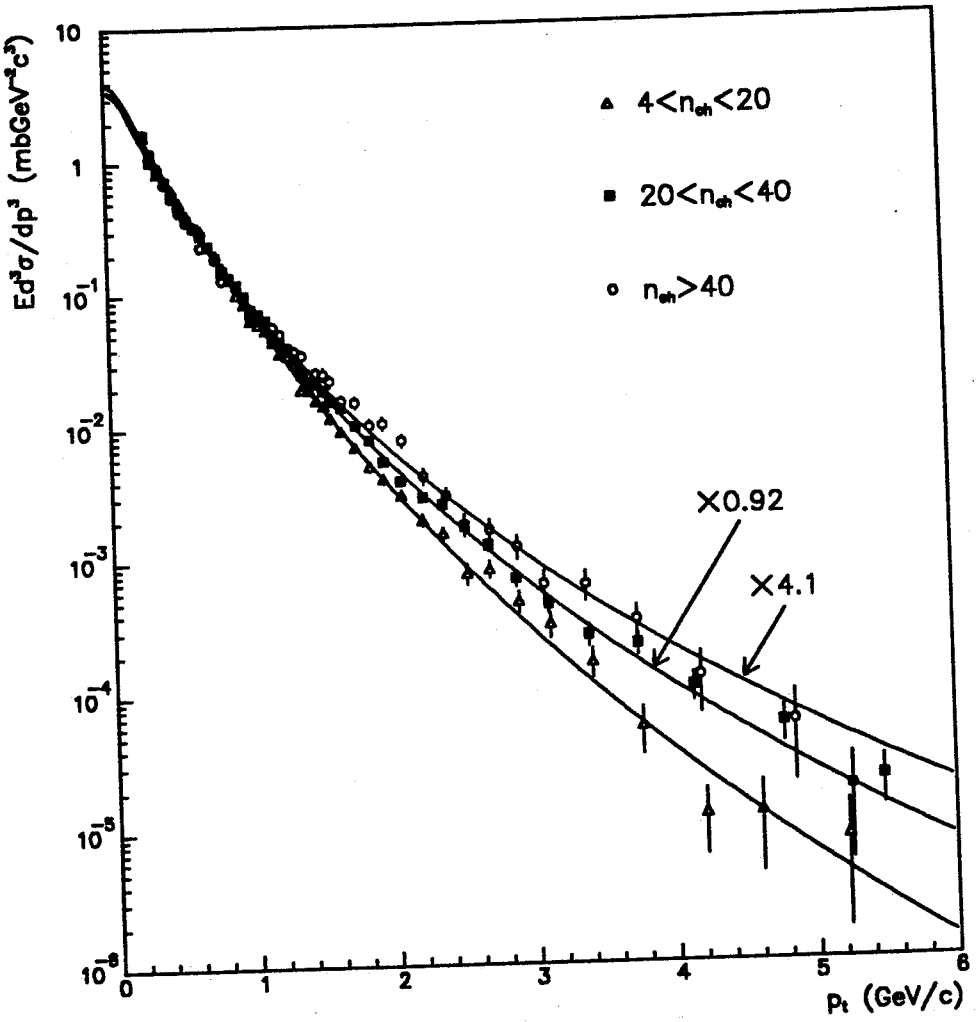

Figure 8.7: Invariant K^0_S cross-section as a function of n_{ch}.

8.3 K/π ratio and strangeness suppression

From the inclusive charged hadron and K^0_S cross-sections measured in this analysis the $K^0_S/h^\pm$ ratio [1] has been evaluated. The average $K^0_S/h^\pm$ ratio has been evaluated from the mean number of K^0_S's per event and the mean charged particle multiplicity. Using eqs. 5.5 and 8.3,

$$K^0_S/h^\pm = 0.072 \pm 0.003 \tag{8.5}$$

Systematic errors from the uncertainty in the minimum-bias cross-section cancel. Fig. 8.8 shows the variation of the $K^0_S/h^\pm$ ratio with transverse momentum, obtained by taking the ratio of the invariant K^0_S and charged particle cross-sections. The UA2 results for $K^\pm/h^\pm$ at $\sqrt{s} = 540GeV$ [60] are also shown. The UA2 $K^\pm/h^\pm$

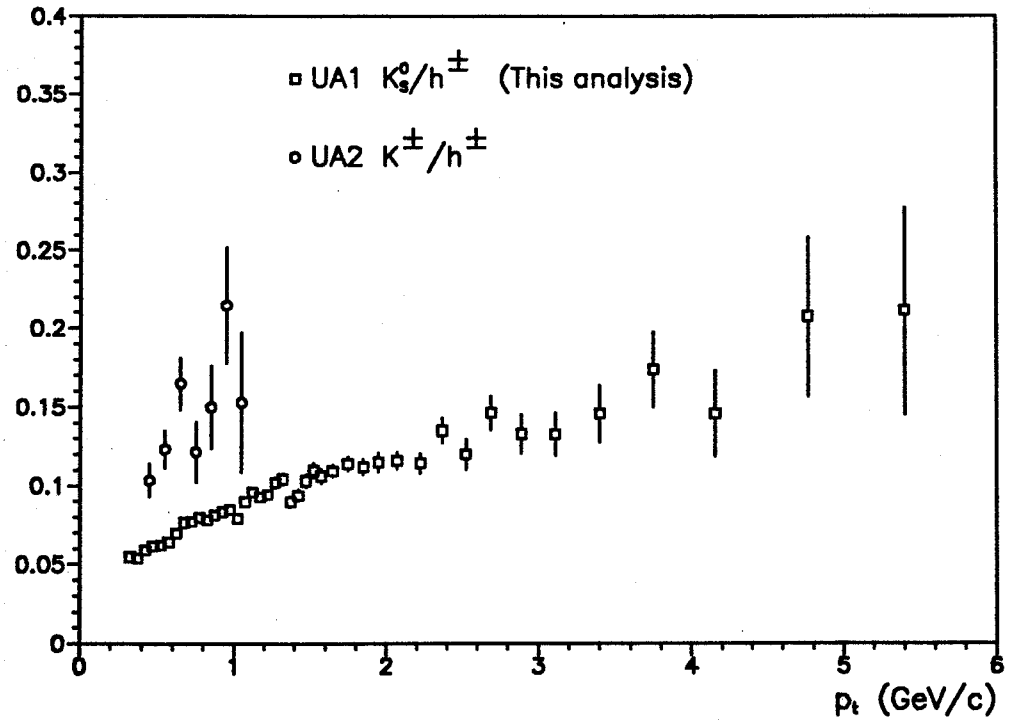

Figure 8.8: $K^0_S/h^\pm$ ratio vs. p_t (UA2 data are from ref. [60]).

ratio is systematically higher than the $K^0_S/h^\pm$ ratio measured in this analysis. This is probably due to the different trigger requirements of the two experiments and

[1] Throughout this chapter, the superscript "$\pm$" indicates the *average* cross-section for the two charges, not the *sum*. Similarly, "$p\bar{p}$" is used to denote $(p + \bar{p})/2$.

some residual pion contamination of the UA2 kaon sample as discussed above. The $K^0_S/h^\pm$ ratio at low p_t is suppressed due to the heavier mass of the strange quark.

The inclusive hadron cross-section has contributions from both baryons and mesons. The suppression in the production of strange hadrons is, therefore, more clearly seen by comparing the pion and kaon cross-sections since kaons differ from pions only in the replacement of a d quark by an s quark. The average charged pion fraction, obtained from UA2 and UA5 data at $\sqrt{s} = 546GeV$, is $\pi^\pm/h^\pm = 81{\cdot}3\pm1{\cdot}6\%$ [47]. The average $K^0_S/\pi^\pm$ ratio can be obtained by writing:

$$\frac{K^0_S}{\pi^\pm} \approx \frac{\langle n_{K^0_S}\rangle_{630}}{\langle n_{h^\pm}\rangle_{630}} \times \frac{\langle n_{h^\pm}\rangle_{540}}{\langle n_{\pi^\pm}\rangle_{540}} = 8.9 \pm 0.4\% \qquad (8.6)$$

The variation of the K/π ratio with $\sqrt{s}$ is shown in fig. 8.9 [59,61]. There is a

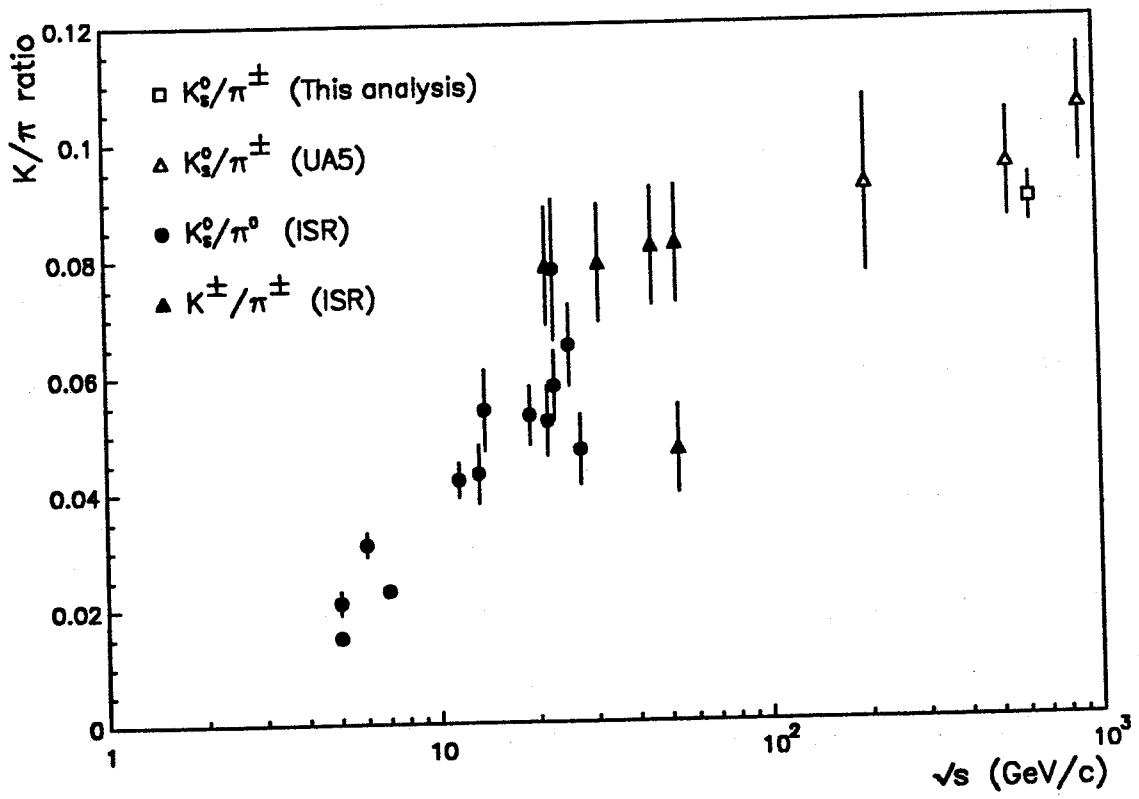

Figure 8.9: K/π ratio as a function of $\sqrt{s}$ [59,61].

strong threshold effect at low $\sqrt{s}$, due to the higher mass of the strange quark compared to u or d quarks, leading to a suppression in the production of kaons

compared to pions. At high $\sqrt{s}$ the K/π ratio seems to reach a constant value of approximately 9%. In the quark model, stable particles such as pions, kaons, nucleons, and Λ-hyperons may be produced directly from quarks in the colliding beam particles or and indirectly from the decays of short-lived resonances. The suppression, at large $\sqrt{s}$, of kaons relative to pions is due to the reduced phase-space available in resonance decays to heavier particles.

The suppression in the production of strange particles may be quantified by the parameter, λ, (defined in eq. 1.6) which measures the relative probability for producing an s quark compared to a u or d quark. The statistical quark model [10] discussed in §1.3, which includes the contributions from resonance decays, predicts the K/π ratio in terms of λ. From table 1.3:

$$K_S^0/\pi^{\pm} = \frac{12\lambda + 3\lambda^2}{31 + 12\lambda + 3\lambda^2 + \gamma(\frac{16}{3} + 4\lambda + \frac{8}{3}\lambda^2)} \tag{8.7}$$

where γ is defined as

$$\gamma = \frac{4 + 4\lambda + \lambda^2}{5 + 5\lambda + 3\lambda^2 + \lambda^3} \tag{8.8}$$

From eq. 8.6, $K_S^0/\pi^{\pm}$= 8·9 ± 0·4%, which yields a value:

$$\lambda = 0.28 \pm 0.01 \tag{8.9}$$

This is in good agreement with the value obtained by UA5 of $\lambda = 0.30 \pm 0.03 \pm 0.03$ at $\sqrt{s} = 540GeV$.

The K_S^0/π ratio has been evaluated as a function of transverse momentum up to $p_t = 6GeV/c$ by taking the ratio of the K_S^0 cross-section measured in this analysis and the combined UA2 charged and neutral pion cross-sections at $\sqrt{s} = 540GeV$. The charged pion cross-section has been measured for $0.4 < p_t < 1.4GeV/c$ using time-of-flight information to identify the pions [60]. The neutral pion cross-section [62] was obtained by reconstructing the decay: $\pi^0 \rightarrow \gamma\gamma$, over the higher p_t range, $1.5 < p_t < 4.5GeV/c$. The UA2 inclusive pion cross-sections are shown in fig. 8.10. The binning of the UA2 data is inconsistent with the binning of K_S^0 data from this analysis. A fit of the hybrid form (eq. 5.3) was therefore made to the

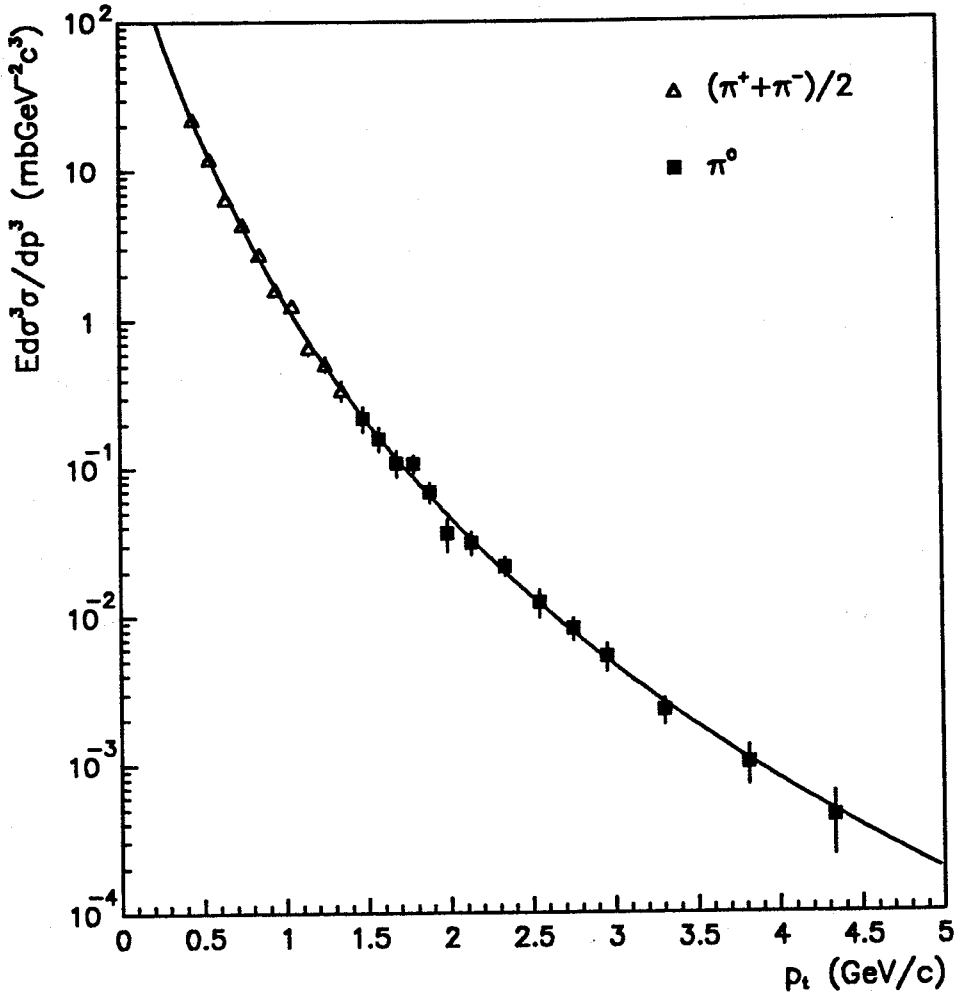

Figure 8.10: UA2 charged and neutral pion inclusive cross-sections, from refs. [60] and [62].

charged and neutral pion cross-sections and the result used to determine the pion cross-section at an arbitrary p_t. There is a 4% error in the measurement of the p_t of the π^0's so the p_t values of the π^0 data points were allowed to vary by a common factor in the fit, *i.e.* $p_t \rightarrow f p_t$. A value of f =0·98 was obtained. The result of the fit is shown by the solid line in fig. 8.10. In order to minimise the effect of the different centre-of-mass energies and to cancel the systematic errors in the luminosity calibrations of the two experiments the K^0_S and pion cross-sections were normalised to the appropriate inclusive hadron cross-sections, *i.e.*

$$\frac{K^0_S}{\pi} = \left[\frac{f(K^0_S)}{f(h^\pm)}\right]_{630} \times \left[\frac{f(h^\pm)_{\mathrm{UA2}}}{f(\pi)_{\mathrm{UA2}}}\right]_{540} \tag{8.10}$$

where $f(p_t)$ is the inclusive invariant cross-section, $Ed^3\sigma/dp^3$, for the production of the appropriate particle type. Unfortunately, UA2 has only measured the inclusive charged hadron cross-section up to $p_t = 2GeV/c$. Extrapolation of a fit to this data to $p_t = 6GeV$ introduces a large systematic uncertainty. UA1 has measured the inclusive charged hadron cross-section at $\sqrt{s} = 540GeV/c$ to $p_t = 10GeV/c$ [63]. A fit to this UA1 data, normalised to the UA2 total charged hadron cross-section, has therefore been used. Thus, the K^0_S/π ratio, as a function of p_t was calculated using the following expression:

$$\frac{K^0_S}{\pi} = \left[\frac{f(K^0_S)}{f(h^\pm)}\right]_{630} \times \left[\frac{f(h^\pm)_{\mathrm{UA1}}}{f(\pi)_{\mathrm{UA2}}}\right]_{540} \times \left[\frac{\sigma_{\mathrm{tot}}(h^\pm)_{\mathrm{UA2}}}{\sigma_{\mathrm{tot}}(h^\pm)_{\mathrm{UA1}}}\right]_{540} \tag{8.11}$$

Fig. 8.11 shows the K^0_S/π ratio, as a function of p_t. Also shown are results from UA2 at $\sqrt{s} = 540GeV$ [60] and from UA5 at $\sqrt{s} = 546GeV/c$ [59]. At low p_t the higher mass of the s quark compared to u or d quarks suppresses the production of kaons compared to pions. For transverse momenta greater than about $2GeV/c$ the K^0_S/π ratio becomes flatter as the strange quark mass becomes insignificant. This threshold effect may be removed by plotting the K/π ratio as a function of transverse mass, $m_t = \sqrt{p_t^2 + m^2}$ (m is the kaon or pion mass) as shown in fig. 8.12. The K/π ratio as a function of m_t is approximately flat.

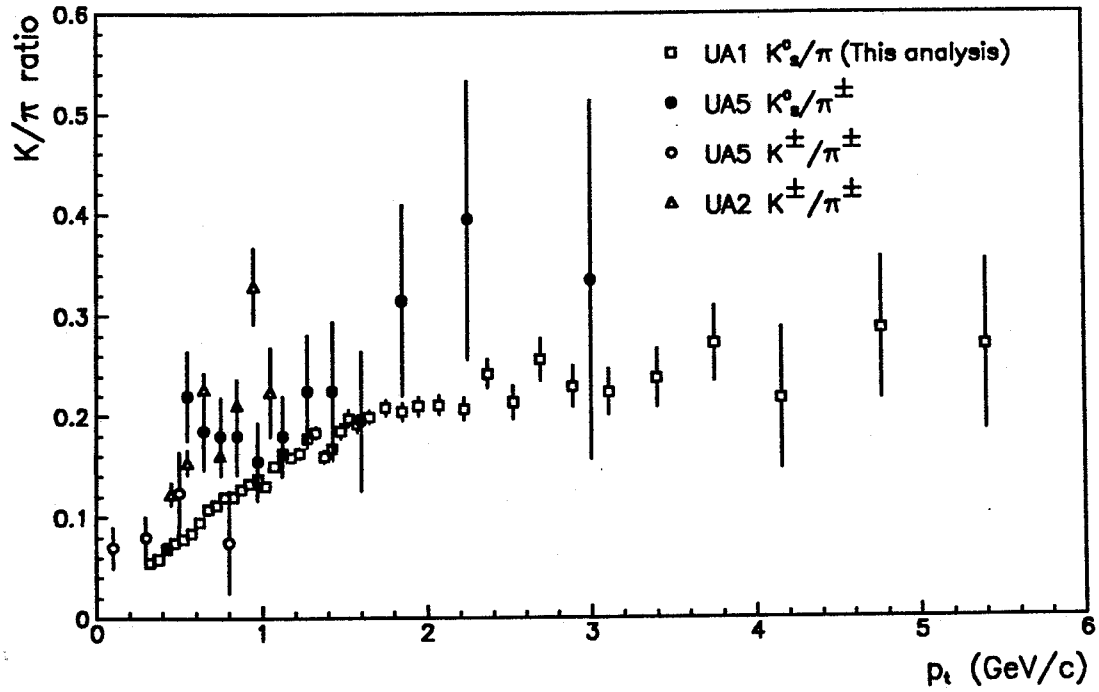

Figure 8.11: K/π ratio as a function of p_t compared with data from UA5 [59] and UA2 [60].

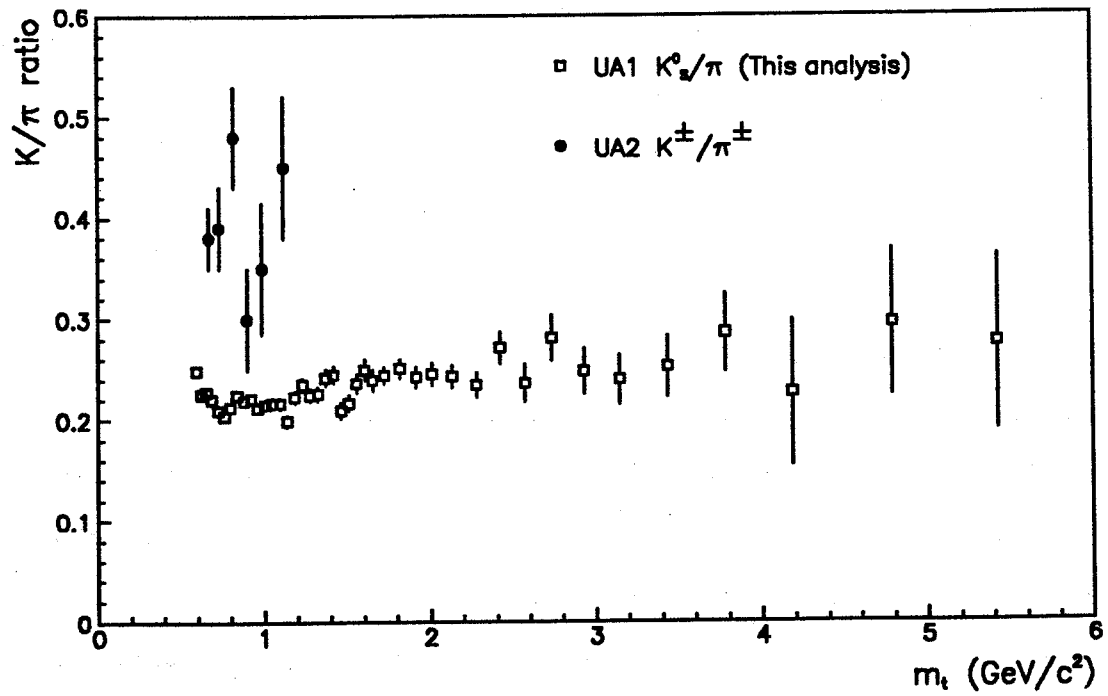

Figure 8.12: K/π ratio as a function of m_t (UA2 data is from ref. [60]).

9. Conclusions

The analysis presented herein is based on approximately two million minimum-bias events collected by the UA1 experiment during the 1987 Sp$\bar{p}$S collider run. The very high statistics of this sample has enabled a detailed and accurate study of hadron production to be made. The results are based on data from the central drift chamber and great care has been taken to eliminate detector-dependent effects.

The inclusive charged particle cross-section has been measured up to a transverse momentum of $15 GeV/c$. By extrapolating the p_t spectrum to $p_t = 0$, the mean charged particle multiplicity, and the mean transverse momentum have been evaluated. Comparison of these data with lower energy results shows that the mean multiplicity increases logarithmically with the centre-of-mass energy. The charged multiplicity distribution has been shown to be consistent with the KNO scaling hypothesis. The mean charged particle transverse momentum is strongly correlated with the multiplicity due to a significant number of events with an underlying hard scatter.

A search for secondary vertices arising from the decay: $K^0_S \rightarrow \pi^+\pi^-$ was made. The large background from photon conversions, random track combinations and Λ-hyperon decays was drastically reduced by exploiting the differences in their decay topologies compared to kaons. A sample of 91 000 K^0_S decays with a purity of 86% was obtained. The only previously published results on K^0_S production at the energies of the Sp$\bar{p}$S collider come from the UA5 collaboration and are based on just 171 K^0_S decays (in the same rapidity range of $|\eta| < 2{\cdot}5$). The efficiency for K^0_S reconstruction was evaluated as a function of p_t, η and ϕ by mixing simulated

K^0_S decays with real events.

The inclusive cross-section for K^0_S production has been evaluated up to $p_t = 6GeV/c$. The mean number of K^0_S mesons produced per event was found to be: $\langle n_{K^0_S} \rangle = 0.62 \pm 0.02$ ($|\eta| < 2.5$). The mean K^0_S transverse momentum measured is $\langle p_t \rangle_{K^0_S} = 0.55 \pm 0.01 GeV/c$. The more rapid increase in $\langle p_t \rangle_{K^0_S}$ at the Sp$\bar{\text{p}}$S energies compared with data at lower $\sqrt{s}$ and the hardening of the K^0_S p_t spectrum with increasing charged multiplicity is attributed to a significant fraction of events containing jets.

The ratio of the K^0_S cross-section from this analysis and the charged and neutral pion cross-sections of UA2 has been calculated. Using a statisitical quark model, the production of strange quarks compared to either u or d quarks is found to be suppressed by an average factor of λ=0·28 ± 0·01.

A. Central Detector Acceptance

A detailed knowledge of the charged track reconstruction efficiency (or acceptance) of the CD is necessary before any physical conclusions may be drawn. The acceptance is a function of p_t, η, ϕ and the charge of the particle. Contributions to the CD acceptance come from the geometry of the chamber, its performance and the efficiency of the track-finding algorithm. It is important to re-evaluate the acceptance periodically as the operating conditions of the chamber change. While the track-finding techniques were largely developed using Monte-Carlo generated tracks [34], evaluation of the acceptance using simulated data will give over-optimistic values. This is because it is impossible to model, with sufficient local detail, the behavior of the chamber — in particular the two-track resolution, the angular dependence of the pulse and the systematic errors. The CD acceptance is therefore evaluated using real minimum-bias data [64,65] from the appropriate data-taking period.

Figures A.1 to A.4 shows the charged track distribution for positive and negative particles for two p_t intervals. Exploiting the z symmetry of the CD, the data from the region $90° < |\phi| < 180°$ have been folded with those within $0° < |\phi| < 90°$ in order to improve the statistics. A lower statistics study showed that the acceptance was symmetric within errors and unaffected by the small correction to the dip angle described in section 4.4. Particles in the region around $\eta = 0$ and $\phi = 0$ are moving in the direction of the field. Here the acceptance is poor since the the tracks have few points and very little curvature. The loss of tracks at large

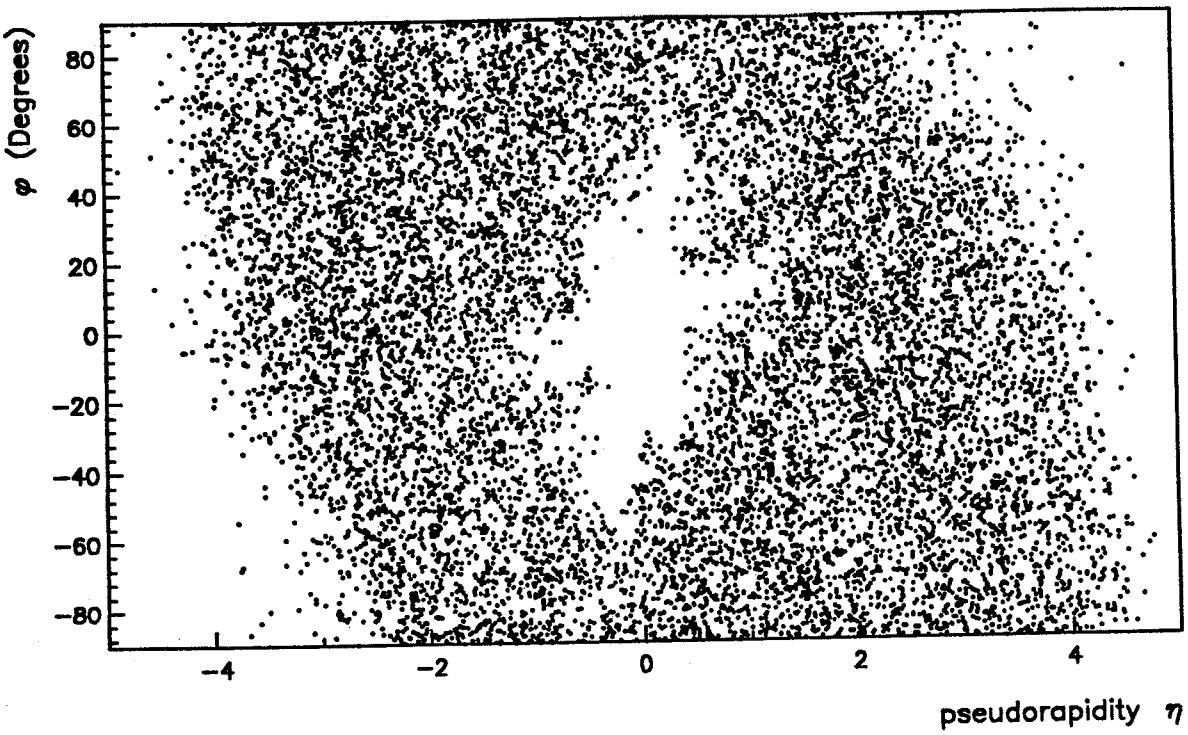

Figure A.1: Positive charged track distribution ($0{\cdot}2 < p_t < 0{\cdot}3\ GeV/c$)

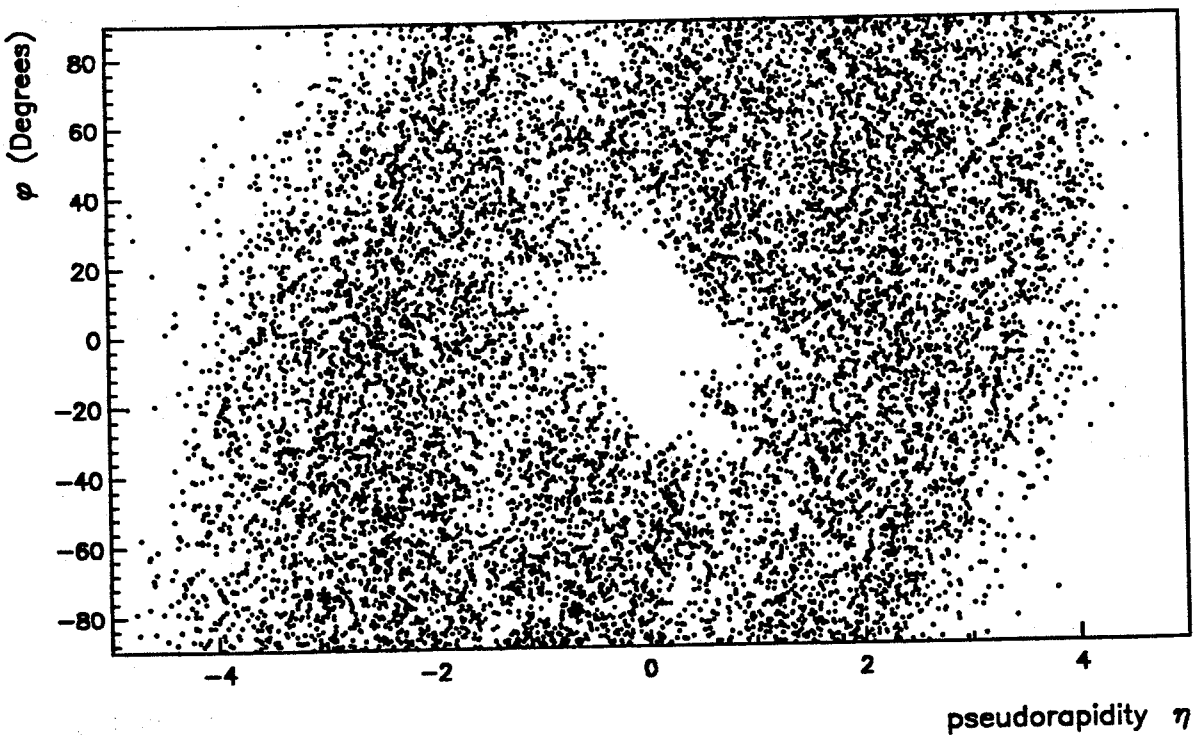

Figure A.2: Negative charged track distribution ($0{\cdot}2 < p_t < 0{\cdot}3\ GeV/c$)

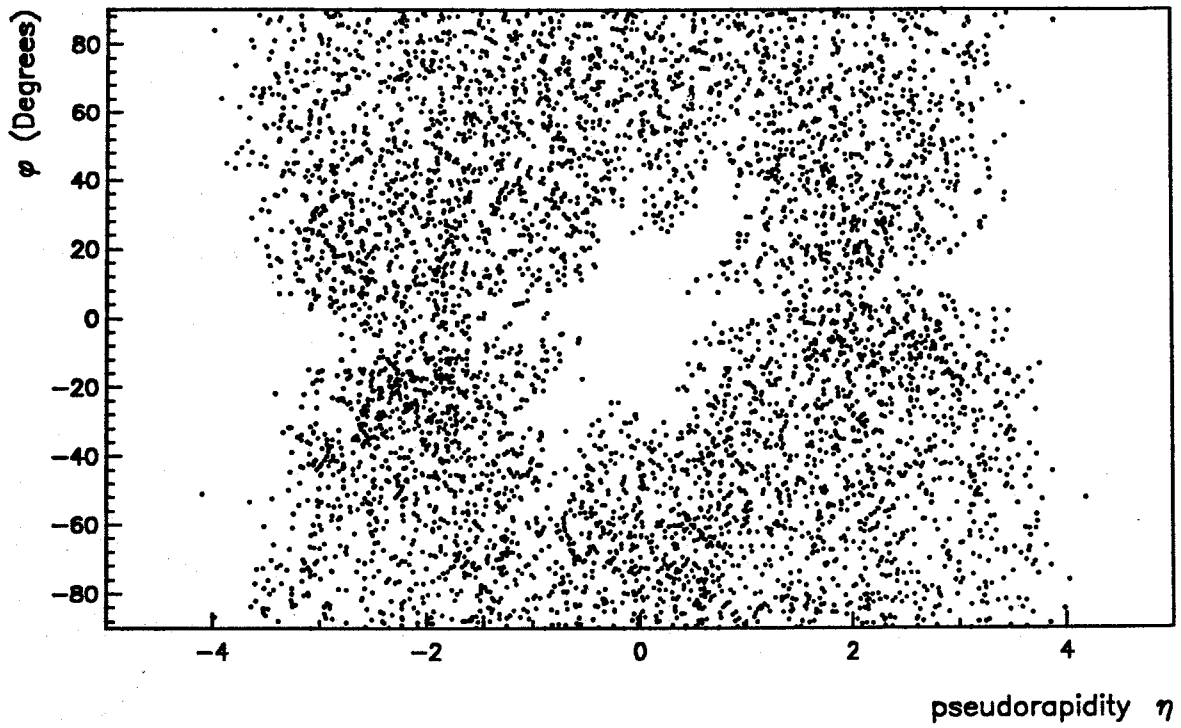

Figure A.3: Positive charged track distribution ($1{\cdot}0 < p_t < \infty\ GeV/c$)

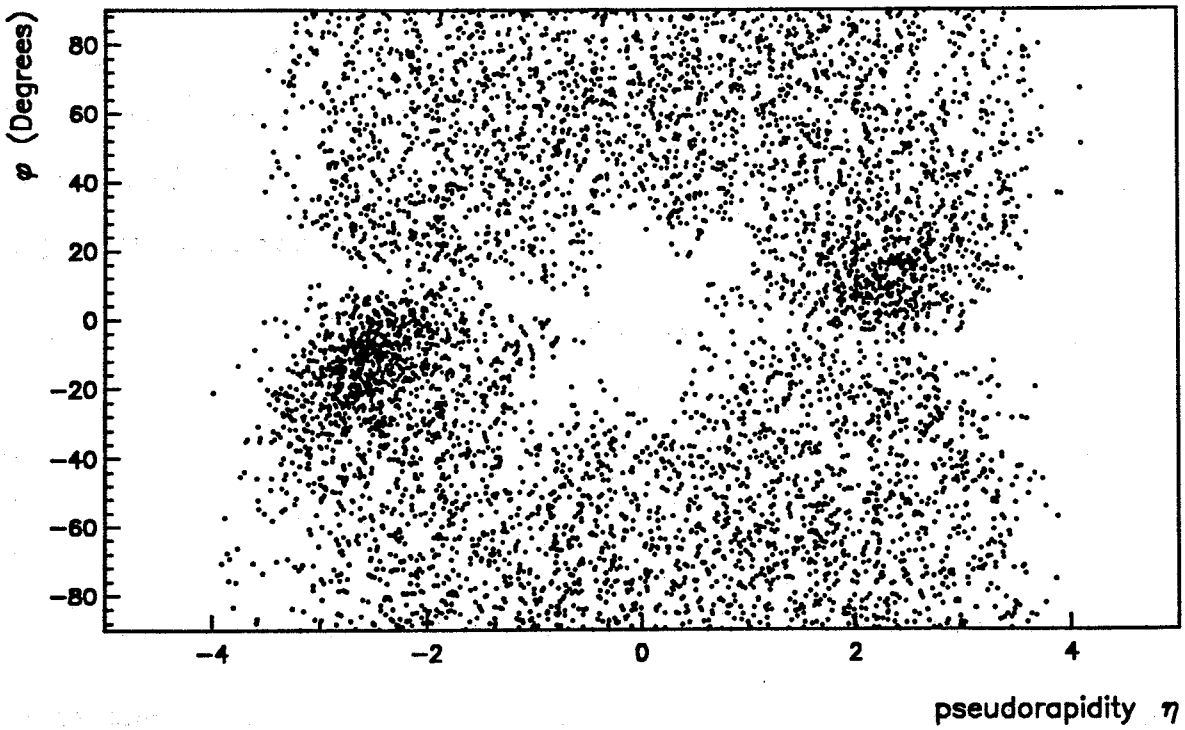

Figure A.4: Negative charged track distribution ($1{\cdot}0 < p_t < \infty\ GeV/c$)

rapidities is charge-dependent since the particles are either deflected into or out of the beam-pipe by the magnetic field. This results in a loss of positive particles for η and ϕ large and of the same sign, and a loss of negative particles for η and ϕ large and of the opposite sign. Tracks with a large curvature are most affected since the starting point of a track is defined as the point of closest approach to the horizontal plane containing the beam. Hence, if a track curves through this plane it is split into two separate tracks each having fewer points and poor vertex association. The gap between the chambers ($|\phi| \sim 0°$and all rapidity) is also seen, particularly at high p_t.

The CD acceptance is calculated as follows. For positive and negative particles separately, phase-space is divided into bins of equal size in η ($\Delta\eta = 0{\cdot}25$) and ϕ ($\Delta\phi = 11{\cdot}25°$), and of non-equal size in p_t ($0{\cdot}15$–$0{\cdot}2$–$0{\cdot}3$–$0{\cdot}5$–$1{\cdot}0$–∞ GeV/c). The variable binning in p_t maintains sufficient statistics in the high p_t region, and since the tracks become straighter with increasing p_t, the acceptance calculation does not suffer as a result. A sample of 10^5 events was used to calculate the acceptance.

The acceptance is calculated assuming that the η and ϕ distributions are flat which is a reasonable assumption for the range, η <2·5, used for this analysis. For each charge and p_t, the number of tracks satisfying some minimal standard track quality cuts (table A.1) is evaluated for each bin in $\eta\phi$ space. The resulting

Projected length, l_{xy}	$> 40cm$
Number of points in xy fit, n_{pts}	> 20
Goodness of xy-fit, χ^2_{xy}	< 6.0
Goodness of z-fit, χ^2_z	< 9.0

Table A.1: Track-quality cuts

population distribution is formed, as shown in fig. A.5, where the horizontal axis is the number of tracks in the $\eta\phi$ bin and the vertical axis is the number of $\eta\phi$ bins which contain this number of tracks. The distribution may be described by

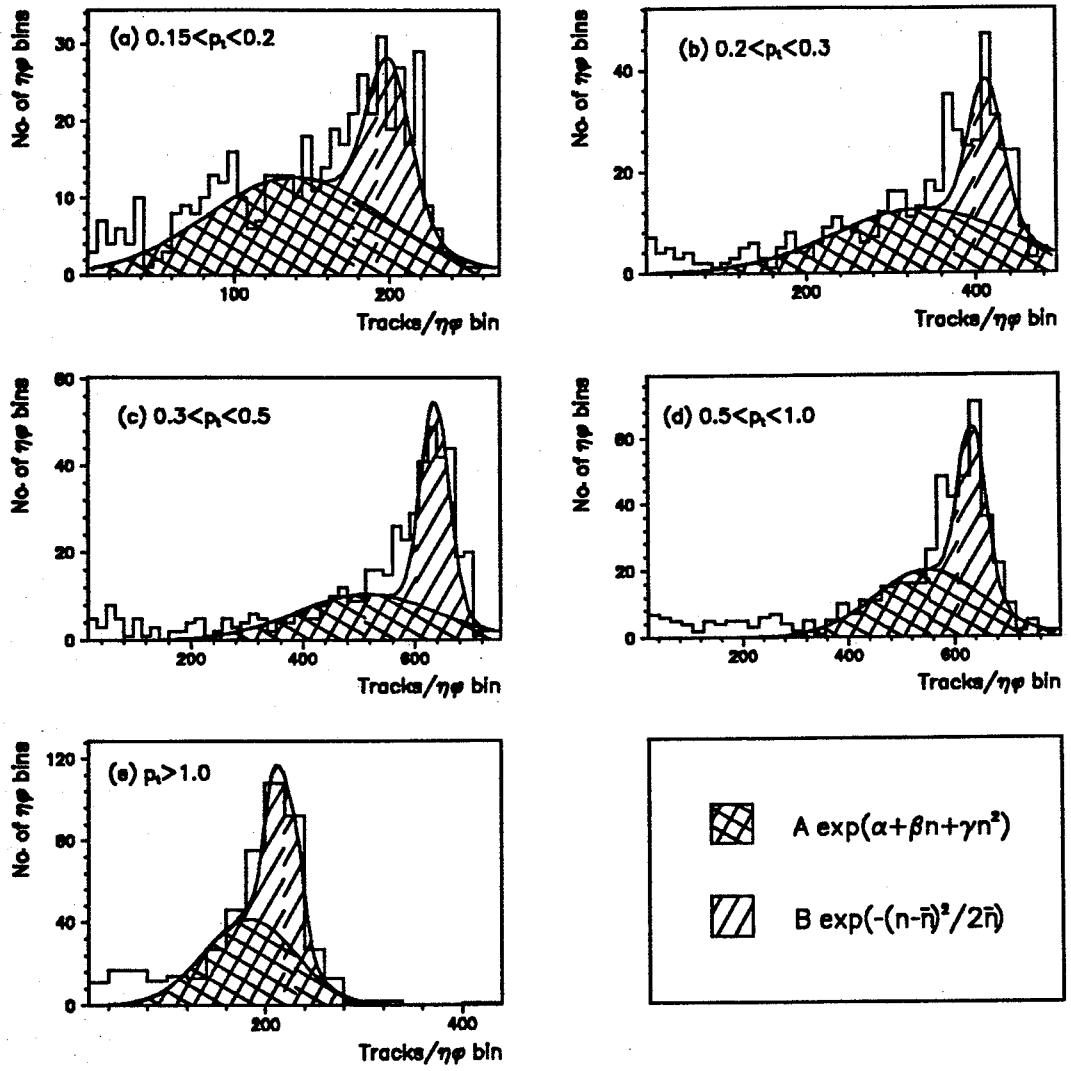

Figure A.5: Track population distributions vs. p_t

a gaussian centred at $\bar{n}$ with $\sigma = \sqrt{\bar{n}}$ corresponding to bins of $\sim 100\%$ efficiency, [1] plus a lower tail coming from the areas of poor acceptance. To improve the determination of $\bar{n}$, positive and negative tracks have been included in the same plot. The rejection of tracks by the track quality cuts is incorporated in the acceptance and does not bias the result provided no genuine tracks are rejected in the good regions of the CD. A fit of the form:

$$f(n) = Ae^{\alpha+\beta n+\gamma n^2} + Be^{-(n-\bar{n})^2/2\bar{n}} \tag{A.1}$$

[1]The track-finding efficiency is in fact 96% [34], approximately independent of p_t, η, ϕ and multiplicity. The data have been corrected accordingly (see chapter 5).

is made to the distribution. The first term describes empirically the poorer regions of the CD and the second those regions with ~100% efficiency and a gaussian measurement error. To avoid having $\mathcal{A} > 1$ for any region, a cut-off $n_{\rm cut}$ is defined according to:

$$\int_0^{n_{\rm cut}} Be^{-(n-\bar{n})^2/2\bar{n}} = \int_{n_{\rm cut}}^{\infty} Ae^{\alpha+\beta n+\gamma n^2} \qquad \text{(A.2)}$$

The gaussian component below $n_{\rm cut}$ is therefore balanced by the polynomial component above $n_{\rm cut}$, so all bins with $n \geq n_{\rm cut}$ may be assumed to have 100% acceptance without introducing a systematic bias. The acceptance for each bin in η-ϕ is then given by:

$$\mathcal{A} = \begin{cases} 1.0, & \text{if } n \geq n_{\rm cut} \\ n/\bar{n}, & \text{if } n < n_{\rm cut} \end{cases} \qquad \text{(A.3)}$$

Although $\bar{n}$ is determined by combining the data from positive and negative tracks, the acceptance is calculated separately for each. Acceptance-corrected physical distributions are then obtained by weighting each track by a factor $1/\mathcal{A}$ interpolating in $1/p_t$.

The corrected number of tracks is subject to the statistical fluctuations as $\mathcal{A} \rightarrow 0$, so if the acceptance for any bin was less than a certain threshold value, $\mathcal{A}_{\rm min}$, then it was set to zero and all other bins in ϕ with the same η and p_t were scaled by

$$f(p_t, \eta) = \frac{\text{No. of bins in } \phi \text{ with } \mathcal{A} > 0}{\text{No. of bins in } \phi \text{ with } \mathcal{A} > \mathcal{A}_{\rm min}} \qquad \text{(A.4)}$$

While this does not affect the p_t and η distributions, the ϕ distribution becomes non-physical. In this analysis, a value $\mathcal{A}_{\rm min}$=10% was used.

A fiducial cut in projected Φ was necessary due to noise in the CD close to the beam (section 4.3). This was implemented by setting the acceptance of all the η-ϕ bins falling within the region of the cut to zero (fig. 4.5). The other bins in ϕ for the same η and p_t were then re-scaled in the same way as described above.

The systematic error in the differential charged particle cross-section, integrating over ϕ, η and taking both positive and negative charged particles, is less than 0·3% for each of the five p_t ranges considered.

B. Charged track distribution in Φ and λ.

In this appendix, the expected form of charged particle distribution, as a function of the projected angle Φ and the dip angle λ, is evaluated assuming a flat distribution in azimuthal angle ϕ and pseudo-rapidity η, *i.e.*

$$\frac{d^2f}{d\phi d\eta} = A \tag{B.1}$$

where A is constant. Making a Jacobian transformation of variables, this may be written

$$\frac{d^2f}{d\Phi d\lambda} = \frac{d^2f}{d\phi d\eta}\frac{\partial(\phi,\eta)}{\partial(\Phi,\lambda)} = A\begin{vmatrix} \frac{\partial\phi}{\partial\Phi} & \frac{\partial\phi}{\partial\lambda} \\ \frac{\partial\eta}{\partial\Phi} & \frac{\partial\eta}{\partial\lambda} \end{vmatrix} \tag{B.2}$$

$$= A\left(\frac{\partial\phi}{\partial\Phi}\frac{\partial\eta}{\partial\lambda} - \frac{\partial\phi}{\partial\lambda}\frac{\partial\eta}{\partial\Phi}\right) \tag{B.3}$$

From fig.B.1, ϕ and $\theta = \theta(\eta)$ may be written in terms of Φ and λ:

$$\tan\phi = \frac{y}{z} = \frac{y}{t}\frac{t}{r}\frac{r}{z} = \frac{\sin\Phi\cos\lambda}{\sin\lambda} \tag{B.4}$$

$$\cos\theta = \frac{x}{r} = \frac{x}{t}\frac{t}{r} = \cos\Phi\cos\lambda \tag{B.5}$$

The individual partial derivatives are determined by differentiation of eqs. B.4 and B.5:

$$\frac{\partial\phi}{\partial\Phi} = \frac{\cos\lambda\cos\Phi}{\sin\lambda}\left[1+\left(\frac{\sin\Phi\cos\lambda}{\sin\lambda}\right)^2\right]^{-1} \tag{B.6}$$

$$\frac{\partial\phi}{\partial\lambda} = -\frac{\sin\Phi}{\sin^2\lambda}\left[1+\left(\frac{\sin\Phi\cos\lambda}{\sin\lambda}\right)^2\right]^{-1} \tag{B.7}$$

and, using the definition of pseudo-rapidity, $\eta = -\ln(\tan(\theta/2))$:

$$\frac{\partial\eta}{\partial\Phi} = \frac{\partial\eta}{\partial\theta}\frac{\partial\theta}{\partial\Phi} = \left(\frac{-1}{\sin\theta}\right)\left(\frac{\sin\Phi\cos\lambda}{\sin\theta}\right) \tag{B.8}$$

$$= -\sin\Phi\cos\lambda\left(1-\cos^2\Phi\cos^2\lambda\right)^{-1} \tag{B.9}$$

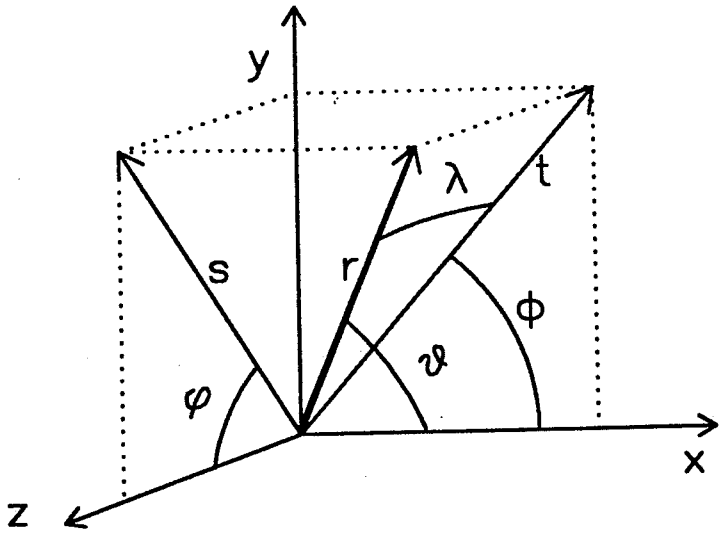

Figure B.1: Charged track distribution geometry.

$$\frac{\partial \eta}{\partial \lambda} = \frac{\partial \eta}{\partial \theta}\frac{\partial \theta}{\partial \lambda} = \left(\frac{-1}{\sin\theta}\right)\left(\frac{\cos\Phi\sin\lambda}{\sin\theta}\right) \tag{B.10}$$

$$= -\cos\Phi\sin\lambda\left(1-\cos^2\Phi\cos^2\lambda\right)^{-1} \tag{B.11}$$

Substituting eqs.B.6 B.7, B.9 and B.11 in eq.B.3, yields after some reduction:

$$f(\Phi,\lambda) = \frac{A\cos\lambda}{1-\cos^2\lambda\cos^2\Phi} \tag{B.12}$$

C. Fitting the p_t spectra

As discussed in chapter 1 the inclusive charged hadron cross-section is predicted to behave as an exponential in transverse mass, $m_t = \sqrt{p_t^2 + m_\pi^2}$, at low p_t and as a power law at higher p_t, as given by eq. 5.3. In this appendix the procedure for extracting the total cross-section and mean transverse momentum from the hybrid fit parameters is outlined.

The invariant cross-section has been fitted with a hybrid function:

$$E\frac{d^3\sigma}{dp^3} = \begin{cases} f(p_t) = Be^{-\beta m_t} & ;\ \text{if } p_t < p_1 \\ g(p_t) = A\left(\frac{p_0}{p_t+p_0}\right)^n & ;\ \text{if } p_t \geq p_1 \end{cases} \tag{C.1}$$

The parameters B and β are constrained by requiring continuity of the functions and their first derivatives at the crossover point $p_t = p_1$. The first constraint, $f(p_1) = g(p_1)$, gives

$$Be^{-\beta(p_1^2+m_\pi^2)^{1/2}} = A\left(\frac{p_0}{p_0+p_1}\right)^n \tag{C.2}$$

The second constraint, $df(p_1)/dp_t = dg(p_1)/dp_t$, results in

$$B\beta p_t \frac{e^{-\beta(p_1^2+m_\pi^2)^{1/2}}}{(p_1^2+m_\pi^2)^{1/2}} = \frac{An}{p_0}\left(\frac{p_0}{p_0+p_1}\right)^{n+1} \tag{C.3}$$

These are then solved to yield expressions in terms of A, n, p_0 and p_1 for B

$$B = A\left(\frac{p_0}{p_0+p_1}\right)^n e^{\beta(p_1^2+m_\pi^2)^{1/2}} \tag{C.4}$$

and for the exponential factor, β

$$\beta = \left(\frac{n}{p_0+p_1}\right)\frac{(p_1^2+m_\pi^2)^{1/2}}{p_1} \tag{C.5}$$

For the fit, only A, n and p_0 are allowed to vary and, for a given p_1, the parameters B and β are given by eqs. C.4 and C.5.

C.1 Total cross-section and mean multiplicity

The total inclusive cross-section, σ_t, is given by the integral:

$$\sigma_t = \int_0^\infty \frac{\partial\sigma}{\partial p_t} dp_t \approx 2\pi\Delta\eta \int_0^\infty p_t \Big(E\frac{d^3\sigma}{dp^3}\Big) dp_t \tag{C.6}$$

where $Ed^3\sigma/dp^3$ is given by eq. C.1. This expression is evaluated analytically from the fit parameters, A, n and p_0, automatically including the extrapolation to $p_t = 0$ necessary as a result of the p_t <0·15GeV/c. The integral for the exponential function, $f(p_t)$, over the range $[p_{t,1}, p_{t,2}]$ is

$$I_f\Big|_{p_{t,1}}^{p_{t,2}} = 2\pi\Delta\eta\Big[\frac{-B}{\beta^2}e^{-\beta m_t}(1+\beta m_t)\Big]_{p_{t,1}}^{p_{t,2}} \tag{C.7}$$

where $p_{t,1} < p_{t,2} < p_1$. For the power law function, $g(p_t)$, the integral (valid for $p_1 < p_{t,1} < p_{t,2}$) is

$$I_g\Big|_{p_{t,1}}^{p_{t,2}} = 2\pi\Delta\eta\Big[C\Big(\frac{p_0}{p_0+p_t}\Big)^n \frac{(p_0+p_t)}{(n-2)(n-1)}\Big((1-n)p_t - p_0\Big)\Big]_{p_{t,1}}^{p_{t,2}} \tag{C.8}$$

The total cross-section is then given by the sum of I_f and I_g for the full p_t range, *i.e.*

$$\sigma_t = I_f\Big|_0^{p_1} + I_g\Big|_{p_1}^{\infty} \tag{C.9}$$

This analytic form has been verified by a numerical calculation of the integral. The mean charged track multiplicity in minimum-bias events is then simply

$$\langle n_{ch}\rangle = \frac{\sigma_t}{\sigma_{\rm MB}} \tag{C.10}$$

where $\sigma_{\rm MB}$, the minimum-bias trigger cross-section, is given by eq. 2.4.

C.2 Mean p_t

The mean transverse momentum, $\langle p_t\rangle$, is calculated from the fit parameters in a similar way to the total cross-section:

$$\langle p_t\rangle = \frac{1}{\sigma_t}\int_0^\infty p_t \frac{\partial\sigma}{\partial p_t} dp_t \approx \frac{2\pi\Delta\eta}{\sigma_t}\int_0^\infty p_t^2 \Big(E\frac{d^3\sigma}{dp^3}\Big) dp_t \tag{C.11}$$

where the invariant cross-section is given by eq. C.1. The two resulting integrals do not have trivial analytic solutions and so have been evaluated numerically for given values of the fit parameters. In the limit $\delta p_t \rightarrow 0$, eq. C.11 may be written

$$\langle p_t \rangle = \sum_{p_t} \left[\frac{2\pi\Delta\eta}{\sigma_t} p_t^2 \left(E\frac{d^3\sigma}{dp^3} \right) \delta p_t \right] \qquad \text{(C.12)}$$

which gives $\langle p_t \rangle$ to arbitrary accuracy.

D. Effect of the CD resolution on the p_t-spectrum

D.1 Evaluation of the p_t resolution

In the drift-plane the spatial resolution is determined by the time-spread of the arrival of the first electrons. By studying the residuals of many fitted tracks, the single hit measurement error is found to be distributed according to a gaussian of width $\sigma_{xy} \approx 250\mu m$. Similarly, in the charge division coordinate $\sigma_z \approx 1.7\% \times l_{wire}$. For a track of length l and sagitta s, subtending an angle 2α at the origin of the track circle, radius R, the sagitta may be written as

$$s = R(1 - cos\alpha) \tag{D.1}$$

Expanding in terms of $\alpha = l/2R$ gives

$$\frac{1}{R} = \frac{8s}{l^2}\left(1 + \frac{1}{2}\left(\frac{l}{R}\right)^2 + \cdots\right) \tag{D.2}$$

The error on the sagitta is gaussian and dominates since the track length is well measured, therefore $1/p \propto 1/R$ has, to first order, a gaussian error. The track length is not constant, depending mainly on the geometry of the chamber, however it is found that $\sigma_{1/p}$ is roughly constant. Hence, using the relation $p_t = p\sqrt{1 - \cos^2\lambda\cos^2\Phi}$, by standard propagation of errors:

$$\frac{\sigma^2_{p_t}}{p_t^2} = \frac{\sigma^2_p}{p^2} + \left(\frac{\cos\lambda \sin\lambda \cos^2\Phi}{1-\cos^2\lambda\cos^2\Phi}\right)^2 \sigma^2_\lambda + \left(\frac{\cos\Phi \sin\Phi \cos^2\lambda}{1-\cos^2\Phi\cos^2\lambda}\right)^2 \sigma^2_\Phi$$

$$+\frac{2}{p}\left(\frac{\cos\lambda \sin\lambda \cos^2\Phi}{1-\cos^2\Phi\cos^2\lambda}\right)\sigma^2_{p,\lambda} + \frac{2}{p}\left(\frac{\cos\Phi \sin\Phi \cos^2\lambda}{1-\cos^2\Phi\cos^2\lambda}\right)\sigma^2_{p,\Phi} \qquad \text{(D.3)}$$

There is no correlation in the λ and Φ measurements. The momentum may be expressed in terms of the projected momentum, p_{xy}, and the dip angle, λ, since $p_{xy} = p\cos\lambda$. The correlation term, $\sigma_{p,\lambda}$, then becomes

$$\sigma^2_{p,\lambda} = \langle \delta p \delta\lambda \rangle = (p\tan\lambda)\sigma^2_\lambda \qquad \text{(D.4)}$$

The errors in the measured track parameters, namely $\sigma^2_{1/p}$, σ^2_λ, σ^2_Φ and $\sigma_{p,\Phi}$, are evaluated for each reconstructed track. Using eq. D.3 σ_{1/p_t} may be obtained (fig. D.1). The dominance of the momentum error is apparent in the flatness of this

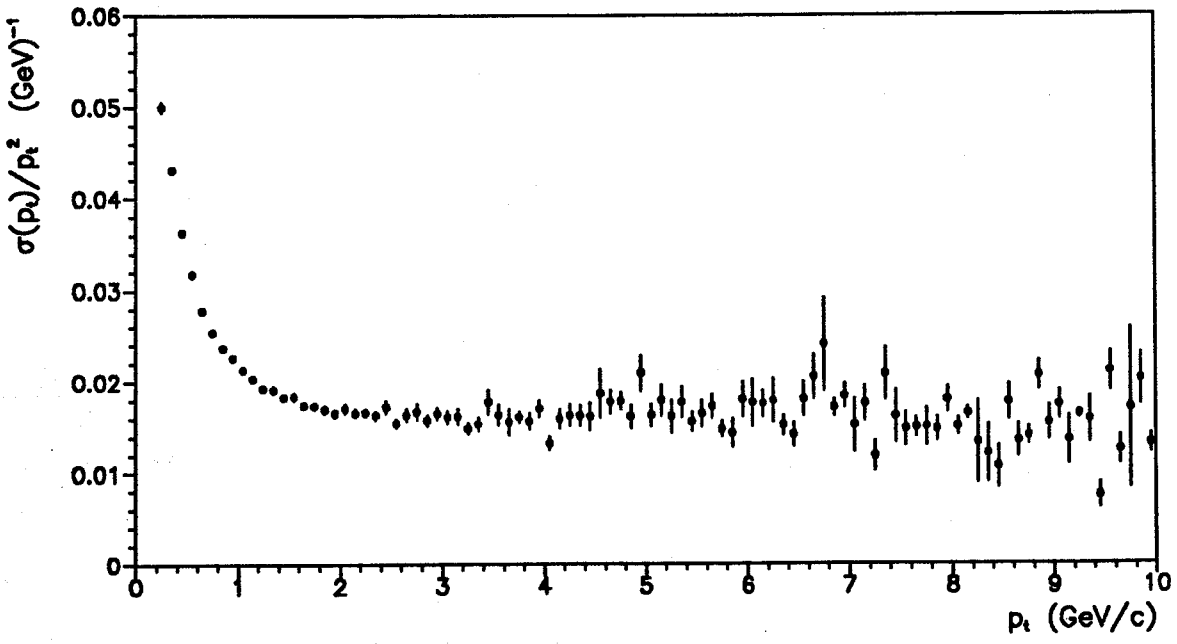

Figure D.1: Inclusive charged track p_t resolution.

plot. The rise at low p_t is due to increased multiple scattering and reconstruction problems. Since the resolution is good at low p_t it has little effect on the p_t distribution, therefore a constant σ_{1/p_t} =0·017$(GeV/c)^{-1}$ was assumed.

In order to evaluate the effect of the resolution on a physical distribution, the *form* of the error in $1/p_t$ (in addition to its mean value) must be known. From eq. D.3 a gaussian distribution may not be automatically assumed, although the dominant term $(\sigma_p/p)^2$, is gaussian in $1/p$. A sample of 5000 minimum-bias events was generated using the Isajet Monte-Carlo [39] and passed through the standard detector simulation and event reconstruction software. The reconstructed and generated transverse momenta are compared by plotting the quantity $(1/p_t^{rec} - 1/p_t^{gen})/\sigma_{1/p_t}$, where σ_{1/p_t}, the reconstruction error, has no systematic contribution. The mean of the data for $p_t > 0{\cdot}2 GeV/c$, shown in fig. D.2(a), is approximately zero with an r.m.s. of $(1{\cdot}02 \pm 0{\cdot}01)$ as expected in this representation. A rather poor gaussian fit to the data yields a width of $\sigma_{fit} = 0{\cdot}72 \pm 0{\cdot}03$. This plot

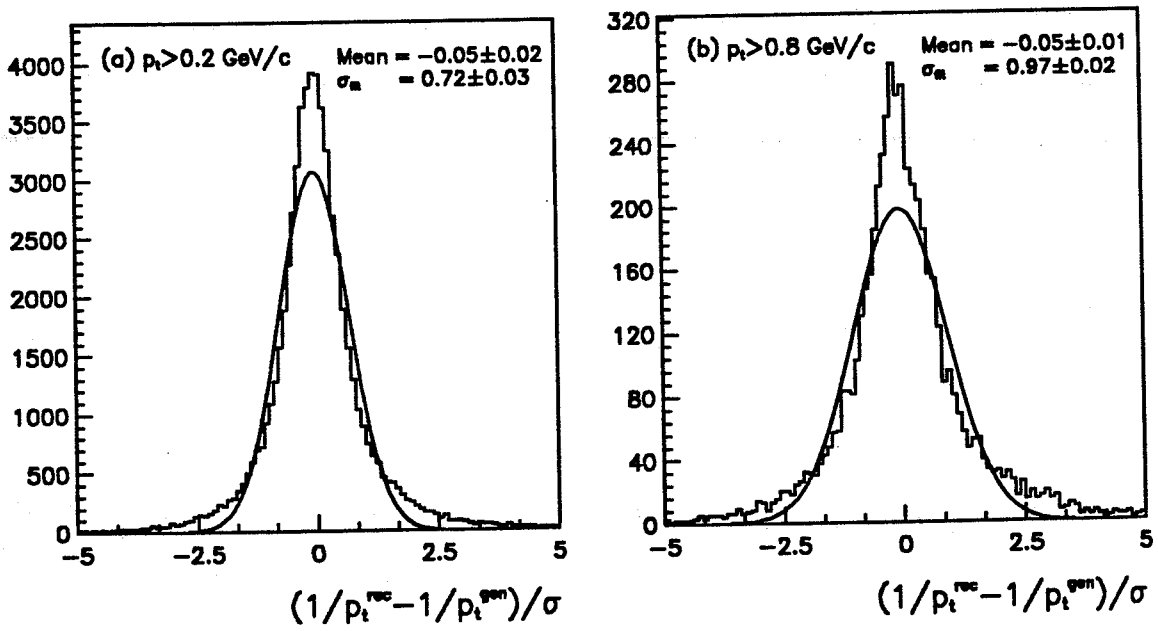

Figure D.2: Normalised error distribution in $1/p_t$

is, however, dominated by the low p_t particles for which σ_{1/p_t} is not constant, so a superposition of gaussians would be more reasonable. At low p_t, however, the effect of the resolution on the momentum spectrum is small. As p_t increases the tracks become straighter so Φ and λ are more accurately determined such that the momentum measurement error dominates. Fig. D.2(b) shows the same dis-

tribution for $p_t > 0{\cdot}8 GeV/c$. A gaussian fit yields $\sigma_{fit} = 0.97 \pm 0{\cdot}02$. The difference in test p_t distributions smeared with pure gaussian or slightly non-gaussian (as in fig. D.2) error distributions was found to be small compared to the difference between the smeared and unsmeared distributions. The error in $1/p_t$ was therefore parametrised by a gaussian for all p_t.

D.2 Deconvolution of the p_t spectrum

The differential cross-section must be corrected for the resolution of the CD. Since it is a steeply-falling distribution, the spectrum tends to become harder due to the smearing to higher p_t of lower momentum tracks. In order to deconvolute the true distribution from the measured one, an iterative procedure has been used. It is assumed that the measured and the true invariant cross-sections may be parametrised according to eq. 5.3. The smearing correction is, however, applied to the distribution, $f(p_t)$, defined using eq. 5.1 to be:

$$f(p_t) = \frac{d\sigma}{dp_t} \approx \Delta\phi \Delta\eta p_t E \frac{d^3\sigma}{dp^3} \tag{D.5}$$

since it is this distribution (within constant factors) which is primarily affected by the CD resolution.

A track having a true value $x = 1/p_t$ [1] will yield a measured value $\tilde{x}$ with a certain probability density, or resolution function $\rho(x, \tilde{x})$. Thus, if the true distribution of x is $g(x)$ then the measured distribution $\tilde{g}(\tilde{x})$ will be

$$\tilde{g}(\tilde{x}) = \int_0^\infty dx \; \rho(x, \tilde{x}) g(x) \tag{D.6}$$

The normalised gaussian resolution function, $\rho(x, \tilde{x})$, is given by

$$\rho(x, \tilde{x}) = \frac{e^{-(x-\tilde{x})^2/2\sigma_x^2}}{\sqrt{2\pi}\sigma_x} \tag{D.7}$$

[1] The distribution of interest is the p_t spectrum but since the CD error is gaussian in $1/p_t$, it is more natural to work with $x = 1/p_t$. Throughout this section, f denotes the p_t distribution and g denotes the corresponding x distribution, given by $g(x) = -f(p_t)/p_t^2$. A tilde is used to distinguish experimentally determined quantities.

The deconvolution of the p_t spectrum proceeds as follows: firstly, a sensible guess $f^0(p_t)$ is made for the form of the true distribution $f(p_t)$. The initial choice of $f^0(p_t)$ is a fit to the measured data, which is justified since the measured and the true distributions are sufficiently close. Next, $g^0(x) = -f^0(p_t)/p_t^2$ is smeared according to eq. D.6, resulting in a new distribution $g'(x)$, from which $f'(p_t) = -p_t^2 g'(x)$. Provided the trial function is reasonably close to the true distribution, the ratio of the true distribution to the measured distribution is approximately equal to the ratio of the trial function to the smeared trial function, *i.e.*

$$\frac{f(p_t)}{\tilde{f}(p_t)} \approx \frac{f^0(p_t)}{f'(p_t)} \tag{D.8}$$

The true distribution is then given approximately by

$$f(p_t) \approx f^0(p_t)\mathcal{W}(p_t) \qquad \text{where:} \quad \mathcal{W}(p_t) = \frac{\tilde{f}(p_t)}{f'(p_t)} \tag{D.9}$$

The correction function $\mathcal{W}(p_t)$ is a measure of the goodness of the trial function $f^0(p_t)$ and is consistent, within statistics, with unity when the trial function corresponds to the true function.

The correction $\mathcal{W}(p_t)$ is applied to the data points, the errors are recalculated, and the points are re-fitted to yield another trial function $f^1(p_t)$, which is closer to the true distribution, $f(p_t)$ than the first approximation $f^0(p_t)$. The procedure is then repeated using $f^1(p_t)$, $f^2(p_t)$, etc. as trial distributions until smearing of the trial distribution reproduces the experimental data, *i.e.* $\mathcal{W}(p_t) \simeq 1.0, \forall p_t$. Fig. D.3 shows the values of the fit parameters of corrected p_t spectrum as a function of the number of iterations of the deconvolution procedure. All the parameters are seen to converge rapidly to stable values. Fig. D.4 shows the inclusive charged particle cross-section before and after the smearing correction has been applied.

A test $\tilde{f}(p_t)$ distribution was produced using eq. D.5 by allowing the binned test function to fluctuate within Poisson statistics. These "data" were then smeared according to eq. D.3 and the deconvolution procedure is applied. The parameters from the fit after the final iteration were compared to those of the generated

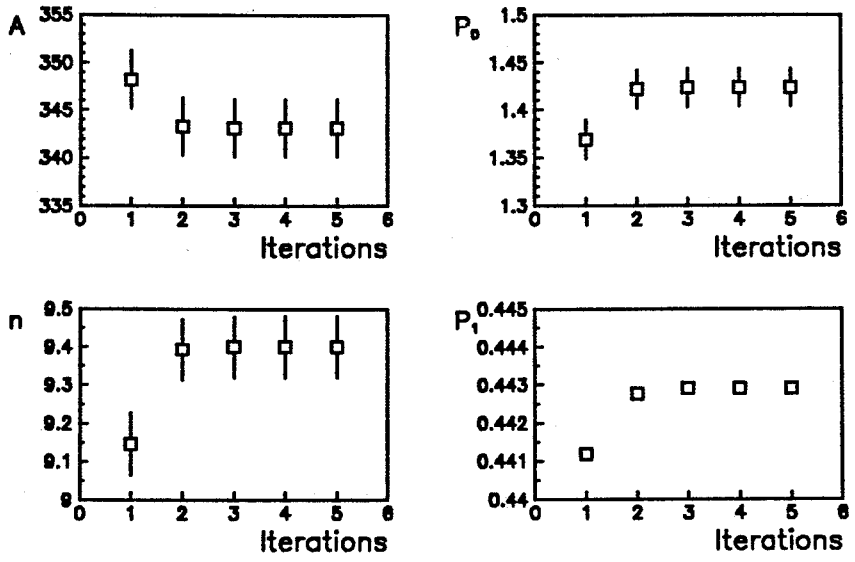

Figure D.3: Convergence of the p_t spectrum fit parameters.

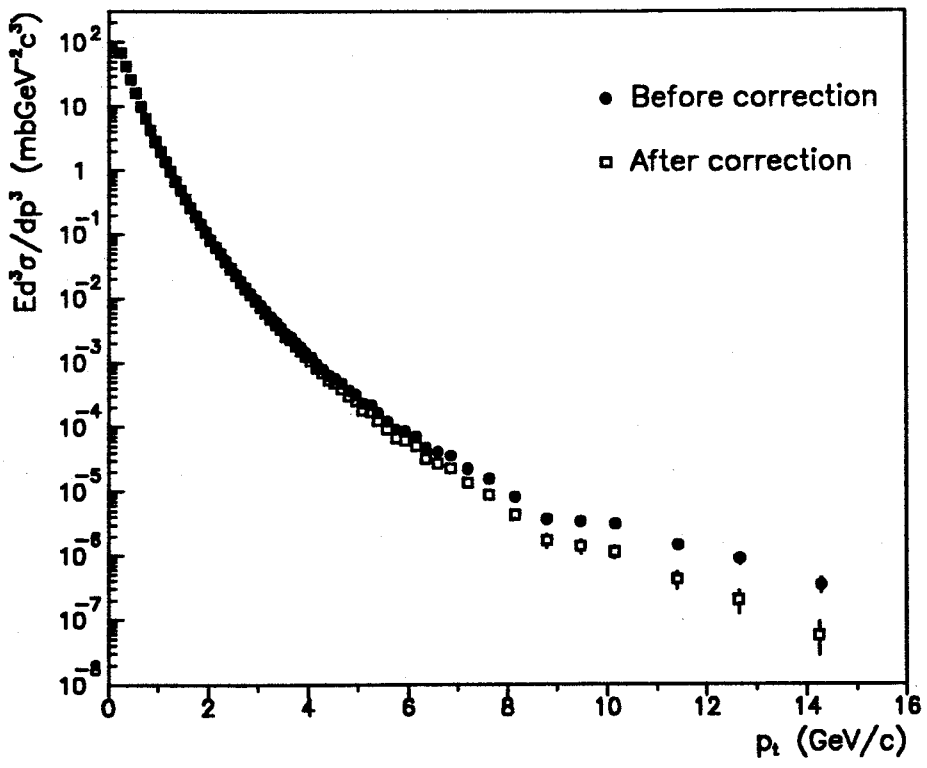

Figure D.4: Charged particle inclusive cross-section (a) Before smear correction (b) After smear correction.

function and were found to agree, within the errors of the fit.

In principle, the p_t spectrum for the K^0_S should also be corrected for the resolution. The K^0_S p_t resolution has been calculated for each candidate using the errors on the pion track properties and the primary vertex measurement. The cuts used to purify the K^0_S sample tend to select well measured K^0_S's. Furthermore, as can be seen in fig. 7.7, the efficiency is greatest in the bending-plane where the track momenta have the smallest errors. The K^0_S p_t resolution, $\sigma_{1/p_t}(K^0_S) = \sigma_{p_t}(K^0_S)/p_t^2$, shown in fig. D.5, is seen to be extremely good for all p_t. The effect of the CD

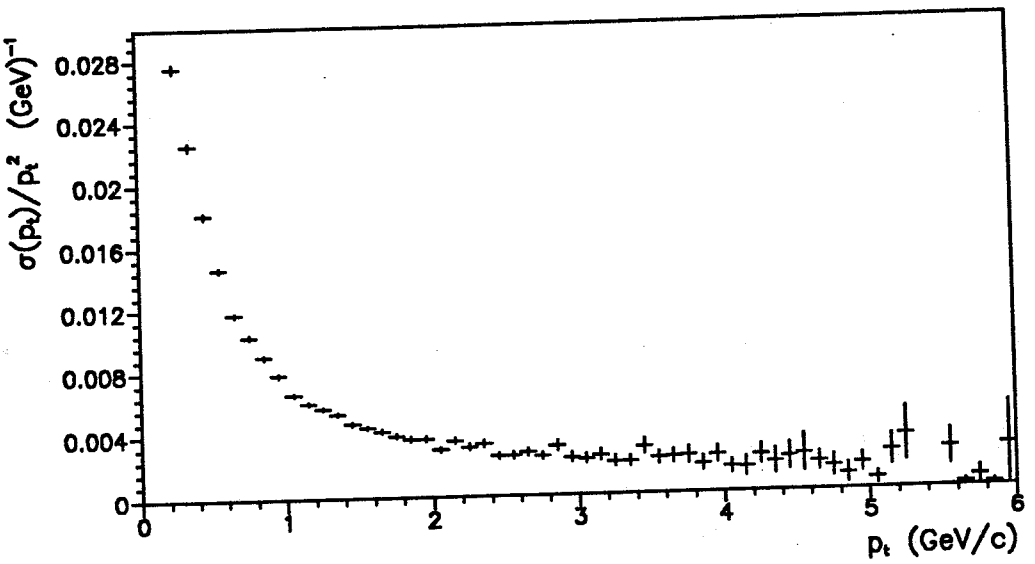

Figure D.5: K^0_S p_t resolution.

smearing is therefore negligible compared to the statistical and other systematic errors, so no correction was applied to the p_t spectrum of the K^0_S.

Bibliography

[1] Aitchison, I. J. R. and Hey, A. J. G. "Gauge Theories in Particle Physics" (1984) Adam Hilger, Bristol

[2] Glashow, S.L., Nucl. Phys. **22** (1961) 579; Salam, A., Ward. J. C., Phys. Lett. **13** (1964) 168; Weinberg S., Phys. Rev. Lett. **19** (1967) 1264

[3] Kobayashi, M. and Maskawa, K. Prog. Theor. Phys. **49** (1973) 652

[4] Gross, D. J. and Wilczek. F. Phys. Rev. D **8** (1973) 3633; **9** (1974) 980

[5] Hagedorn, R. Rev. Nuovo Cimento **6** (1983) N. 10

[6] Erwin, J. *et al.* Phys. Rev. Lett., **27**, 1534 (1971)

[7] Angelini, C. *et al.* Lett. Nuovo Cimento **19** (1977) 283

[8] Anisovich, V.V. and Shekhter, V. M. Nucl. Phys. **B55** (1973) 455

[9] Bjorken, J.D. and Farrar, G. R. Phys. Rev. **D9** (1974) 1449

[10] Anisovich, V.V. and Kobrinsky M. N. Phys. Lett. **52B** (1974) 217

[11] Collins, P.D.B. and Martin, A.D. "Hadron Interactions" (1984) Adam Hilger, Bristol

[12] Combridge, B.L., Kripfganz, J. and Ranft, J. Phys. Lett. **70B** (1977) 234

[13] Feynmann, R.P., Field, R.D. and Fox, G.C. Phys. Rev. **D18** (1978) 3320

[14] Particle data group. Phys. Lett. **204B** (1988) 1

[15] Staff of CERN $p\bar{p}$ Project. Phys. Lett. **107B** (1981) 306

[16] Jones, E. **CERN PS/87-93** (1987)

[17] Autin, B. *et al.* **CERN PS/88-43** (1988)

[18] Van de Meer, S., Rev. Mod. Phys. **57** (1985) 689

[19] Corden, M. *et al.* Physica Scripta **25**, (1982) 11

[20] Bauer, G. *et al.* N.I.M. **A253**, (1987) 179

[21] Eggert, K. *et al.* N.I.M. **176** (1980) 217

[22] Eggert, K. *et al.* N.I.M. **176** (1980) 223

[23] Robinson, D. Minutes of the UA1 Collaboration Meeting, (1988) Madrid

[24] Bernard, D. *et al.* (UA4) Phys. Lett. **186B** (1987) 227; Phys. Lett. **198B** (1987) 583

[25] Alner, G.J. *et al.* (UA5) Phys. Rep. **154** (1987) 247

[26] Robinson, D. and Wulz, C.W. **UA1/TN89-10**

[27] Eisenhandler, E., Ellis, N., Robinson, D. and Wulz, E. **UA1/TN89-24**

[28] Vuillemin, V. **UA1/TN86-37**

[29] Calvetti, M. *et al.* IEEE Trans. on Nuc. Sci. **NS-30**, No. 1, (1983) 71

[30] Barranco Luque, M. *et al.* N.I.M. **176** (1980) 175

[31] Calvetti, M. *et al.* N.I.M. **176** (1980) 255

[32] B. Hallgren and H. Verweij, IEEE Trans. Nucl. Sci. **NS-27**, No. 1, (1980) 333

[33] Karimäki, V. and Kroll, J. **UA1/TN87-100**

[34] Pimiä, M. PhD Thesis **HU-P-D45** (1985) Helsinki

[35] Calvetti,M. and Sadoulet, B. UA1 Technical Memo **80-06**

[36] Beingessner, S. *et al.* **UA1/TN86-14**

[37] Beingessner, S. *et al.* **CERN - EP/89-62**

[38] Bock, R.J. and Verkerk, F. **UA1/TN81-37**

[39] Paige, F.E. and Protopopescu, S.D. "ISAJET 5.30: A Monte-Carlo event generator for pp and $p\bar{p}$ interactions" BNL 38774 (1986)

[40] Zaccardelli, C. M. V. Tesi di Laurea (1985) Università di Roma La Sapienza

[41] Albajar, C. *et al.* Nuc. Phys. **B335** (1990) 261

[42] Arnison, G. *et al.* Phys. Lett. **B118** (1982) 167

[43] Abe, F. *et al.* **ANL-HEP-PR-88-32**

[44] Alner, G. J. *et al.* (UA5) Z. Phys. **C33** (1986) 1

[45] Adamus, M. *et al.* Phys. Lett. **B177** (1988) 239

[46] Adamus, M. *et al.* Z. Phys. **C37** (1988) 215

[47] Ward, D. CERN-EP/87-178 (1987)

[48] Koba, Z., Nielson, H.B. and Oleson, P. Nucl. Phys. **B40** (1972) 317

[49] Alner, G. J. *et al.* (UA5) Phys. Lett. **B138** (1984) 304

[50] Ciapetti, G. "Proc. of the 5^{th} Topical Workshop on $p\bar{p}$ Collider Physics." (1985) Ed. M. Greco, World Scientific, Singapore

[51] Geer, S. *et al.* **UA1/TN84-51**

[52] Karimäki, V. **UA1/TN85-88**

[53] Karimäki, V. *et al.* **UA1/TN85-88**

[54] Zacharov, I.E. PhD. Thesis (1989) Univ. of Amsterdam

[55] Ciapetti, G. *et al.* **UA1/TN87-73**

[56] Kroll, J. Private communication.

[57] Highland, V.L. N.I.M. **129** (1975) 497 with erratum : Highland, V.L. N.I.M. **161** (1979) 171

[58] Nisati, A. Tesi di Laurea (1986) Università di Roma La Sapienza

[59] Alner, G.J. *et al.* (UA5) Nucl. Phys. **B258** (1985) 505

[60] Banner, M. *et al.* (UA2) Phys. Lett. **122B** (1983) 322

[61] Ansorge, R.E. *et al.* (UA5) Phys. Lett. **B199** (1987) 311

[62] Banner, M. *et al.* (UA2) Phys. Lett. **115B** (1982) 59

[63] Arnison, G. *et al.* (UA1) Phys. Lett. **118B** (1981) 167

[64] Arnison, G. *et al.* (UA1) Phys. Lett. **123B**, (1983) 108

[65] Ciapetti, G. *et al.* **UA1/TN84-55**